Computational Atomic Structure

Applications to Astrophysics and Nuclear Structure

ASIMINA PAPOULIA
FACULTY OF SCIENCE | DEPARTMENT OF PHYSICS | LUND UNIVERSITY 2020

Computational Atomic Structure: Applications to Astrophysics and Nuclear Structure

Computational Atomic Structure: Applications to Astrophysics and Nuclear Structure

by Asimina Papoulia

LUND UNIVERSITY

MALMÖ UNIVERSITY

Thesis for the degree of Licentiate of Philosophy
Thesis advisors: Prof. Tomas Brage, Prof. Per Jönsson and Assoc. Prof. Jörgen Ekman
Faculty opponent: Prof. Jacek Bieroń

To be presented, with the permission of the Faculty of Science of Lund University, for public criticism in the Mathematical Physics lecture hall C368 at the Department of Physics on Friday, the 13th of March 2020 at 13:00.

Organization
LUND UNIVERSITY

Department of Physics
Box 118
SE–221 00 LUND
Sweden

Author(s)
Asimina Papoulia

Document name
LICENTIATE DISSERTATION

Date of defence
2020-03-13

Sponsoring organization

Title and subtitle
Computational Atomic Structure: Applications to Astrophysics and Nuclear Structure

Abstract
This thesis deals with the modelling of atoms and ions. In heavy systems, where the effect of the nuclear size must be considered, a fully relativistic treatment based on the Dirac-Coulomb Hamiltonian is needed. Chapter two of the thesis provides an introduction to the basic principles of the fully relativistic multiconfiguration Dirac-Hartree-Fock (MCDHF) method, which is a variational approach for determining the wave functions. After we demonstrate how to obtain the best approximation of the wave functions by optimizing the energy expression, we describe how to compute the eigenvalues of operators other than the Hamiltonian, and how these eigenvalues correspond to measurable quantities. Chapter three and four, respectively, summarize the work done in the two published papers, illustrating some of the applications of the relativistic atomic structure theory.

Paper I is an example of atomic structure calculations for astrophysical applications. Extensive amount of atomic transition data are produced for the systems of neutral and singly ionized aluminium that can be used to improve the interpretation of abundances in stars.

Paper II demonstrates a novel method, in which the atomic structure calculations of isotope shifts are combined with experimental data, for extracting nuclear properties other than the charge radii.

Key words
Atomic structure, transition energies, transition probabilities, stellar spectra, abundance analysis, isotope shift, field shift, reformulated field shift, nuclear sizes, nuclear deformation

Classification system and/or index terms (if any)

Supplementary bibliographical information

Language
English

ISSN and key title

ISBN
978-91-7895-436-0 (print)
978-91-7895-437-7 (pdf)

Recipient's notes

Number of pages
104

Price

Security classification

Computational Atomic Structure: Applications to Astrophysics and Nuclear Structure

by Asimina Papoulia

LUND
UNIVERSITY

MALMÖ
UNIVERSITY

A licentiate thesis at a university in Sweden takes either the form of a single, cohesive research study (monograph) or a summary of research papers (compilation thesis), which the doctoral student has written alone or together with one or several other author(s).

In the latter case the thesis consists of two parts. An introductory text puts the research work into context and summarizes the main points of the papers. Then, the research publications themselves are reproduced, together with a description of the individual contributions of the authors. The research papers may either have been already published or are manuscripts at various stages (in press, submitted, or in draft).

Faculty of Science, Department of Physics

ISBN: 978-91-7895-436-0 (print)
ISBN: 978-91-7895-437-7 (pdf)

Printed in Sweden by Media-Tryck, Lund University, Lund 2020

"Educating the mind without educating the heart is no education at all"

- Aristotle

Acknowledgements

I would like to sincerely thank my supervisors, Per Jönsson, Jörgen Ekman, and Tomas Brage for their constant guidance and support during these past three years, and for giving me, in the first place, the opportunity to conduct my doctoral studies in their research group. I have learned a lot from our discussions, and I have really appreciated your valuable feedback. Your genuine enthusiasm for physics has made me feel inspired and motivated.

I would also like to thank Henrik Hartman for all the discussions on astrophysical topics, and the members of the LUMCAS group and the broader CompAS community for making me enjoy every single meeting and conference and reminding me that physics is, above all, fun. Further, I am thankful to all my colleagues at Malmö University for creating a pleasant atmosphere and friendly working environment. I am especially grateful to Mats Persson for always being happy to help me with all kinds of matters.

I also wish to thank my colleagues at the division of Mathematical Physics at Lund University, in particular, Katarina Lindqvist for helping me with everything I needed, and all the PhD students I have met there over the years. Special memories were created at this place, where my journey in research began. Thank you Sara for all the nice moments, both inside and outside work, and thank you Gunnar for our talks, the memorable, exhaustive post-work workouts and for sharing the office with me. Special thanks go to Cecilia Jarlskog for the exciting discussions on the history of physics and beyond, which accompanied me during the long nights at the division.

But most importantly, I want to thank the people that make all this work and effort worthwhile. Thank you Marina for creating some of my best memories so far and for making me laugh my head off, Lorena for being my best friend in Sweden from day one, Zizi, Chryssa, Elena, and Virginia for making me looking forward to my visits back home. You guys have always being there for me, at my best and my worst. Thank you Katerina for being by my side, helping me find my inner piece and making me happy.

I am most thankful to my mom and dad, because, literally, none of this would have been possible without them. Μαμά και μπαμπά, ευχαριστώ που είστε πάντα δίπλα μου, υποστηρίζοντας κάθε μου επιλογή. Αλλά και που ο καθένας σας ξεχωριστά είναι πηγή έμπνευσης για μένα.

Contents

List of publications

This thesis is based on the following publications, referred to by their Roman numerals:

I **Extended transition rates and lifetimes in Al I and Al II from systematic multiconfiguration calculations**

A. Papoulia, J. Ekman, and P. Jönsson
A&A 621, A16 (2019)

Aluminium is an important element in astrophysics. Correct deduction of aluminium abundances, together with chemical evolution modeling, is necessary to put together a complete picture of the stellar and galactic evolution. During the past decades, a considerable amount of research was conducted for the systems of Al I and Al II. Yet, there is still a need for extended and accurate theoretical transition data that could meet the demands raised from the obtained high-resolution astronomical spectra that are to be analysed. In this work, updated transition data have been produced to include the 28 and 78 lowest states in neutral and singly ionized aluminium, respectively. The present calculations are extended to higher energies and many of the computed transitions fall in the infrared spectral region. The new generation of telescopes are designed for this region, and these transition data are of high importance.

Contribution: I carried out the computations in both Al I and Al II using the GRASP2018 package [1]. Computational methods and strategies were discussed on a regular basis with JE and PJ, and all steps of the computational procedure were followed under their supervision. As part of this project, I wrote an additional computer program for handling the expansions of the atomic state functions that facilitated and sped up the final computations. I performed a thorough review of previous theoretical and experimental works on these two atomic systems, and I was the main responsible for the preparation of the manuscript, which was revised by JE and PJ. I produced all figures and tables using the tools of GRASP2018. This work was presented at the CompAS 2018[1] and ICAMDATA 2018[2] International Conferences.

[1] `http://ddwap.mah.se/tsjoek/compas/`
[2] `https://projects.iq.harvard.edu/icamdata`

II **Effect of realistic nuclear charge distributions on isotope shifts and progress towards the extraction of higher-order nuclear radial moments**

A. Papoulia, B.G. Carlsson, and J. Ekman

PRA 94, 042502 (2016)

With the continuous advancement in experimental methods, one may ask whether the improved precision and access to several atomic transitions in different isotopes make it possible to obtain more data on the nuclear isotopes than just the $\delta\langle r^2\rangle$ values commonly extracted so far. Starting from the expression of the reformulated field shift [2], we demonstrated that the electron states in heavy systems are sensitive not only to the $\delta\langle r^2\rangle$ but also to changes in $\langle r^4\rangle$ values. Hence, information about the nucleus beyond the root-mean-square (rms) radius can potentially be deduced from isotope shift (IS) observations. In this work, a promising and novel method for the extraction of both $\delta\langle r^2\rangle$ and $\delta\langle r^4\rangle$ radial moment differences from experimental IS was presented and tested. Considering both systematical and statistical errors in the extraction procedure, we concluded that an increase in experimental precision by 1-2 orders of magnitude, or, access to data for more independent atomic transitions, would be essential. This would open the possibility for systematic tabulation of the changes in $\langle r^4\rangle$ nuclear moments between different isotopes.

Contribution: The bulk of the results and figures presented in Sections III, IV, and V.A-B were produced in the course of my master thesis project [3], performing both nuclear and atomic structure calculations [4, 5, 6]. I also produced the results shown in Subsections V.C-D and generated all tables and figures. All computational steps were carried out under the guidance of GC and JE. I was the main responsible for the preparation of Sections II-V of the manuscript, which was revised and completed by GC and JE. This work was presented at the CompAS 2017[3] and REHE 2017[4] International Conferences.

[3] see footnote 1

[4] `https://www.online.uni-marburg.de/rehe2017/`

List of acronyms

AS	Active Set
ASF	Atomic State Function
CFPs	Coefficients of Fractional Parentage
CG	Clebsch-Gordan
CI	Configuration Interaction
CSF	Configuration State Function
DHF	Dirac-Hartree-Fock
EOL	Extended Optimal Level
FS	Field Shift
GRASP	General Relativistic Atomic Structure Package
HF	Hartree-Fock
IS	Isotope Shift
MCDHF	MultiConfiguration Dirac-Hartree-Fock
MS	Mass Shift
MR	MultiReference
NMS	Normal Mass Shift
RCI	Relativistic Configuration Interaction
RFS	Reformulated Field Shift
SCF	Self-Consistent Field
SMS	Specific Mass Shift
SD-MR	Single and Double (substitutions from) MultiReference
QED	Quantum ElectroDynamics

Popular summary

To correctly describe the laws that govern the physical world, we have to study the structure of matter and how the fundamental constituents of the universe interact. The basic building block for all regular matter in the universe is the atom, which is made up of electrons orbiting its nucleus. The atom is a quantal many-body system, and its structure is characterized by the discrete, and distinctive for each element, energy levels of the electrons. Interactions of the electrons with internal and external electromagnetic fields give rise to atomic transitions, through absorption or emission of photons with certain energies. This causes the total energy of the system to change. Since the allowed energy levels are unique to an element, so are the energies corresponding to transitions between those levels.

Our knowledge on the formation and evolution of the universe mainly comes from the emitted starlight through atomic transitions, which is displayed as an energy spectrum with lines of different energies and intensities. The positions of the spectral lines reveal the elements a specific star consists of, and from their intensities the elemental abundances are deduced. For the interpretation of the observed spectra, atomic reference data are needed. Laboratory measurements are usually costly and time-consuming, and the produced experimental data are not always sufficient. It is, thus, necessary to develop quantum mechanical models that describe the atomic structure and underlying processes. Computations can, then, be performed to predict the atomic transition energies and other atomic parameters. Such an example are the computations that were performed, in Paper I, for the systems of neutral and singly ionized aluminium.

Although the atomic nucleus is $\sim 10^4$ times smaller than the size of the atom, its finite mass and extended charge distribution have a measurable effect on the atomic spectra. For a particular element, the spectral lines from different isotopes display a small shift in energy, known as the line isotope shift. The atomic electrons are, therefore, sensitive probes of the properties of the nucleus they are bound to. In Paper II, we show how the modeling of the isotope shift can be combined with experimental data to extract information about the details of the nuclear charge distributions. Nuclear-model independent information can be used to benchmark nuclear structure calculations. An understanding of the structure and dynamics of atomic nuclei is fundamental to our overall picture of the universe, as nucleosynthesis is inseparably connected with stellar evolution.

Populärvetenskaplig sammanfattning

För att beskriva lagarna som styr den fysiska världen behöver vi studera materiens struktur och hur dess olika delar växelverkar. Den grundläggande byggstenen för all materia är atomen, vilken består av elektroner som rör sig runt en kärna. Atomen är ett kvantiserat mångkropparssystem, vars struktur karakteriseras de diskreta, och för ämnet unika, elektronbanor. Växelverkan mellan elektronerna och interna- och externa elektromagnetiska fält leder till energiövergångar genom absorption eller emission av en foton med väldefinierad energi. Dessa övergångar medför att elektronerna hoppar från ett tillstånd till ett annat varvid systemets totala energi ändras. Eftersom energinivåerna är unika för ett ämne så blir på motsvarande sätt energierna för övergångar mellan dessa nivåer unika.

Vår kunskap om universums skapelse och utveckling kommer i huvudsak från ljuset från utsänt från atomerna i stjärnorna. Ljuset uppdelas i ett energispektrum med linjer med olika energier och intensiteter. Spektrallinjernas energier eller positioner avslöjar vilka ämne som bygger upp stjärnorna, och från intensiteterna kan halten av de olika ämnena bestämmas. För tolkning av observerade spektra behövs atomära referensdata. Dessa data kan bestämmas via laboratoriemätningar, men dessa är ofta dyra och tidskrävande. Data från experiment täcker inte heller behoven. Det är därför nödvändigt att utveckla kvantmekaniska modeller och teorier, vilka beskriver den atomära strukturen och de underliggande energiövergångarna. Utifrån dessa modeller kan sedan beräkningar utföras vilka ger de tillåtna energinivåerna och andra egenskaper relaterade till energiövergångar. Beräkningarna i papper I för neutralt och enkelt joniserat aluminium är exempel på sådana beräkningar.

Även om atomkärnan är ungefär 10^4 gånger mindre än atomen så har dess massa och utsträckta laddningsfördelning en mätbar effekt på atomens energispektrum. För ett givet ämne uppvisar spektrallinjerna från olika isotoper ett litet energiskift, känt som isotopskiftet. Atomens elektroner är alltså känliga prober, som känner av egenskaperna hos kärnan. I papper II visar vi hur modellering och noggranna studier av isotopskiftet kombinerat med experimentella data möjliggör extraktion av detaljerad information om kärnans laddningsfördelning. Modelloberoende information om laddningsfördelningen kan användas för att validera kärnstrukturen. En ökad förståelse för kärnornas struktur och dynamik är viktig för vår övergripande bild av universum då nukleosyntes är tätt knuten till stjärnutveckling.

Chapter 1

Introduction

Physics investigates the basic principles and laws that govern the physical world we live in. Through astrophysical observations a continuous effort is put to unveil the mysteries of our universe. To understand how the universe, its galaxies, and solar systems were formed and evolved, we need to closely study their constituents; celestial objects including our Sun and other stars. Stars are hot spheres of plasma that are powered by nuclear fusion in their cores, where various elements are formed. In fact, stellar evolution studies are inseparable with nucleosynthesis and chemical evolution [7].

Chemical evolution modeling requires astrophysicists to perform abundance analysis [8, 9]. Their main source of information about stars is the light emitted through atomic transitions. When light from stars is displayed according to the transition energies, the result is an energy spectrum. An energy spectrum consists of lines of different energies and intensities, and the detailed positions of these lines depend on the elements that a specific star consists of. Information about stars, such as elemental composition and abundances, can thus be extracted by analyzing their spectra.

The elemental abundances are not observed, but interpreted. To translate astrophysical observations into knowledge, the atomic structures and underlying processes that generate the spectra need to be well understood and described. Examples of such processes are the interactions with electromagnetic fields that take place in different atoms and ions. In many cases, the description of atomic structures and interactions is only available through quantum mechanical calculations that need to be benchmarked against precision experiments. Atomic data are then generated, and they can be used for identifying the observed spec-

tral lines [10] and for deducing elemental abundances. Paper I is an instance of atomic structure calculations for astrophysical applications, such as abundance analyses of stars.

The knowledge of the origin and evolution process of the astronomical objects that exist in the universe depends not only on their elemental abundances, but also on their isotopic composition [11, 12]. For a particular element, the spectra of the various isotopes are very similar; however, a small shift in energy is observed, known as the isotope shift (IS). The intensities of the spectral lines that represent the different isotopes are used to derive the isotopic abundances [13]. Therefore, besides the transition energies and transition probabilities, the IS is another fundamental parameter that is involved in abundance analyses and needs to be determined [14].

The IS can be decomposed into the mass shift (MS) and the field shift (FS) parts. The former arises from the recoil energy of finite nuclear masses, while the latter emerges from the extended nuclear charge density distributions. The contribution from the FS is most often assumed to be proportional to the difference in the $\langle r^2 \rangle$ nuclear moments of the respective isotopes [15]. In heavy atoms, the FS might be dominated by the term involving $\delta\langle r^2 \rangle$, yet the contributions from changes in higher-order radial moments of the nuclear charge distribution become substantial and must be considered for accurate predictions of IS. These higher-order moments contain information not only about the nuclear charge radii, but also the specifics of the shapes of the nuclear charge distributions.

By comparing IS measurements with theoretical predictions, it has so far been possible to extract $\delta\langle r^2 \rangle$ values for numerous isotope pairs, e.g., [16, 17, 18], from which the root-mean-square (rms) radii of the respective nuclei were determined [19]. Available data of nuclear charge radii allow for detailed studies of the evolution of nuclear sizes for isotope sequences along nearly the entire periodic table. The observed trends then serve as benchmarks for nuclear structure calculations, which are key to understanding the mechanisms that occur during nucleosynthesis. Even so, access to nuclear properties other than the charge radius would open up opportunities to explore various scenarios in nuclear physics and to search for new physics beyond the Standard Model [20, 21].

Experimental techniques, such as electron scattering, typically yield more detailed information of nuclear charge distributions than just the rms radius [22, 23]. Electron scattering experiments are, however, possible only for stable or long-lived isotopes. When it comes to radioactive nuclei, there is an apparent need to explore other strategies. Using a reformulated expression for the FS, which takes into account changes in higher than the second-order nuclear mo-

ments [2], in Paper II, we illustrate a novel approach that could be utilized to probe details of the nuclear charge density distribution beyond rms radii.

This thesis aims at complementing Papers I and II by giving an insight on the computation of atomic properties, while addressing the greatest challenges. During the past decades various computational methods have been developed for the description of the atom and its structure. The results of the two papers are produced using the General Relativistic Atomic Structure Package (GRASP) [1, 6], which is developed within the CompAS collaboration[1] and implements the multiconfiguration Dirac-Hartree-Fock (MCDHF) approach [24]; a fully relativistic variational method. To meet the current needs for atomic data, GRASP is continuously upgraded and enhanced.

Chapter two provides the theoretical background of the fully relativistic atomic structure calculations, focusing on the principles of the MCDHF approach. The following two chapters illustrate some of the applications of atomic structure calculations in astrophysics and nuclear structure, in relation to Papers I and II, respectively. Finally, chapter five provides an outlook with ideas on future research work and the required program development. Copies of the two published papers are included at the end of the thesis.

[1] `https://github.com/compas`

Chapter 2

Relativistic Atomic Structure

The relativistic atomic structure theory is fully discussed in a number of previous works, including the book on atomic structure by Johnson [25], which uses the framework of perturbation theory to illustrate the fundamental concepts of the relativistic treatment of atoms. The book by Grant [24] describes in great detail the relativistic modelling of atoms and molecules using a variational approach, and in particular, the MCDHF method, which is the method of our choice. A very readable description of the relativistic atomic theory can also be found in the publication by Dyall et al. [26], which reports on an early release of the GRASP code. Finally, both non-relativistic and relativistic multiconfiguration methods are discussed in the recent review article by Froese Fischer et al. [27]. With this chapter, we only aim at providing the reader with a short introduction to the basic principles of the relativistic multiconfiguration method as it applies to GRASP2018 [1].

2.1 The Relativistic Many-Electron Hamiltonian

For complex atomic systems with $N > 1$ electrons, the Hamiltonian can be expressed in terms of a sum over N one-particle operators h_i and $N(N-1)/2$ two-particle operators h_{ij},

$$\mathcal{H} = \sum_{i=1}^{N} h_i + \sum_{i<j}^{N} h_{ij}. \tag{2.1}$$

2.1.1 The Dirac-Coulomb Hamiltonian

The main relativistic effects in the Hamiltonian steam from the one-electron operator

$$h_i = T_i + V(r_i), \tag{2.2}$$

where T_i is the kinetic energy of the electron i and $V(r_i) = V_{\text{nuc}}(r_i)$ is the potential energy arising from the Coulomb interaction of this electron with the atomic nucleus, with r_i being the distance between the electron and the nucleus.

The potential $V_{\text{nuc}}(r_i)$ accounts for an extended nuclear charge density distribution, instead of a point-like nucleus. An extended charge distribution can be obtained by either an approximate model, such as the Fermi distribution [28], or microscopic nuclear structure models. This is central to Paper II, and various nuclear charge distribution models will be discussed more thoroughly in Chapter 4.

According to Dirac's theory, the kinetic energy in Eq. (2.2) takes the form

$$T_i^{\text{D}} = c\,\boldsymbol{\alpha}_i \cdot \mathbf{p}_i + (\beta_i - 1)c^2, \tag{2.3}$$

where c is the speed of light in atomic units[1], $\mathbf{p} \equiv -\mathrm{i}\boldsymbol{\nabla}$ is the electron momentum operator, and $\boldsymbol{\alpha}$ and β are the 4×4 Dirac matrices:

$$\boldsymbol{\alpha} = \begin{pmatrix} 0 & \boldsymbol{\sigma} \\ \boldsymbol{\sigma} & 0 \end{pmatrix}, \qquad \beta = \begin{pmatrix} \mathbf{I} & 0 \\ 0 & -\mathbf{I} \end{pmatrix}, \tag{2.4}$$

where $\mathbf{I}$ is the unit matrix 2×2, and σ is defined by the hermitian matrices:

$$\sigma_x = \begin{pmatrix} 0 & 1 \\ 1 & 0 \end{pmatrix}, \qquad \sigma_y = \begin{pmatrix} 0 & -\mathrm{i} \\ \mathrm{i} & 0 \end{pmatrix}, \qquad \sigma_z = \begin{pmatrix} 1 & 0 \\ 0 & -1 \end{pmatrix}. \tag{2.5}$$

In the relativistic treatment of the atom, the one-particle Dirac operator is then given by

$$h_i^{\text{D}} = T_i^{\text{D}} + V_{\text{nuc}}(r_i). \tag{2.6}$$

The two-particle operator in Eq. (2.1) can to a first approximation be represented by the potential energy $V(i,j)$ that emerges from the Coulomb interac-

[1]The atomic units are defined by requiring that the Planck's constant $\hbar$, and the electron's rest mass m_e and charge e, all have the value 1. The speed of light in the vacuum is given by $c = 1/\alpha$, where $\alpha \approx 1/137$ is the fine-structure constant.

tion between two electrons i and j, that is

$$h_{ij}^{\mathrm{C}} = V(i,j) = \frac{1}{r_{ij}}, \tag{2.7}$$

where $r_{ij} = |\boldsymbol{r}_i - \boldsymbol{r}_j|$ is the interelectronic distance. Inserting (2.6) and (2.7) in (2.1) results in what is known as the Dirac-Coulomb Hamiltonian

$$\mathcal{H}^{\mathrm{DC}} = \sum_{i=1}^{N} [c\, \boldsymbol{\alpha_i} \cdot \mathbf{p}_i + (\beta_i - 1)c^2 + V_{\mathrm{nuc}}(r_i)] + \sum_{i<j}^{N} \frac{1}{r_{ij}}. \tag{2.8}$$

The Dirac-Coulomb Hamiltonian is the one used in the self-consistent field (SCF) calculations. The SCF procedure will be discussed later in Subsection 2.3.3.

2.1.2 Breit interaction

In relativistic atomic structure, the two-electron interaction is essentially much more complex than the apparent instantaneous Coulomb interaction given by Eq. (2.7) and thus, the Dirac-Coulomb Hamiltonian (2.8) is only a first approximation. For precision calculations, further corrections suggested by quantum electrodynamics (QED) [29, 30, 31] need to be taken into account [32].

The leading correction to the Coulomb interaction is given by what is known as the *transverse photon* (TP) interaction, which is due to magnetic interactions and retardation effects. The latter effects emerge from the finite speed of the exchanged virtual photons between a pair of electrons [33]. The Hamiltonian that accounts for the *transverse photon* interaction, which is correct to order of α^2, is written as

$$h_{ij}^{\mathrm{TP}} = -\sum_{i<j}^{N} \left[\frac{\boldsymbol{\alpha}_i \cdot \boldsymbol{\alpha}_j \cos(\omega_{ij} r_{ij}/c)}{r_{ij}} + (\boldsymbol{\alpha}_i \cdot \boldsymbol{\nabla}_i)(\boldsymbol{\alpha}_j \cdot \boldsymbol{\nabla}_j) \frac{\cos(\omega_{ij} r_{ij}/c) - 1}{\omega_{ij}^2 r_{ij}/c^2} \right], \tag{2.9}$$

where $\omega_{ij} = |\epsilon_i - \epsilon_j|/c$ is the angular frequency of the exchanged photon, related to the differences between the one-particle energies of the electrons i and j and $\boldsymbol{\nabla}$ is the gradient operator involved in the differentiation of $r_{ij} = |\boldsymbol{r}_i - \boldsymbol{r}_j|$.

In the low frequency approximation, $\omega_{ij} \to 0$ and Eq. (2.9) reduces to what is known as the Breit interaction, given by

$$h_{ij}^{\mathrm{Breit}} = -\sum_{i<j}^{N} \frac{1}{2r_{ij}} \left[(\boldsymbol{\alpha}_i \cdot \boldsymbol{\alpha}_j) + \frac{(\boldsymbol{\alpha}_i \cdot \boldsymbol{r}_{ij})(\boldsymbol{\alpha}_j \cdot \boldsymbol{r}_{ij})}{r_{ij}^2} \right]. \tag{2.10}$$

The corrections from the frequency dependent part are generally very small, and the total Hamiltonian of the system is typically expressed as

$$\mathcal{H}^{\mathrm{DCB}} = \mathcal{H}^{\mathrm{DC}} + \mathcal{H}^{\mathrm{TP}} \simeq \mathcal{H}^{\mathrm{DC}} + \mathcal{H}^{\mathrm{Breit}}. \tag{2.11}$$

The Breit corrections to the Dirac-Coulomb Hamiltonian are accounted for in the relativistic configuration interaction (RCI) calculations that follow the SCF procedure. Additional significant QED contributions, such as the *self-energy* (SE) and *vacuum polarization* (VP), can also be included in the RCI calculations. This yields the final Hamiltonian

$$\mathcal{H}^{\mathrm{DCB+QED}} = \mathcal{H}^{\mathrm{DCB}} + \mathcal{H}^{\mathrm{SE}} + \mathcal{H}^{\mathrm{VP}}. \tag{2.12}$$

2.2 Relativistic Wave Functions

In atomic structure, the fundamental problem is the calculation of the wave functions that describe the quantum states of interest. Once the wave functions have been determined, a number of atomic properties can be computed (see Section 2.4). A stationary state of an N-electron system is described by a wave function $\Psi(\mathbf{q}_1, ..., \mathbf{q}_N)$, where $\mathbf{q}_i = (\mathbf{r}_i, \sigma_i)$ represents the space and spin coordinates of the electron i. To determine the wave function Ψ, we need to solve the wave equation for the Hamiltonian $\mathcal{H}$ of choice, which in mathematical terms is an eigenvalue problem

$$\mathcal{H}\Psi(\mathbf{q}_1, ..., \mathbf{q}_N) = E\Psi(\mathbf{q}_1, ..., \mathbf{q}_N). \tag{2.13}$$

Solutions to (2.13) thus exist only for certain values of E, representing the total energy of the system. Due to the many-electron term (2.7) that enters the Dirac-Coulomb Hamiltonian (2.8), the eigenvalue problem cannot be solved exactly, and the atomic structure calculations are based upon the orbital approximation.

In the context of the *central field* approximation, the potential arising from the Coulomb interaction between the electrons is replaced by a central average potential due to the nucleus and the other electrons, i.e.,

$$V_{\mathrm{av}}(r_i) = V_{\mathrm{nuc}}(r_i) + u(r_i). \tag{2.14}$$

The Dirac-Coulomb Hamiltonian of Eq. (2.8) can then be expressed as

$$\mathcal{H}^{\mathrm{DC}} \approx \mathcal{H}_0 = \sum_{i=1}^{N} h_i^{\mathrm{D}}, \tag{2.15}$$

where

$$h_i^{\mathrm{D}} = c\,\boldsymbol{\alpha}_i \cdot \mathbf{p}_i + (\beta_i - 1)c^2 + V_{\mathrm{av}}(r_i) \tag{2.16}$$

is the modified Dirac Hamiltonian operator representing the energy of an electron i moving in the spherically symmetric scalar potential of (2.14). The eigenvalue problem downsizes to

$$\mathcal{H}_0\Psi_0(\mathbf{q}_1, ..., \mathbf{q}_N) = E_0\Psi_0(\mathbf{q}_1, ..., \mathbf{q}_N) \tag{2.17}$$

and since the approximate Hamiltonian $\mathcal{H}_0$ is separable, the eigenvalues and eigenfunctions can respectively be written as

$$E_0 = \langle\Psi_0|\mathcal{H}_0|\Psi_0\rangle = \sum_{i=1}^{N} \epsilon_i \tag{2.18}$$

and

$$\Psi_0(\mathbf{q}_1, ..., \mathbf{q}_N) = \prod_{i=1}^{N} \phi_i(\mathbf{q}_i), \tag{2.19}$$

where $\phi_i(\mathbf{q}_i)$ are the one-electron wave functions, also known as *spin-orbitals*, and ϵ_i are the corresponding one-electron energies.

2.2.1 One-electron Dirac orbitals

The *central field spin-orbitals* $\phi(\mathbf{q})$ satisfy the single-particle Dirac equation

$$h^{\mathrm{D}}\phi(\mathbf{q}) = \epsilon\phi(\mathbf{q}). \tag{2.20}$$

The Hamiltonian h^{D} commutes with the parity π and total angular momentum $\mathbf{j} = \mathbf{l}+\mathbf{s}$ and thus, we seek *spin-orbital* solutions $\phi_{nlsjm}(\mathbf{q}_i)$ that are simultaneous eigenfunctions of these operators, so that

$$\begin{aligned} &\pi\phi_{nlsjm} = (-1)^l\phi_{nlsjm}, \\ &\mathbf{j}^2\phi_{nlsjm} = j(j+1)\phi_{nlsjm}, \\ &j_z\phi_{nlsjm} = m\phi_{nlsjm}, \;\; m = -j, -j+1, ..., j. \end{aligned} \tag{2.21}$$

Spin-orbitals determined in a *central field* form an orthonormal set. What is more, the Dirac equation (2.20) allows the separation of the radial coordinates from the angular and spin coordinates, and the *spin-orbitals* take the general form

$$\phi_{nlsjm}(\mathbf{q}) = \frac{1}{r}\begin{pmatrix} P_{nlj}(r)\Omega_{lsjm}(\theta,\varphi) \\ \mathrm{i}Q_{nlj}(r)\Omega_{\tilde{l}sjm}(\theta,\varphi) \end{pmatrix}, \tag{2.22}$$

where $P_{nlj}(r)$ and $Q_{nlj}(r)$ are, respectively, the large and small components of the radial function and $\Omega_{lsjm}(\theta,\varphi)$ are the two-component spin-angular functions, or else the *spherical spinors*. The *spherical spinors* $\Omega_{lsjm}(\theta,\varphi)$ are constructed from the coupling of the *spherical harmonics* $Y_{lm_l}(\theta,\varphi)$ with the *spinors* $\chi_{\frac{1}{2},m_s}$, that is

$$\Omega_{lsjm}(\theta,\varphi) = \sum_{m_l,m_s} \langle l, \frac{1}{2}; m_l, m_s | j, m\rangle Y_{l,m_l}(\theta,\varphi)\chi_{\frac{1}{2},m_s}, \tag{2.23}$$

where $\langle l, \frac{1}{2}; m_l, m_s | j, m\rangle$ is a Clebsch-Gordan (CG) coefficient and

$$\chi_{\frac{1}{2},\frac{1}{2}} = \begin{pmatrix} 1 \\ 0 \end{pmatrix}, \qquad \chi_{\frac{1}{2},-\frac{1}{2}} = \begin{pmatrix} 0 \\ 1 \end{pmatrix}. \tag{2.24}$$

The *spherical spinors* satisfy the orthonormality conditions, just as the *spherical harmonics* do.

From the coupling of the angular momentum and spin, it follows that $j = l \pm s$ with $s = \frac{1}{2}$ and, for a given value of j, the l quantum number can take two possible values, i.e., $l = j \pm \frac{1}{2}$. In (2.22), the *spherical spinors* of the large and small radial components are obtained by, respectively, choosing l and $\tilde{l}$, which are associated to each other with the relation

$$\tilde{l} = \begin{cases} l+1 & \text{for } \; j = l + \frac{1}{2} \\ l-1 & \text{for } \; j = l - \frac{1}{2}. \end{cases} \tag{2.25}$$

In this manner, the pair of two-component spinors will have opposite parity. Besides the parity π, the *spherical spinors* are eigenfunctions of $\mathbf{l}$ and $\mathbf{s}$, as well as the total angular momentum $\mathbf{j}$, so that

$$\begin{aligned} \mathbf{l}^2\Omega_{lsjm} &= l(l+1)\Omega_{lsjm}, \\ \mathbf{s}^2\Omega_{lsjm} &= \frac{1}{2}(\frac{1}{2}+1)\Omega_{lsjm}, \\ \mathbf{j}^2\Omega_{lsjm} &= j(j+1)\Omega_{lsjm}, \\ j_z\Omega_{lsjm} &= m\Omega_{lsjm}. \end{aligned} \tag{2.26}$$

The quantum numbers j and m are not sufficient to uniquely describe an atomic state, and the modified Dirac Hamiltonian of Eq. (2.16) does not commute with $\mathbf{l}$ and $\mathbf{s}$. Since the Hamiltonian (2.16) commutes with $\mathbf{j}^2, \mathbf{l}^2$ and $\mathbf{s}^2$, it also commutes with $\mathbf{s}\cdot\mathbf{l}$, and it is convenient to introduce the additional quantum

number κ as the eigenvalue of the operator $\mathcal{K} = -(1 + \mathbf{j}^2 - \mathbf{l}^2 - \mathbf{s}^2) = -1 - \boldsymbol{\sigma} \cdot \mathbf{l}$, so that

$$\mathcal{K}\Omega_{lsjm} = \kappa\Omega_{lsjm}, \tag{2.27}$$

where

$$\kappa = \begin{cases} -(l+1) & \text{for } j = l + \frac{1}{2} \\ l & \text{for } j = l - \frac{1}{2}. \end{cases} \tag{2.28}$$

In doing so, we can rewrite the *spin-orbitals* of (2.22) as

$$\phi_{n\kappa m}(\mathbf{q}) = \frac{1}{r} \begin{pmatrix} P_{n\kappa}(r)\Omega_{\kappa m}(\theta, \varphi) \\ \mathrm{i}Q_{n\kappa}(r)\Omega_{-\kappa m}(\theta, \varphi) \end{pmatrix}. \tag{2.29}$$

We note that each quantum state is now uniquely described by the quantum number κ.

The *spherical spinors* are linearly independent, and after inserting the *spin-orbitals* of Eq. (2.29) in the wave equation (2.20), we get

$$\begin{aligned} &(V_{\mathrm{av}}(r) - E)P_{n\kappa}(r) - c\left(\frac{\mathrm{d}}{\mathrm{d}r} - \frac{\kappa}{r}\right)Q_{n\kappa}(r) = 0 \\ &c\left(\frac{\mathrm{d}}{\mathrm{d}r} + \frac{\kappa}{r}\right)P_{n\kappa}(r) + (V_{\mathrm{av}}(r) - 2c^2 - E)Q_{n\kappa}(r) = 0, \end{aligned} \tag{2.30}$$

where the zero energy E corresponds to the electron ionization limit. These equations are solved for each electron i, in the common average potential V_{av} produced by the remaining $N-1$ electrons. In GRASP2018, the radial functions $\{P_{n\kappa}(r), Q_{n\kappa}(r)\}$ are defined on a grid

$$r_i = A(e^{B(i-1)} - 1), \qquad i = 1, ..., i_{max}, \tag{2.31}$$

where A and B are constants, and the default value for i_{max} is 590. This logarithmic grid normally contains enough points that properly capture the entire pattern of the large and small components of the continuous radial function.

For bound states, the radial orbitals must be square integrable and must also satisfy the orthonormality condition, i.e,

$$\int_0^\infty [P_{n\kappa}(r)P_{n'\kappa}(r) + Q_{n\kappa}(r)Q_{n'\kappa}(r)]\mathrm{d}r = \delta_{nn'}. \tag{2.32}$$

Further, the radial amplitudes should vanish at the endpoints, that is $r \to 0$ and $r \to \infty$. Near the origin, the radial functions can be expanded in power series of the form

$$P_{n\kappa}(r) = r^s(p_0 + p_1 r + ...), \qquad Q_{n\kappa}(r) = r^s(q_0 + q_1 r + ...), \tag{2.33}$$

where p_i, q_i, and the index $s > -1/2$ are constants that depend on the nuclear potential model and the *spin-orbital*, and are determined by coupled linear algebraic equations [24]. For large r, the radial functions reduce asymptotically to zero. By convention, the first oscillation of the $P_{n\kappa}(r)$ is chosen to be positive. The number of nodes in the large component $P_{n\kappa}(r)$ is given by $n-l-1$, just as in the non-relativistic case, while the number of nodes in the small component $Q_{n\kappa}(r)$ is given by $n-l-1$ for $\kappa < 0$ and $n-l$ for $\kappa > 0$. Node counting is essential in SCF methods, such as the MCDHF method (see Section 2.3), ensuring that the desired physical states are found.

2.2.2 Configuration state functions

The Hamiltonian $\mathcal{H}_0$ of (2.15) is invariant with respect to permutations of the electron coordinates $\mathbf{q_i}$ and thus, any permutation in the product function of (2.19) also leads to an eigenfunction. According to the Pauli *exclusion principle* [34] only wave functions that are anti-symmetric describe physical atomic states and such wave functions can be represented by what is known as a *Slater determinant*

$$\Phi(\mathbf{q}_1, ..., \mathbf{q}_N) = \frac{1}{\sqrt{N!}} \begin{vmatrix} \phi_{\alpha_1}(\mathbf{q}_1) & \phi_{\alpha_1}(\mathbf{q}_2) & \dots & \phi_{\alpha_1}(\mathbf{q}_N) \\ \phi_{\alpha_2}(\mathbf{q}_1) & \phi_{\alpha_2}(\mathbf{q}_2) & \dots & \phi_{\alpha_2}(\mathbf{q}_N) \\ \dots & \dots & \dots & \dots \\ \phi_{\alpha_N}(\mathbf{q}_1) & \phi_{\alpha_N}(\mathbf{q}_2) & \dots & \phi_{\alpha_N}(\mathbf{q}_N) \end{vmatrix}, \tag{2.34}$$

which, in a more compact manner, is written as

$$\Phi(\mathbf{q}_1, ..., \mathbf{q}_N) = \frac{1}{\sqrt{N!}} \sum_{\mathcal{P}} (-1)^p \mathcal{P} \prod_{i=1}^{N} \phi_{\alpha_i}(\mathbf{q}_i), \tag{2.35}$$

where $\mathcal{P}$ is an operator that permutes the coordinates of the electrons, with the sum $\mathcal{P}$ being over all possible $N!$ permutations, p is the parity of the permutation, and $\alpha_i = n_i \kappa_i m_i$ is the quantum label that uniquely describes a Dirac *spin-orbital*.

The relativistic N-electron Hamiltonian $\mathcal{H}^{DC}$, which also includes the electron-electron Coulomb interaction, commutes with the total angular momentum operator $\mathbf{J} = \mathbf{j}_1 + \mathbf{j}_2 + ... + \mathbf{j}_N$. Hence, we seek many-electron solutions to the eigenvalue problem (2.13) that are eigenfunctions of $\mathbf{J}^2$ and J_z, with J and M being good quantum numbers together with the parity P, so that

$$\begin{aligned} &\Pi\Phi = P\Phi, \;\; P = (-1)^{l_1+...+l_N}, \\ &\mathbf{J}^2\Phi = J(J+1)\Phi, \\ &J_z\Phi = M\Phi, \;\; M = -J, -J+1, ..., J. \end{aligned} \tag{2.36}$$

The approximate wave functions (2.35) in the form of *Slater determinants* are usually not eigenfunctions of $\mathbf{J}^2$. However, by taking linear combinations of *Slater determinants* belonging to the same configuration[2], we can obtain wave functions with the desired J-symmetry. These functions are better approximations to the exact wave functions than the *Slater determinants* themselves. Each such solution defines a configuration state function (CSF), denoted as

$$\Phi(\gamma PJM_J) \;\; \equiv \;\; |\gamma PJM_J\rangle, \tag{2.37}$$

where γ represents the configuration, the angular momentum coupling tree, and other quantum numbers that are necessary to entirely describe the CSF. We require that the CSFs form an orthonormal set, so that

$$\langle \gamma_\mu P_\mu J_\mu M_\mu | \gamma_\nu P_\nu J_\nu M_\nu \rangle = \delta_{\mu\nu}. \tag{2.38}$$

Alternatively, a CSF can be constructed from products of *spin-orbitals* using a recursive method in terms of coefficients of fractional parentage (CFPs) and explicit antisymmetrization. In GRASP2018, the latter approach is applied, which is described in detail in the review article by Fischer et al. [27] and the book by Grant [24].

2.2.3 Atomic state functions

The single CSF approach does not capture effects that arise from the correlated motion of the electrons. To include *electron correlation* [35] (for more details see Section 2.5), we must seek a better approximation to the exact wave functions. For a certain parity P, there is a number of CSFs coupled to the same total

[2]That is determinants with the same set of n and l quantum numbers, but with different m_l and m_s quantum numbers.

angular momentum J. Each set of CSFs with the same P and J quantum numbers form a basis for a function space of approximate wave functions, which are known as atomic state functions (ASFs). An ASF, $\Psi(\Gamma PJ)$, is then written as a linear combination of CSFs, $\Phi(\gamma_\mu PJ)$, i.e.

$$\Psi(\Gamma PJ) \equiv |\Gamma PJ\rangle = \sum_{\mu=1}^{N_{\rm CSF}} c_{\gamma_\mu J}\Phi(\gamma_\mu PJ), \tag{2.39}$$

where $c_{\gamma_\mu J} = \langle\gamma_\mu PJ|\Gamma PJ\rangle$ are the mixing coefficients of the expansion, which as follows from (2.38) must satisfy the normalization condition

$$\sum_{\mu=1}^{N_{\rm CSF}} c^2_{\gamma_\mu J} = 1. \tag{2.40}$$

The label Γ of the ASF is normally the same as the label γ_μ of the dominating CSF μ, that is the CSF with the largest absolute value of the coefficient $c_{\gamma_\mu J}$ in the expansion. Considering the fact that the coefficients $c_{\gamma_\mu J}$ are independent of the quantum number M, in Eq. (2.39) the latter was suppressed for brevity.

In atomic structure calculations, it is most likely that we are interested in more than one atomic state, represented by multiconfiguration functions as Eq. (2.39) suggests. When performing multiconfiguration calculations that target multiple states $|\Gamma^i PJ^i\rangle$, $i = 1, ..., N_{\rm ASF}$ at the same time, the different ASFs are chosen to be orthonormal, so that

$$(\mathbf{c}_{\Gamma^i J^i})^\dagger \mathbf{c}_{\Gamma^j J^j} = \delta_{ij}, \tag{2.41}$$

where $\mathbf{c}_{\Gamma J}$ is a column vector combining the mixing coefficients $\{c_{\gamma_\mu J}, \mu = 1, ..., N_{\rm CSF}\}$ that take part in the representation of an atomic state.

2.3 Multiconfiguration Dirac-Hartree-Fock

In Section 2.2, it was shown that the wave function of an atomic state can be approximated by a superposition of CSFs $\Phi(\gamma_\mu PJ)$, according to Eq. (2.39). The CSFs are, however, constructed based on the assumption that the one-electron Dirac orbitals $\phi_{n\kappa m}$, with radial parts $\{P_{n\kappa}(r), Q_{n\kappa}(r)\}$, arise from a general *central field* approximation. To determine the radial orbitals and mixing coefficients that yield the best approximation to the exact wave functions, the MCDHF method is employed. In the MCDHF method, the large and small components of the radial functions are obtained by solving a set of SCF equations that result from applying the *variational principle* [36, 37] on the energy

functional of one or more ASFs, with additional terms ensuring orthonormality of the orbitals. The SCF MCDHF equations are presented after a brief introduction to the calculation of the matrix elements that are needed for the construction of the energy functional.

2.3.1 Energy matrix elements

Approximate eigenenergies of the atom at hand are obtained as diagonal expectation values of the approximate Dirac-Coulomb Hamiltonian, i.e.,

$$E_{\Gamma J} = \langle \Gamma P J | \mathcal{H}^{\mathrm{DC}} | \Gamma P J \rangle = (\mathbf{c}_{\Gamma J})^{\dagger} \mathbf{H} \mathbf{c}_{\Gamma J}, \tag{2.42}$$

where $\mathbf{H}$ is the Hamiltonian matrix with elements

$$H_{\mu\nu} = \langle \gamma_\mu P J | \mathcal{H}^{\mathrm{DC}} | \gamma_\nu P J \rangle. \tag{2.43}$$

The matrix elements $H_{\mu\nu}$ are expressed as sums of products of *spin-angular coefficients* and *radial integrals*, i.e.,

$$H_{\mu\nu} = \sum_{ab} t_{ab}^{\mu\nu} I(a,b) + \sum_{abcd;k} v_{abcd;k}^{\mu\nu} R^k(ab,cd), \tag{2.44}$$

where, e.g., a represents the orbital in the subshell $n_a\kappa_a$ occupied in the CSF μ.

In Eq. (2.44), the one-particle contributions (2.6) give rise to the *spin-angular coefficients* $t_{ab}^{\mu\nu}$ and the *radial integrals* $I(a,b)$ given by

$$\begin{aligned} I(a,b) = \delta_{\kappa_a\kappa_b} \int_0^\infty \big[& P_{n_a\kappa_a}(r) V_{\mathrm{nuc}}(r) P_{n_b\kappa_b}(r) \\ & - c P_{n_a\kappa_a}(r) \left(\frac{d}{dr} - \frac{\kappa}{r} \right) Q_{n_b\kappa_b}(r) \\ & + c\, Q_{n_a\kappa_a}(r) \left(\frac{d}{dr} + \frac{\kappa}{r} \right) P_{n_b\kappa_b}(r) \\ & + Q_{n_a\kappa_a}(r) \left(V_{\mathrm{nuc}}(r) - 2c^2 \right) Q_{n_b\kappa_b}(r) \big]\, dr, \end{aligned} \tag{2.45}$$

where the condition $\kappa_a = \kappa_b = \kappa$ follows from the orthogonality property of the *spherical spinors*. In the special case of diagonal matrix elements, $t_{aa}^{\mu\mu}$ is given by the occupation number w_a^μ of the orbital a in the CSF μ. The two-particle

contributions (2.7) are evaluated by first expanding the Coulomb potential in terms of Legendre polynomials, so that

$$\frac{1}{r_{ij}} = \sum_{k=0}^{\infty} \frac{r_<^k}{r_>^{k+1}} P_k(\cos\omega), \tag{2.46}$$

where ω is the angle between the position vectors $\boldsymbol{r}_i$ and $\boldsymbol{r}_j$, $r_< \equiv \min(r_i, r_j)$, and $r_> \equiv \max(r_i, r_j)$. In the coupled tensorial form, the above equation takes the form

$$\frac{1}{r_{ij}} = \sum_{k=0}^{\infty} \frac{r_<^k}{r_>^{k+1}} (\mathbf{C}^{(k)}(\theta_i, \phi_i) \cdot \mathbf{C}^{(k)}(\theta_j, \phi_j)), \tag{2.47}$$

where the $\mathbf{C}^{(k)}(\theta_i, \phi_i)$ are renormalized spherical harmonics of rank k. Eq. (2.47) finally yields the *spin-angular coefficients* $v^{\mu\nu}_{abcd;k}$ and the *relativistic Slater integrals* $R^k(ab, cd)$, which are given by

$$\begin{aligned} R^k(ab, cd) = & \int_0^{\infty} [P_{n_a\kappa_a}(r) P_{n_c\kappa_c}(r) \\ & + Q_{n_a\kappa_a}(r) Q_{n_c\kappa_c}(r)] \frac{1}{r} Y^k(bd; r) dr, \end{aligned} \tag{2.48}$$

with the relativistic Hartree Y^k-functions defined by

$$\begin{aligned} Y^k(ab; r) = & \; r \int_0^{\infty} \frac{r_<^k}{r_>^{k+1}} [P_{n_a\kappa_a}(s) P_{n_b\kappa_b}(s) \\ & + Q_{n_a\kappa_a}(s) Q_{n_b\kappa_b}(s)] \, ds, \end{aligned} \tag{2.49}$$

where $r_<$ ($r_>$) denotes the smaller (larger) of r and s. By introducing the Y-functions, Hartree showed in [38] that the double *radial integrals* of the two-body Coulomb interaction could be evaluated through a pair of one-dimensional integrals given by the Eqs. (2.48) and (2.49).

In GRASP2018, the evaluation of the *spin-angular coefficients* $t^{\mu\nu}_{ab}$ and $v^{\mu\nu}_{abcd;k}$, needed for constructing the Hamiltonian matrix elements $H_{\mu\nu}$, relies on the latest angular-momentum methods developed by Gaigalas et al. [39, 40]. These methods use algebraic expressions for matrix elements adapted for spin-angular integrations in jj-coupling, involving the calculation of reduced CFPs and completely reduced matrix elements of double tensors.

2.3.2 The MCDHF equations

In the publications included in this thesis, the wave functions of the targeted atomic states were simultaneously determined using the extended optimal level (EOL) scheme [24, 26]. The EOL energy functional is expressed in terms of the statistical weight of each targeted state $|\Gamma^i J^i\rangle$, i.e.,

$$\mathcal{F}(\{c\},\{P\},\{Q\}) = \frac{\sum_{i=1}^{N_{\rm ASF}}(2J^i+1)\;E_{\Gamma^i J^i}}{\sum_{i=1}^{N_{\rm ASF}}(2J^i+1)} + \sum_{ab}\;\delta_{\kappa_a\kappa_b}\lambda_{ab}\,\mathcal{C}_{ab}, \tag{2.50}$$

where the orthonormality of the radial orbitals is ensured by introducing the *Langrange multipliers* λ_{ab} for each orthonormality constraint

$$\mathcal{C}_{ab} \equiv \int_0^\infty [P_{n_a\kappa_a}(r)P_{n_b\kappa_b}(r) + Q_{n_a\kappa_a}(r)Q_{n_b\kappa_b}(r)]\,dr - \delta_{n_a n_b} = 0. \tag{2.51}$$

The energy functional (2.50) is optimized by requiring that it remains stationary with respect to variations in both the mixing coefficients $c_{\gamma_\mu J}$ and the radial parts $\{P_{n\kappa}(r), Q_{n\kappa}(r)\}$ of the *spin-orbitals*.

For a specific set of radial functions $\{P_{n\kappa}(r), Q_{n\kappa}(r)\}$, initially provided by e.g. (screened) hydrogenic or Thomas-Fermi orbitals, the optimal values of the mixing coefficients $\mathbf{c}_{\Gamma J} = \{c_{\gamma_\mu J}, \mu = 1, ..., N_{\rm CSF}\}$ are obtained as solutions to the RCI problem

$$\mathbf{H}\mathbf{c}_{\Gamma J} = E_{\Gamma J}\mathbf{c}_{\Gamma J}. \tag{2.52}$$

Given a set of mixing coefficients $c_{\gamma_\mu J}$, the stationary condition with respect to coupled variations in the radial orbitals, i.e., $\{\delta P_{n\kappa}(r), \delta Q_{n\kappa}(r)\}$, leads to a set of coupled integro-differential equations similar to (2.30)

$$w_a \begin{bmatrix} V(a;r) & -c\left[\dfrac{d}{dr} - \dfrac{\kappa_a}{r}\right] \\ c\left[\dfrac{d}{dr} + \dfrac{\kappa_a}{r}\right] & V(a;r) - 2c^2 \end{bmatrix} \begin{bmatrix} P_{n_a\kappa_a}(r) \\ Q_{n_a\kappa_a}(r) \end{bmatrix} = \sum_b \epsilon_{ab}\delta_{\kappa_a\kappa_b} \begin{bmatrix} P_{n_b\kappa_b}(r) \\ Q_{n_b\kappa_b}(r) \end{bmatrix}, \tag{2.53}$$

which are known as the MCDHF equations. In (2.53), w_a is the generalized occupation number of the orbital a and ϵ_{ab} are energy parameters related to

the *Lagrange multipliers*. To incorporate the correct qualitative features of the exact wave functions, the radial orbitals must satisfy the boundary conditions discussed in Subsection 2.2.1. Subject to these conditions, the MCDHF equations are solved for each subshell $n_a\kappa_a$, on the logarithmic grid (2.31), using a finite difference method.

The average and *central field* MCDHF potential $V(a;r)$ is built from the nuclear, *direct*, and *exchange* contributions, i.e.,

$$V(a;r) = V_{\text{nuc}}(r) + Y(a;r) + \overline{X}(a;r). \tag{2.54}$$

Variations of the *Slater integrals* of the type $R^k(ab;ab)$, weighted with the angular coefficients and the state averaged mixing coefficients, contribute to the direct potential $Y(a;r)$, whereas variations of the other $R^k(ab;cd)$ integrals and the off-diagonal $I(a,b)$ integrals, again weighted with the angular coefficients and the state averaged mixing coefficients, contribute to the non-local *exchange* potential $\overline{X}(a;r)$. The expressions for the *direct* and *exchange* potentials, involving both diagonal and off-diagonal contributions are rather lengthy, and thus not provided here. Instead, the interested reader is referred to Dyall et al. [26] or the book by Grant [24].

2.3.3 Self-consistent field procedure

Since the *direct* and *exchange* potentials depend on the radial orbitals, the RCI problem (2.52) and MCDHF equations (2.53) are simultaneously solved through an iterative non-linear procedure. This procedure is continued until self-consistency is reached, with respect to both radial orbitals and mixing coefficients, based on a specified convergence criterion. In what follows, we summarize the SCF calculations in steps (see also Figure 2.1):

1. Given initial estimates for the radial orbitals, the energy matrix elements are evaluated. The mixing coefficients are obtained by a first diagonalization of the Hamiltonian matrix.

2. The energy functional (2.50) is constructed and the stationary condition is applied; first, with respect to variations in the radial orbitals (step 3) and then with respect to variations in the mixing coefficients (step 4).

3. The MCDHF equations (2.53) are solved using the *direct* and *exchange* contributions to the potential (2.54) from the previously estimated radial orbitals. An improved estimate for the radial orbitals is obtained.

4. The RCI problem (2.52) is solved after utilizing the new set of radial orbitals. An improved estimate for the mixing coefficients is obtained.

5. The convergence of both radial orbitals and mixing coefficients is examined. If the convergence criterion is met, the SCF calculations are completed, yielding the final orbital basis and mixing coefficients. If not, the process is repeated from step 2.

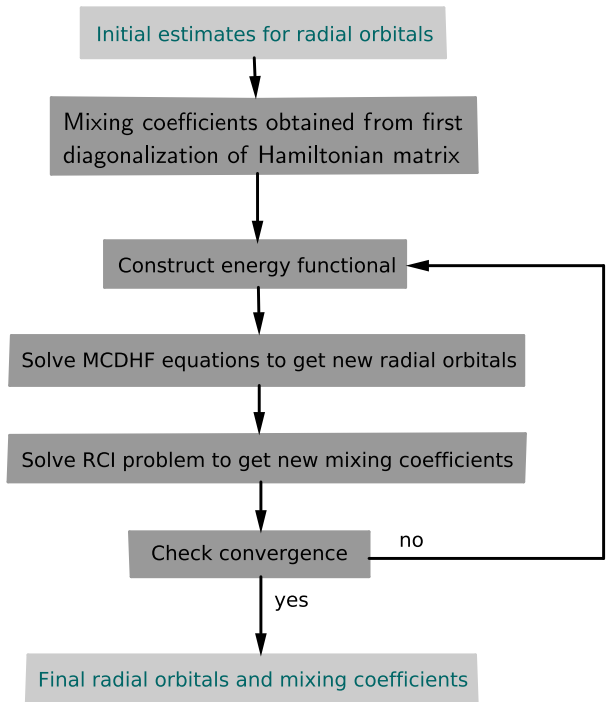

Figure 2.1: The algorithm of the SCF MCDHF scheme. The first and last instants, respectively, correspond to the required input and the output of the SCF calculations.

2.3.4 Relativistic configuration interaction

The SCF MCDHF method is employed to generate the orbital basis. Given this basis, the final wave functions of the targeted states are determined in subsequent RCI calculations, based on the Dirac-Coulomb-Breit and QED Hamiltonian (2.12). In the RCI calculations, the *spin-orbitals* defining the basis are fixed and only the mixing coefficients $\mathbf{c}_{\Gamma J}$ are evaluated by diagonilizing the

Hamiltonian matrix. The eigenvalues of the Hamiltonian matrix represent the total energies of the targeted states.

2.4 Computation of Atomic Properties

Once the wave functions have been determined from MCDHF and RCI calculations, measurable properties can be obtained by evaluating the expectation values, or, in the case of transitions, the amplitudes, of appropriate tensor operators. According to the Wigner-Eckart theorem [41], the matrix elements of a general spherical tensor operator $O_q^{(k)}$ of rank k can be written as

$$\langle \Gamma PJM|O_q^{(k)}|\Gamma' P' J' M'\rangle = \\ (-1)^{J-M} \begin{pmatrix} J & k & J' \\ -M & q & M' \end{pmatrix} \langle \Gamma PJ||\mathbf{O}^{(k)}||\Gamma' P' J'\rangle, \qquad (2.55)$$

where the entire dependence on the magnetic quantum numbers is factored out as a CG coefficient. The physical nature of the operator is entirely contained in the reduced matrix element $\langle \Gamma PJ||\mathbf{O}^{(k)}||\Gamma' P' J'\rangle$. After inserting the multiconfiguration expansions (2.39), the reduced matrix element is given by

$$\langle \Gamma PJ||\mathbf{O}^{(k)}||\Gamma' P' J'\rangle = \sum_{\mu,\nu} c_{\gamma_\mu J} c_{\gamma'_\nu J'} \langle \gamma_\mu PJ||\mathbf{O}^{(k)}||\gamma'_\nu P' J'\rangle. \qquad (2.56)$$

The reduced matrix elements between CSFs are, in turn, expressed as sums over products of *spin-angular coefficients* [39, 40] and *radial integrals*. The latter depend only on the *spin-orbitals* and the nature of the interaction operator.

2.4.1 Transition properties

An electron interacts with the electromagnetic field and transitions between atomic states are observed. Following the work by Grant [24], the *rate* (or *probability*) $A^{(k)}$ for spontaneous emission, from an upper state $|\Gamma' P' J' M'\rangle$ to any of the $2J+1$ states $|\Gamma PJM\rangle$ of lower energy, is given by

$$A^{(k)}(\Gamma' P' J', \Gamma PJ) = \frac{2\omega}{c} \frac{1}{(2k+1)(2J'+1)} |\langle \Gamma PJ\|\mathbf{T}^{(k)}\|\Gamma' P' J'\rangle|^2, \qquad (2.57)$$

where ω is the angular frequency of the transition and $\mathbf{T}^{(k)} = \sum_{i=1}^{N} \mathbf{t}^{(k)}(i)$ is the electromagnetic multipole operator of rank k, with the sum running over the

number N of electrons. Instead of giving the *rate*, the strength of a transition is often expressed in terms of the *weighted oscillator strength* $gf^{(k)}$, which is defined as

$$gf^{(k)}(\Gamma' P' J', \Gamma P J) = \frac{1}{\omega} \frac{1}{(2k+1)} |\langle \Gamma P J \| \mathbf{T}^{(k)} \| \Gamma' P' J' \rangle|^2. \tag{2.58}$$

When the observed spectra consist of absorption lines, data of gf parameters are preferred.

The *lifetime* $\tau_{\Gamma' J'}$ of an excited state $|\Gamma' P' J'\rangle$ is given in terms of a sum over transition rates for all the possible decay channels, so that

$$\tau_{\Gamma' J'} = \frac{1}{\sum_{k, \Gamma P J} A^{(k)}(\Gamma' P' J', \Gamma P J)}. \tag{2.59}$$

In Figure 2.2, we assume that an upper state $u \equiv |\Gamma' P' J'\rangle$ has three possible decay channels, with *rates* A_1, A_2 and A_3. The *radiative lifetime* of this state is given by $\tau_u = 1/(A_1 + A_2 + A_3)$. Although single line properties, such as *transition rates* and *weighted oscillator strengths* are not easy to measure, *radiative lifetime* measurements are possible. If the latter are precise enough, they can be used to benchmark the theoretical predictions.

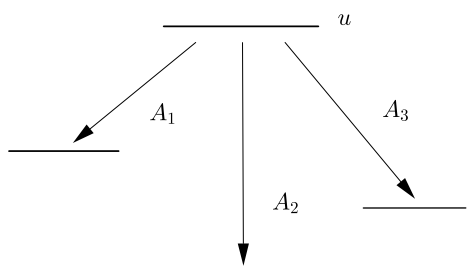

Figure 2.2: An example of an upper state u having three possible decay channels. The corresponding *transition rates* for each channel are A_1, A_2 and A_3.

Another quantity that can experimentally be obtained is the *branching fraction* $\mathcal{Q}$, which represents the relative intensity of lines originating from the same upper state $u \equiv |\Gamma' P' J'\rangle$ and is expressed as

$$\mathcal{Q} = \tau_{\Gamma' J'} \sum_k A^{(k)}(\Gamma' P' J', \Gamma P J). \tag{2.60}$$

According to (2.60), in the example of Figure 2.2, the *branching fraction* of, e.g, "transition 1" is given by $\mathcal{Q}_1 = A_1/(A_1 + A_2 + A_3)$. It follows that $A_1 = \mathcal{Q}_1/\tau_u$, $A_2 = \mathcal{Q}_2/\tau_u$ and so forth. Thus, by combining measurements of *branching fractions* with reference data of *lifetimes*, *transition rates* and *weighted oscillator strengths* can be derived [42].

The one-particle radiation field operator $\mathbf{T}^{(k)}$ can be separated into individual operators for multipole transitions of electric (Ek) and magnetic (Mk) type. In general, electric dipole (E1) transitions dominate, yielding the largest *rates* and contributions to the *radiative lifetimes*. In Paper I, E1 *transition rates* were computed and *radiative lifetimes* were deduced for the systems of singly ionized and neutral aluminium, i.e., Al II and Al I.

The electric multipole operators contain a gauge parameter. This parameter determines whether the matrix elements (2.55) are computed in the *Babushkin* or the *Coulomb* gauge, which in the non-relativistic limit, respectively, correspond to the *length* and the *velocity* form. The two forms are equivalent for hydrogenic wave functions, but they often result in different values when approximate many-electron wave functions are used. Producing transition data, for many-electron systems, that are weakly sensitive to the choice of gauge requires that the obtained wave functions are accurately represented in regions of space both near and far from the nucleus. This is an important aspect of atomic structure calculations and part of the discussion in Chapter 3.

In the systems of Al II and Al I, relativistic effects are expected to be small. This permits us to limit the discussion on the computations of the electric dipole reduced matrix elements to the non-relativistic limit. For the explicit relativistic expressions, the reader is referred to [24] and [43]. In the non-relativistic limit, the electric dipole reduced matrix elements are, in the *length* and the *velocity* form, respectively, given by

$$\langle \Gamma P J || \sum_{i=1}^{N} r_i \mathbf{C}^{(1)}(\theta_i, \phi_i) || \Gamma' P' J' \rangle \tag{2.61}$$

and

$$\frac{1}{E_{\Gamma' J'} - E_{\Gamma J}} \langle \Gamma P J || \sum_{i=1}^{N} \boldsymbol{\nabla}_i^{(1)} || \Gamma' P J' \rangle, \tag{2.62}$$

where $\mathbf{C}^{(1)}$ is the renormalized spherical harmonic of rank 1, $\boldsymbol{\nabla}_i^{(1)}$ is the gradient tensor operator of rank 1, and $E_{\Gamma' J'} - E_{\Gamma J}$ is the transition energy [44]. The reduced matrix elements (2.61) and (2.62) involve, respectively, sums over *radial*

transition integrals of the kind

$$\int_0^\infty P(r) r P'(r)\, dr \tag{2.63}$$

and

$$\int_0^\infty P(r) \frac{d}{dr} P'(r)\, dr, \tag{2.64}$$

weighted with the products of the mixing coefficients of the CSFs and the *angular coefficients*. In (2.63) and (2.64), $P'(r)$ and $P(r)$ are the radial functions of the large components of the Dirac *spin-orbitals* (2.29) that build the CSFs of the upper state $|\Gamma' P' J'\rangle$ and the lower state $|\Gamma P J\rangle$, respectively.

The agreement between the values of the reduced matrix elements (2.61) and (2.62), respectively, evaluated in the *length* and the *velocity* form is used to indicate the accuracy of the wave functions [45]. Accordingly, as an estimate of the uncertainty of computed transition data, such as *transition rates* A, we could use (see [46])

$$dT = \frac{|A_l - A_v|}{\max(A_l, A_v)}. \tag{2.65}$$

Although the uncertainties dT should be used in a statistical manner for a group of transitions with similar properties, as done in Paper I, individual dT values point out problematic transitions, which could be further analyzed.

2.4.2 Isotope shifts

Due to isotope specific properties of atomic nuclei, spectral lines from different isotopes of the same element display a small shift in energy, known as the isotope shift (IS). Given a transition k, the line IS for a pair of isotopes A, A' is defined as

$$\Delta E_{k,\mathrm{IS}}^{A,A'} = \delta E_{u,\mathrm{IS}}^{A,A'} - \delta E_{l,\mathrm{IS}}^{A,A'}, \tag{2.66}$$

where $\delta E_{u,\mathrm{IS}}^{A,A'}$ and $\delta E_{l,\mathrm{IS}}^{A,A'}$ are, respectively, the shifts in the energies of the upper state u and lower state l taking part in the transition (see also Figure 2.3). By far the most important isotope properties to consider are the finite mass and the extended charge distribution of the nucleus. Thus, the line IS is, normally, broken down into the mass shift (MS) and the field shift (FS) contributions, which are computed separately (see below) [15, 2].

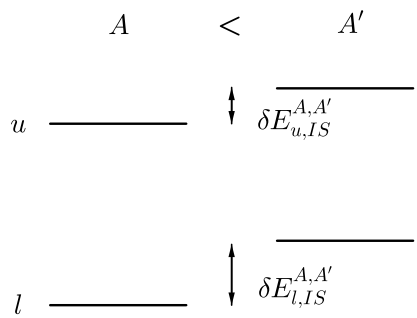

Figure 2.3: The upper u and lower l levels that are, respectively, associated with an atomic transition k, in the isotopes A and A' of an element. The shift in energy is different in magnitude for each of the upper and lower levels of the two isotopes, resulting in the observed IS for the transition k.

For a specific state $|\Gamma PJM\rangle$, the level MS is given by

$$\delta E^{A,A'}_{\Gamma J,\mathrm{MS}} = (K_{\Gamma J,\mathrm{NMS}} + K_{\Gamma J,\mathrm{SMS}})\frac{M^{A'} - M^{A}}{M^{A}M^{A'}}, \tag{2.67}$$

where M^A and $M^{A'}$ are the nuclear masses of the isotopes A and A'. The normal mass shift $K_{\Gamma J,\mathrm{NMS}}$ and the specific mass shift $K_{\Gamma J,\mathrm{SMS}}$ parameters are, respectively, defined by

$$\frac{K_{\Gamma J,\mathrm{NMS}}}{M^A} = \frac{1}{\sqrt{2J+1}}\langle \Gamma PJ||\mathcal{H}^A_{\mathrm{NMS}}||\Gamma PJ\rangle \tag{2.68}$$

and

$$\frac{K_{\Gamma J,\mathrm{SMS}}}{M^A} = \frac{1}{\sqrt{2J+1}}\langle \Gamma PJ||\mathcal{H}^A_{\mathrm{SMS}}||\Gamma PJ\rangle, \tag{2.69}$$

where

$$\begin{aligned}\mathcal{H}^A_{\mathrm{NMS}} = \frac{1}{2M^A}\sum_{i=1}^{N}\Bigg(&\mathbf{p}_i^2 - \frac{\alpha Z}{r_i}\boldsymbol{\alpha}_i\cdot\mathbf{p}_i \\ &-\frac{\alpha Z}{r_i}\left(\boldsymbol{\alpha}_i\cdot\mathbf{C}^{(1)}(\theta_i,\phi_i)\right)\mathbf{C}^{(1)}(\theta_i,\phi_i)\cdot\mathbf{p}_i\Bigg)\end{aligned} \tag{2.70}$$

and

$$\mathcal{H}^A_{\rm SMS} = \frac{1}{2M^A}\sum_{i\neq j}^{N}\Bigg(\mathbf{p}_i\cdot\mathbf{p}_j - \frac{\alpha Z}{r_i}\boldsymbol{\alpha}_i\cdot\mathbf{p}_j \\ -\frac{\alpha Z}{r_i}\Big(\boldsymbol{\alpha}_i\cdot\mathbf{C}^{(1)}(\theta_i,\phi_i)\Big)\mathbf{C}^{(1)}(\theta_i,\phi_i)\cdot\mathbf{p}_j\Bigg), \tag{2.71}$$

are, respectively, the normal mass shift and the specific mass shift operators, given for the reference isotope A.

In GRASP2018, the nuclear potential results from a two-parameter Fermi nuclear charge density distribution, which is given by

$$\rho(r) = \frac{\rho_0}{1+e^{\frac{r-c}{a}}}, \tag{2.72}$$

where ρ_0 is the normalization constant, a is related to the skin thickness t of the distribution by $t = 4\ln(3)a$, and c is determined based on the value of a and the selected rms radius $\sqrt{\langle r^2\rangle}$. The skin thickness, which defines the interval where the density decreases from 90% to 10% of $\rho(0)$, has a default value $t = 2.3$ fm. The level FS can then be obtained by performing two separate variational calculations for the isotopes A and A' and subtracting the energies.

When several isotopes are considered, the above-mentioned "exact" calculations are cumbersome, computationally expensive, and, in general, the result of subtracting large numbers, which is likely to be unstable. Alternatively, we can use an approach based on perturbation theory. Within the framework of perturbation, the first-order level FS, for a state $|\Gamma PJM\rangle$, can be expressed as

$$\delta E^{(1)A,A'}_{\Gamma J,\rm FS} = -\int_{R^3}\Big(V^{A'}_{\rm nuc}(\boldsymbol{r}) - V^{A}_{\rm nuc}(\boldsymbol{r})\Big)\rho^e_{\Gamma J}(\boldsymbol{r})d^3\boldsymbol{r}, \tag{2.73}$$

where $V^A_{\rm nuc}(\boldsymbol{r})$ and $V^{A'}_{\rm nuc}(\boldsymbol{r})$ are the one-electron potentials arising from the different nuclear charge distributions of the two isotopes A and A', and $\rho^e_{\Gamma J}(\boldsymbol{r})$ is the level electron density distribution inside the nuclear volume of the reference isotope A (averaged over the magnetic components M). The electron density is evaluated as

$$\rho^e_{\Gamma J}(\boldsymbol{r}) = \langle \Gamma PJ||\sum_{i=1}^{N}\delta(\boldsymbol{r}-\boldsymbol{r}_i)||\Gamma PJ\rangle. \tag{2.74}$$

Assuming a spherically symmetric nuclear charge distribution, the electron density within the nucleus can be expanded as an even polynomial function [47, 48,

49]. After keeping only the first few terms, the electron density around $r = 0$ is given by

$$\rho^e_{\Gamma J}(\boldsymbol{r}) \approx b_{\Gamma J}(r) = b_{\Gamma J,1} + b_{\Gamma J,2} r^2 + b_{\Gamma J,3} r^4 + b_{\Gamma J,4} r^6. \tag{2.75}$$

Inserting the expansion above in Eq. (2.73), we arrive at the expression for the reformulated (level) field shift (RFS) [49, 2], which is written as

$$\delta E^{(1)A,A'}_{\Gamma J,\mathrm{FS}} \approx \delta E^{(1)A,A'}_{\Gamma J,\mathrm{RFS}} = \sum_{n=1}^{4} F_{\Gamma J,n} \delta \langle r^{2n} \rangle^{A,A'}, \tag{2.76}$$

where $F_{\Gamma J,n}$ are the level electronic factors given by

$$F_{\Gamma J,n} = \frac{2\pi Z b_{\Gamma J,n}}{n(2n+1)}, \tag{2.77}$$

and

$$\delta \langle r^{2n} \rangle^{A,A'} = \langle r^{2n} \rangle^{A} - \langle r^{2n} \rangle^{A'} \tag{2.78}$$

are the differences in radial nuclear moments, of order $2n$, between the isotopes A and A'. These moments can be taken from any model, calculation, or experiment.

The computations of the MS parameters $K_{\Gamma J,\mathrm{NMS}}$, $K_{\Gamma J,\mathrm{SMS}}$ and electronic factors $F_{\Gamma J,n}$ are performed using the program RIS4 [2], which is compatible with the GRASP code. In RIS4, the polynomial expansion $b_{\Gamma J}(r)$ is, for each level, fitted to the constructed electron density $\rho^e_{\Gamma J}(\boldsymbol{r})$ using a least-squares method.

Accounting for the level IS of the upper u and lower l states participating in a transition k, as displayed in Figure 2.3, yields the line IS, i.e.,

$$\begin{aligned} \Delta E^{A,A'}_{k,\mathrm{IS}} &= \Delta E^{A,A'}_{k,\mathrm{MS}} + \Delta E^{A,A'}_{k,\mathrm{FS}} \\ &= \left(\Delta K_{k,\mathrm{NMS}} + \Delta K_{k,\mathrm{SMS}}\right) \frac{M^{A'} - M^{A}}{M^{A} M^{A'}} \\ &\quad + \sum_{n=1}^{4} \frac{2\pi Z \Delta b_{k,n}}{n(2n+1)} \, \delta \langle r^{2n} \rangle^{A,A'}, \end{aligned} \tag{2.79}$$

where $\Delta K_{k,\mathrm{NMS}}, \Delta K_{k,\mathrm{SMS}}$ and $\Delta b_{k,n}$ are, respectively, the differences of the MS parameters $K_{\Gamma J,\mathrm{NMS}}$, $K_{\Gamma J,\mathrm{SMS}}$ and the coefficients $b_{\Gamma J,n}$ between the upper state u and lower state l. The experimentally measurable line frequency IS is, then, given by

$$\delta \nu^{A,A'}_{k,\mathrm{IS}} = \frac{\Delta E^{A,A'}_{k,\mathrm{IS}}}{h}. \tag{2.80}$$

2.5 General Computational Methodology

The accuracy of multiconfiguration calculations relies on the expansions of the ASFs given by Eq. (2.39). The latter need to be truncated, and the included CSFs must effectively capture *electron correlation* [35]. To generate lists of CSFs that systematically account for the *electron correlation* effects and build accurate wave functions, multiconfiguration calculations often follow a well-defined optimization scheme, known as the SD-MR approach [50, 27]. In this section, we describe the general methodology of atomic structure calculations following this approach. The details, which depend on the shell structure of the atom at hand, the number of targeted states, and the available computational resources, will be discussed in the next chapter within the context of astrophysical applications.

When applying the SD-MR approach, the starting point is to define a multireference (MR). The MR is a set of configurations that are associated with the targeted atomic states, merged with important closely degenerate configurations [27]. Applying rules for the coupling of angular momenta, the configurations in the MR produce a set of CSFs that acccount for the major *correlation* effects. These effects describe what is known as the *static correlation*, or else, the long-range re-arrangement of the electron charge distribution. By performing an MCDHF calculation for the orbitals of the MR configurations, a first approximation of the wave functions of the targeted states is acquired. The orbitals that take part in this initial calculation are called *spectroscopic* and are required to have the node structure of hydrogenic orbitals, which is determined by the principal quantum number, as discussed in Subsection 2.2.1. The *spectroscopic* orbitals are kept frozen in all subsequent MCDHF calculations.

The initial approximation of the wave functions is improved by also accounting for the *dynamic correlation* effects, which are related to the *cusp condition*[3] [51]. To do so, the atomic state expansions are gradually enlarged with CSFs that interact with the ones that are formed from the MR configurations. Such CSFs are built from configurations that differ by either a single (S) or a double (D) electron substitution from the configurations in the MR. Following the SD-MR approach, the interacting configurations are obtained by allowing SD substitutions of electrons from the *spectroscopic* orbitals to an active set (AS) of *correlation* orbitals. The AS is systematically increased to introduce at each step an additional *correlation* orbital layer [52, 53], for which an MCDHF calculation is performed.

[3] The *cusp condition* arises form the singularity of the inter-electronic Coulomb interaction $1/r_{ij}$ near points of coalescence where $r_{ij} = 0$.

The interacting configurations produce CSFs that can be classified, based on the nature of the SD substitutions, into CSFs that capture valence–valence (VV), core–valence (CV), and core–core (CC) *electron correlation* effects [50, 27]. The radial orbital basis is obtained by performing MCDHF calculations, where all, or some, of the classes of CSFs are taken into account. After the orbital basis is generated, additional *electron correlation* effects, even beyond the SD-MR model, can be considered in the final RCI calculations.

Building accurate wave functions requires a considerable amount of CSFs that would generate a very large orbital basis. Even so, a large but incomplete orbital basis does not ensure that the wave functions give accurate properties other than energies. In the MCDHF calculations, the *correlation* orbitals are obtained by applying the *variational principle* on the weighted energy functional of all the targeted atomic states. Thus, the orbitals of the first *correlation* layers will overlap with the *spectroscopic* orbitals that account for the effects that minimize the energy the most [54, 55]. The energetically dominant effects must first be saturated to obtain orbitals localized in other regions of space, which might describe effects that do not lower the energy much, but are important for, e.g., transition parameters. This implies that the orbital basis must carefully be constructed with respect to the computed properties [56].

Chapter 3

Atomic Data for Astrophysics

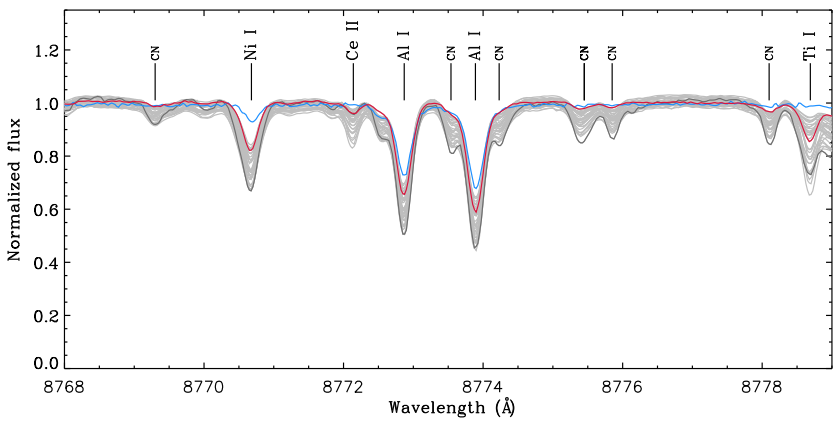

Figure 3.1: Sample of spectra in the optical region that are used for abundance analysis[a b]. The blue spectrum represents the Sun, the red and dark gray spectra are the standard benchmark giants arcturus and muLeo[c], while the lighter gray spectra represent about 50 other giants. (Image credits: [57].)

[a] `http://www.astro.lu.se/~henrikj/posters.shtml`
[b] `http://www.cfht.hawaii.edu/Instruments/Spectroscopy/Espadons/`
[c] `https://www.blancocuaresma.com/s/benchmarkstars`

Over the past couple of decades, technology has been progressing rapidly, and the high-resolution instruments that are now used in astronomical spectroscopy have raised the demands on atomic data. Moreover, the new generation of telescopes are designed for the infrared (IR) spectral region [58, 59, 60], and reference data from the higher part of the spectrum must also be made avail-

able. That being so, interpreting astronomical spectra requires nearly complete datasets of atomic parameters for the systems of interest. In Paper I, extensive data of parameters, such as energies, *transition rates*, and *radiative lifetimes*, have been produced for the systems of Al II and Al I. Spectral lines of these ions have been observed in the solar spectrum and in many stellar spectra (see for instance Figure 3.1), and such data are of great astrophysical interest.

Performing extended spectrum calculations, where numerous atomic states are targeted at the same time, is generally not trivial. To build accurate wave functions for all states, special attention to the optimization scheme of the orbital basis must be paid. In what follows, we briefly discuss the targeted spectra in the computations of Al II and Al I and describe, for each system, the applied strategies for obtaining the orbital basis. The most significant results and conclusions, which emphasize the computational challenges in these two systems, are then summarized. Finally, we suggest modifications in the optimization strategies that could improve the accuracy of the computed atomic data.

3.1 Al II and Al I: The Targeted Spectra

Table 3.1: Configurations of the targeted states in the computations of Al II and Al I. For brevity, the [Ne] neon core, where [Ne]=$1s^2 2s^2 2p^6$, is omitted.

	Al II	Al I
Even	$3s^2$	$3s^2\{4s,5s,6s\}$
	$3p^2$	$3s3p^2$
	$3s\{4s,5s,6s,7s\}$	$3s^2\{3d,4d,5d,6d\}$
	$3s\{3d,4d,5d,6d\}$	$3s^25g$
	$3s\{5g,6g\}$	
Odd	$3s\{3p,4p,5p,6p,7p\}$	$3s^2\{3p,4p,5p,6p\}$
	$3s\{4f,5f,6f\}$	$3s^2\{4f,5f\}$
	3p3d	
	3s6h	

The spectrum calculations that were carried out in Paper I targeted 78 and 28 states, in singly ionized and neutral aluminium, respectively. The configurations of the targeted states are shown, for both systems, in Table 3.1. The brackets that appear in Table 3.1 successively include the orbitals of the configuration states that are part of *Rydberg series*, i.e., configuration states that are formed by exciting the outermost electron to orbitals of increasing n quantum number,

but the same l symmetry. Atomic structure calculations of systems that involve *Rydberg series* are often associated with additional difficulties.

Due to perturbers that enter the *Rydberg series*, some states are strongly mixed. In Al II, the lower part of the spectrum is dominated by the strong interaction between the 3s3d ^{1}D and 3p^2 ^{1}D configuration states. This can readily be deduced by looking at the LS-composition of these states as, for instance, given in the NIST database [61]. Moving higher, the spectrum of Al II is governed by the strong configuration mixing of the 3snf ^{3}F series with the 3p3d ^{3}F states. As Al I has an additional electron in the valence shell, in this system the strong two-electron interaction between the 3s3d ^{1}D and 3p^2 ^{1}D states manifests itself in the interaction between the 3s^{2}3d ^{2}D and 3s3p^2 ^{2}D states. In fact, the 3s3p^2 ^{2}D perturber state is smeared out over the entire discrete part of the 3s^{2}nd ^{2}D *Rydberg series*, resulting in the strong mixing of all these states [62]. The positions of strongly mixed states are predicted correctly only if the wave functions are highly correlated, which in turn requires to consider large CSF expansions.

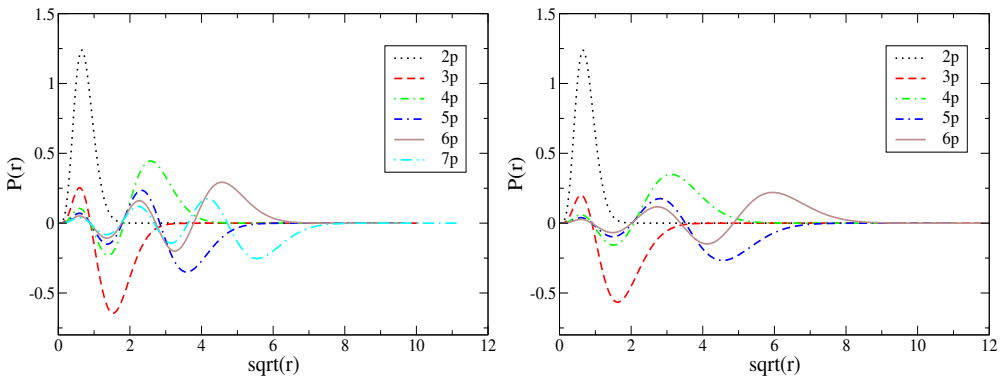

Figure 3.2: Al II (left) and Al I (right) Dirac-Fock radial orbitals for the p symmetry, as a function of $\sqrt{r}$. The 2p orbital is part of the core shell and the orbitals with $n > 2$ belong to the valence shell, occupying different regions in space.

In the targeted spectra, some of the *Rydberg series* include the 3snp ^{1,3}P states in Al II and the 3s^{2}np ^{2}P states in Al I. These states encompass valence orbitals np that extend from $n = 3$ to 7 and $n = 3$ to 6, respectively (see also Table 3.1). In Figure 3.2, the Dirac-Fock radial orbitals np are shown as a function of $\sqrt{r}$. As seen in the figure, the valence orbitals occupy different regions in space, extending far out from the atomic core. Same conclusions are drawn for *Rydberg* orbitals that belong to other angular symmetries. Since the overlap between orbitals that make up *Rydberg* states is in some cases minor, finding an optimal

orbital basis is not straightforward. The CSF expansions must be generated so that the *correlation* orbitals are properly localized to adequately describe the wave functions of all targeted states.

3.2 Computations

3.2.1 Al II

Applying the developed methodology, described in Section 2.5, in the computations of Al II, it is possible to build the radial orbital basis using CSF expansions that are produced by single and restricted double (SrD)-MR electron substitutions (the MR consists of the targeted configurations shown in Table 3.1), from the valence orbitals and the $2p^6$ core, with the restriction that only one substitution is allowed from $2p^6$. In this manner, the CSFs would capture both VV and CV *electron correlation* effects. The 2pnl pair-correlation effect is relatively important. From initial MCDHF calculations and analysis of the mean radii of the resulting orbitals, we observed that the orbitals of the first *correlation* layers were spatially localized between the 2p core orbital and the inner valence orbitals. As a result, the wave functions were not properly described for all states, and in particular, not for the higher *Rydberg* states considered.

A correct representation of all targeted states demands that the *correlation* orbitals occupy, instead, the space of the valence orbitals. Hence, the atomic state expansions ultimately included CSFs that were formed by only allowing VV substitutions of electrons to effectively build six layers of *correlation* orbitals. The resulting *correlation* orbitals were, in this latter case, more extended, overlapping with orbitals of higher *Rydberg* states. In the subsequent RCI calculations, the CSF expansions were augmented by enabling SrD-MR electron substitutions from the valence orbitals and the 2s and 2p core orbitals, with the restriction that there is maximum one substitution from the $n = 2$ core orbitals.

3.2.2 Al I

The system of Al I is more complex than Al II, and the MCDHF calculations for constructing the orbital basis were more involved. *Static electron correlation* was accounted for by extending the MR to include, besides the targeted configurations shown in Table 3.1, configurations of CSFs that give considerable contributions to the total wave functions, i.e., CSFs with mixing coefficients $\gtrsim 0.05$. The MR that was used in the computations of Al I is presented in Table 3.2.

Table 3.2: Extended multireference in the computations of Al I.

	Al I
Even	$3s^2\{4s,5s,6s\}$
	$3p^2\{4s,5s,6s\}$
	$3s3p^2$
	$3s^2\{3d,4d,5d,6d\}$
	$3p^2\{3d,4d,5d,6d\}$
	$3s^25g$
	$3p^25g$
Odd	$3s^2\{3p,4p,5p,6p\}$
	$3p^3$
	$3p^2\{4p,5p,6p\}$
	$3s^2\{4f,5f\}$
	$3p^2\{4f,5f\}$

To account for *dynamic correlation*, the atomic state expansions were enlarged with CSFs that were formed by allowing SrD electron substitutions from the valence *spectroscopic* orbitals to six layers of *correlation* orbitals. The applied restriction was that there was at most one substitution from orbitals with $n = 3$. By doing so, the *correlation* orbitals were properly localized, between the inner $n = 3$ valence orbitals and the outer orbitals of the higher *Rydberg* states, to ably describe all states considered. Subsequent RCI calculations included CSF expansions produced by SDT substitutions from all valence orbitals and SD substitutions from the valence orbitals and the $2p^6$ core, with the limitation of allowing maximum one hole in $2p^6$.

3.3 Results

The spectrum calculations that were performed in Paper I produced a great number of updated *ab initio* excitation energies and transition data. An important task is to evaluate the accuracy of these data. The computed excitation energies are compared with the critically evaluated energies proposed by NIST [61] and are found to be in very good agreement. On average, the relative differences between computed energies E_{RCI} and critically compiled energies E_{NIST} are $< 0.2\%$ and $< 0.6\%$, in Al II and Al I, respectively. In the computations of Al II, all differences $\Delta E = E_{\mathrm{NIST}} - E_{\mathrm{RCI}}$ maintain the same sign, and similar is the case for Al I, with the exceptions of the $3s^24d\ {}^2D_{3/2,5/2\ a}{}^1$ states. That

[1] The subscript a is used to distinguish the two terms that are assigned the same label after the computations.

being so, the uncertainties in the predicted excitation energies of two states associated with a transition most often cancel out, and the majority of the derived transition energies are in excellent agreement with the NIST values.

The uncertainties of the computed transition data essentially arise from the disagreement of the reduced matrix elements (2.61) and (2.62), respectively, evaluated in the *length* and *velocity* form. These uncertainties are reflected in the dT values given by Eq. (2.65). For the strong transitions, i.e., transitions with *rates* $A > 10^6$ s^{-1}, the A values are subject to uncertainties dT that are typically of the order of 3% in Al II and 5% in Al I. It is, however, observed that when the transitions involve high *Rydberg* states, the agreement between the A_l and A_v values is not as good. For instance, when the $3s^2 6s\ ^2S_{1/2}$ state participates in a transition in Al I, the average uncertainty dT is about 8%. In Al II, for transitions involving the 3s7p ^{1,3}P states, the dT values are consistently large, ranging between 8% and 37%. Consequently, the *lifetimes* of the 3s7p ^{1,3}P states are computed with average uncertainties of the order of 13%. The latter uncertainties are by far the largest among all computed *lifetimes* in Al II.

3.4 Conclusions

The computations of reduced matrix elements in the *length* and the *velocity* form, respectively, involve the *transition integrals* (2.63) and (2.64), which probe separate parts of the wave functions. Obtaining transition data that are weakly sensitive to the choice of gauge (form), i.e., $dT \sim 0$, requires that the radial parts of the wave functions are well approximated as a whole. In the computations of Al II and Al I, despite the specific optimization strategies, the *correlation* orbitals are, in most cases, rather contracted compared to the *spectroscopic* outer *Rydberg* orbitals, and the outer part of the wave functions representing the high *Rydberg* states is not always effectively described. As a result, computed data for transitions involving high *Rydberg* states are often subject to unexpectedly large dT values.

To improve the overall accuracy of the computed transition data, a more balanced radial orbital basis, containing orbitals that occupy regions of space far from the atomic core, should be generated. To do so, one could consider including in the MR configurations that encompass orbitals of higher principal quantum numbers, i.e., 3snl configurations with $n = 8, 9$ in Al II and $3s^2$nl configurations with $n = 7, 8$ in Al I. The same optimization strategy has been applied in the past in spectrum calculations of Mg I [42].

Chapter 4

Probing Nuclear Properties in Heavy Atoms

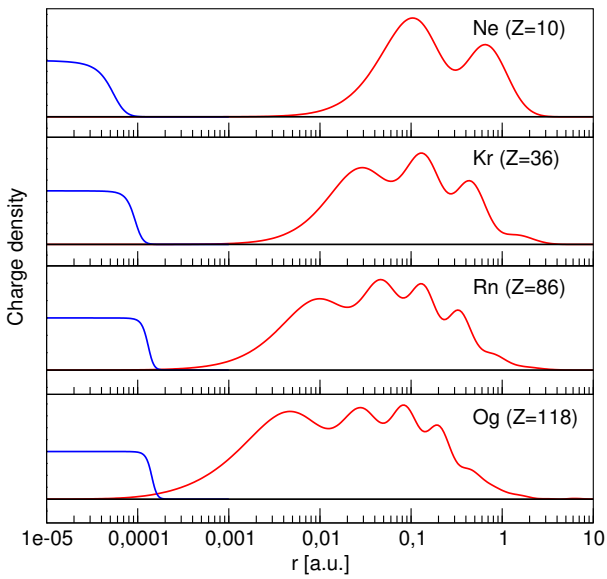

Figure 4.1: Nuclear charge (blue) and radial electron (red) density distributions in ground states of selected nobel gases. The nuclear charge and extent, together with the contraction of the atomic orbitals, increase with the atomic number Z, and the contribution from the FS to the observed IS is significantly larger in heavier atomic systems. (Image credits: [63].)

In light atoms, the electron density within the nucleus is essentially constant, and, after keeping only the first term in Eq. (2.76), the FS contribution to the IS is assumed to be proportional to the changes in $\langle r^2 \rangle$ nuclear moments. On the contrary, in heavier systems, the electron density inside the nuclear volume varies. For an accurate description of the FS, terms involving changes in higher-order radial moments must, thus, be considered. The radial moments are normally calculated using models that approximate the nuclear charge density distributions. In atomic structure calculations, the most commonly adopted approximation is the Fermi model given by (2.72), which, nonetheless, does not fully capture the details of the nuclear charge distributions.

In Paper II, the effect from using realistic nuclear charge distributions, obtained from microscopic nuclear models, on the computed FS was quantitatively investigated. It was deduced that, in relatively heavy nuclear systems, the latter effect can be significant and above the observable limit. This suggests the possibility to extract information about higher-order radial moments from IS measurements. The developed method for extraction of higher than second-order radial moments is presented, and the systematical and statistical errors that need to be considered are briefly discussed.

4.1 Realistic Nuclear Charge Distributions

In Section III.B of Paper II, calculated FS values in Ba I ($Z = 56$) are compared with experimental IS data [64], from which the theoretical MS contributions were subtracted [65]. To calculate the FS given by Eq. (2.76), we used nuclear radial moments that resulted from: (i) the Fermi model and (ii) the realistic nuclear charge distributions obtained from DFT calculations [5]. The comparison shows that the calculations based on the Fermi distribution fail to capture the general behavior of the observed FS. On the other hand, the microscopic nuclear calculations capture both the right trend with neutron number and, in addition, some of the odd-even staggering (see also Figure 3 in the paper).

The Fermi model was used with the rms radii given by

$$\sqrt{\langle r^2 \rangle} = 0.836 \cdot A^{\frac{1}{3}} + 0.570 \text{ fm } (A > 9), \tag{4.1}$$

where A denotes the mass number of the isotope. The major correction to the descriptions of the observed FS values is clearly provided by the use of realistic rms radii. However, by also making use of realistic higher-order radial moments, the predicted FS are further improved. In Figure 4.2, the Fermi and realistic nuclear charge distributions are, for instance, compared for the system

of neodymium (Z=60). The Fermi distribution, shown in the figure, is tuned so that is has the same $\langle r^2 \rangle$ radial moment as the more realistic charge distribution denoted as "DFT". Nonetheless, the density profiles differ to some extent. The Fermi model, with fixed skin thickness $t = 2.3$ fm, does not properly describe the density wiggles and diffuseness of the distribution. These features are encoded in higher-order radial moments.

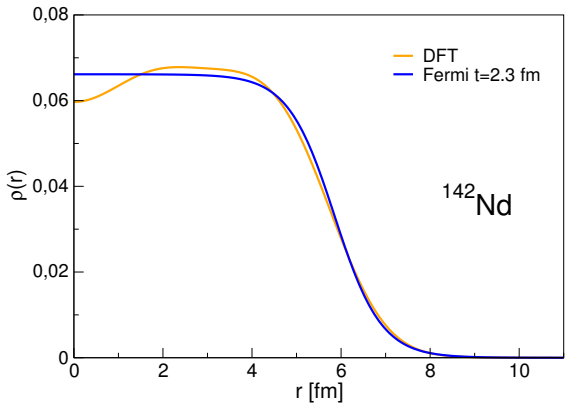

Figure 4.2: Comparison between the nuclear charge density distributions resulting from the Fermi model (blue) and the DFT calculations (orange) in the spherical neodymium (Nd) with mass number $A = 142$. The Fermi model has a fixed skin thickness $t = 2.3$ fm and is fitted to reproduce the $\langle r^2 \rangle$ moment provided by the realistic DFT calculations. Discrepancies in the specifics of the distributions are observed. (Image credits: [63].)

In Section IV, we further investigate the magnitude of the corrections when realistic higher-order radial moments are used, in Eq. (2.76), to predict the FS. This was done by evaluating the so-called *correction term*, which is defined as

$$\delta\nu^{A,A'}_{\text{realistic}} - \delta\nu^{A,A'}_{\text{Fermi}} = \sum_{n=2}^{4} F_{k,n}[\,\delta\left\langle r^{2n}\right\rangle^{A,A'}_{\text{realistic}} - \delta\left\langle r^{2n}\right\rangle^{A,A'}_{\text{Fermi}}\,]. \tag{4.2}$$

The magnitude of (4.2) was estimated for a wide range of isotopes in Li-like systems and Ba I. For isotope pairs A, A' of a specific element, the absolute value of (4.2) typically grows with the difference between the neutron number $\Delta N^{A,A'}$. When more neutrons are added (or removed), they alter the protons' distribution, leading to changes in the diffuseness. As also seen in Figure 4.2, this effect is not sufficiently captured by the Fermi model. In deformed nuclei, the corrections further depend on the quadrupole deformation parameter β_{20},

which is assumed to be zero in the Fermi model given by (2.72). The corrections increase when the difference in deformation between the reference and the target isotope gets larger. The same trends are observed in Ba I. When, instead, the axially symmetric deformed Fermi model, which is given by Eq. (11) in Paper II, is used, the *correction term* appears to be smaller.

Besides the IS measurements in Ba I, experimental IS are also available for the first two resonance transitions in the $^{142,150}\mathrm{Nd}^{57+}$ isotope pair [66]. In highly-charged systems, the MS contribution is generally much smaller, and the uncertainties in the observed FS values are most often restricted to the experimental uncertainties. That being so, the uncertainties of the observed IS in $^{142,150}\mathrm{Nd}^{57+}$ are compared with the estimated *correction terms* resulting from the use of realistic higher than second-order radial moments (see Figure 6 in Paper II). It is deduced that effects, such as deformation, which are captured by these nuclear radial moments, could be detected. In the next two sections, the developed method for possible simultaneous extraction of the $\delta\left\langle r^2\right\rangle$ and $\delta\left\langle r^4\right\rangle$ radial moment differences from IS measurements is outlined.

4.2 Simultaneous Extraction of $\delta\left\langle r^2\right\rangle$ and $\delta\left\langle r^4\right\rangle$

The RFS expression given by Eq. (2.76), combined with experimental IS data, in principle, enables the extraction of differences in higher-order radial moments. Given measurements for at least four transitions k, a system of four equations can be solved, i.e.,

$$\delta\nu_{k,\mathrm{RFS}} = F_{k,1}\delta\left\langle r^2\right\rangle + F_{k,2}\delta\left\langle r^4\right\rangle + F_{k,3}\delta\left\langle r^6\right\rangle + F_{k,4}\delta\left\langle r^8\right\rangle, \tag{4.3}$$

where $k = 1, 2, 3, 4$. However, it is rare that observed IS are available for four transitions, and such systems of equations cannot be formed so that they give trustworthy solutions for higher than second-order moments.

The expansion (4.3) is truncated, and the set of r^{2n}, where $n = 1, 2, 3, 4$, does not form an orthonormal basis. By instead expanding in a set of orthogonal polynomials y_n, the RFS expression is written as

$$\delta\nu_{k,\mathrm{RFS}} = c_{k,1}\delta\left\langle y_1\right\rangle + c_{k,2}\delta\left\langle y_2\right\rangle + c_{k,3}\delta\left\langle y_3\right\rangle + c_{k,4}\delta\left\langle y_4\right\rangle, \tag{4.4}$$

where the new expansion coefficients $c_{k,n}$ are expressed in relation to the electronic factors $F_{k,n}$ and the functions y_n are given in terms of the r^{2n} moments (see Appendix in Paper II). The expansion (4.4) converges substantially faster

than the original summation (4.3). In fact, simply the $\delta\langle y_1\rangle$ and $\delta\langle y_2\rangle$, which are given in terms of the $\delta\langle r^2\rangle$ and $\delta\langle r^4\rangle$, need to be considered when the sum is rearranged. Then, for a pair of isotopes A, A' and a transition k, the RFS can, to a very good approximation, be expressed as

$$\delta\nu_{k,\mathrm{RFS}} \approx c_{k,1}\delta\langle y_1\rangle + c_{k,2}\delta\langle y_2\rangle\,. \tag{4.5}$$

From knowledge of observed IS for at least two transitions, a system of two equations is then solved for the unknowns $\delta\langle y_1\rangle$ and $\delta\langle y_2\rangle$, from which the $\delta\langle r^2\rangle$ and $\delta\langle r^4\rangle$ values are determined. It is demonstrated in the paper that the expression (4.5) enables the determination of the differences in the $\langle r^2\rangle$ and $\langle r^4\rangle$ moments much more accurately than when the first two terms of the original expression (4.3) are considered. Yet, there are still systematical and statistical errors that must be taken into account, and their nature will be discussed next.

4.3 Errors in the Extraction of $\delta\langle r^2\rangle$ and $\delta\langle r^4\rangle$

4.3.1 Systematical errors

From observed IS, experimental FS values can be obtained by estimating and subtracting the MS contribution and residual effects, $\delta\nu_{k,\mathrm{RES}}$, so that

$$\delta\nu^{\mathrm{expt}}_{k,\mathrm{FS}} = \delta\nu^{\mathrm{expt}}_{k,\mathrm{IS}} - \delta\nu_{k,\mathrm{MS}} - \delta\nu_{k,\mathrm{RES}}. \tag{4.6}$$

The residual effects are related to QED effects, or, the model errors induced by the perturbation treatment that led to the RFS expression. They can be represented by the discrepancy between the "exact" variational solution $\delta\nu^{\mathrm{exact}}_{k,\mathrm{VA}}$ (see Subsection 2.4.2) and the RFS solution $\delta\nu_{k,\mathrm{RFS}}$. Making a "qualified guess" for the unknown rms radii of the target and, perhaps, the reference isotope, and assuming a two-parameter Fermi distribution that yields the higher-order moments for both isotopes, this discrepancy can be evaluated. A "qualified guess" of rms radii is provided by, e.g., the parametrization of Eq. (4.1). In heavy nuclei, the QED effects become significant and it is, therefore, crucial to precisely determine the $\delta\nu_{k,\mathrm{RES}}$ term in these systems. In Section V.B of Paper II, the contributions from QED effects were, indicatively, investigated for two different isotope pairs in uranium (Z=92), and they were found to be of the order of 1.5%.

4.3.2 Statistical errors

The $\delta\langle r^2\rangle$ and $\delta\langle r^4\rangle$ moments are determined based on the $\delta\langle y_1\rangle$ and $\delta\langle y_2\rangle$ values, which are extracted by solving the matrix equation

$$\begin{bmatrix} \delta\nu_{1,\mathrm{RFS}} \\ \delta\nu_{2,\mathrm{RFS}} \end{bmatrix} = C \begin{bmatrix} \delta\langle y_1\rangle \\ \delta\langle y_2\rangle \end{bmatrix}. \tag{4.7}$$

where

$$C = \begin{bmatrix} c_{1,1} & c_{1,2} \\ c_{2,1} & c_{2,2} \end{bmatrix} \tag{4.8}$$

is the matrix containing the expansion coefficients of the equations that are formed based on (4.5). The unknown $\delta\langle y_1\rangle$ and $\delta\langle y_2\rangle$ are, thus, evaluated according to

$$\begin{bmatrix} \delta\langle y_1\rangle \\ \delta\langle y_2\rangle \end{bmatrix} = C^{-1} \begin{bmatrix} \delta\nu_{1,\mathrm{RFS}} \\ \delta\nu_{2,\mathrm{RFS}} \end{bmatrix}. \tag{4.9}$$

To obtain $\delta\langle y_1\rangle$ and $\delta\langle y_2\rangle$, the matrix C must be invertible. If the matrix determinant is zero, then the matrix is singular and cannot be inverted. Occasionally, the determinant of the matrix can approach zero, but still be nonzero. In this case, the matrix is close to singular and the extracted $\delta\langle y_1\rangle$ and $\delta\langle y_2\rangle$ will be hugely affected, even by a small change in the field shifts $\delta\nu_{1,\mathrm{RFS}}$ and $\delta\nu_{2,\mathrm{RFS}}$. This means that the values of $\delta\langle y_1\rangle$ and $\delta\langle y_2\rangle$ and, in turn, the $\delta\langle r^2\rangle$ and $\delta\langle r^4\rangle$ moments, might be greatly affected by the uncertainties in the observed IS, the computed MS, and the evaluated residual effects of Eq. (4.6).

A matrix determinant equal to zero is obtained if the two equations are linearly dependent. To minimize the statistical errors when solving Eq. (4.9), the set of electronic factors $F_{k,n}$, which affect the values of the coefficients $c_{k,n}$, for the two transitions must be as linearly independent as possible.

Chapter 5

Outlook

Paper I made available a substantial amount of updated *ab initio* atomic data in Al II and Al I. For the most part, the produced transition data meet the high demands in accuracy. Nonetheless, transition parameters associated with highly excited states are often computed with rather significant uncertainties. The systems of Al II and Al I involve states that are part of *Rydberg series*, and the studies of such systems are generally not trivial. The challenges in the computations of *Rydberg series* become apparent mostly when computing transition parameters. As the major objective in spectrum calculations is to produce transition data that are weakly sensitive to the choice of gauge for all the computed transitions, different computational strategies, for optimizing the orbital basis used to construct the wave functions, are continuously explored. Due to the recent astronomical interest in the IR part of the spectrum, this is of particular interest and subject for future research.

In Paper II, a promising method for the extraction of both $\delta\langle r^2\rangle$ and $\delta\langle r^4\rangle$ radial moment differences is presented and tested. Considering both systematical and statistical errors for isotope pairs in different elements, it is deduced that an increase in experimental precision by 1-2 orders of magnitude, or/and access to data for more independent transitions is essential. From the theoretical side, effort to accurately compute the MS contributions, mainly in neutral and near-neutral systems, must be made. Combined progress in theory and experiment would allow possible tabulation of changes in the $\langle r^4\rangle$ nuclear moments. It has recently been shown that the $\langle r^4\rangle$ moment is directly related to the surface thickness of the nuclear charge density distribution, and thus, prediction of $\langle r^4\rangle$ values will allow realistic estimates of nuclear structure corrections for the interpretation of new physics quests [67].

References

[1] Froese Fischer C., Gaigalas G., Jönsson P., and Bieroń J. GRASP2018-A Fortran 95 version of the General Relativistic Atomic Structure Package. *Comput. Phys. Commun.*, 237:184–187, 2019.

[2] Ekman J., Jönsson P., Godefroid M., Nazé C., Gaigalas G., and Bieroń J. RIS 4: A program for relativistic isotope shift calculations. *Comput. Phys. Commun.*, 235:433–446, 2019.

[3] Papoulia A. The effect of realistic nuclear charge distributions on atomic levels and transitions. Master's thesis, Lund University, 2015.

[4] Carlsson B. G., Dobaczewski J., Toivanen J., and Veselý P. Solution of self-consistent equations for the N^3LO nuclear energy density functional in spherical symmetry. The program HOSPHE (v1.02). *Comput. Phys. Commun.*, 181:1641–1657, 2010.

[5] Stoitsov M. V., Schunck N., Kortelainen M., Michel N., Nam H., Olsen E., Sarich J., and Wild S. Axially deformed solution of the Skyrme-Hartree-Fock-Bogoliubov equations using the transformed harmonic oscillator basis (II) HFBTHO v2.00d: A new version of the program. *Comput. Phys. Commun.*, 184:1592–1604, 2013.

[6] Jönsson P., Gaigalas G., Bieroń J., Froese Fischer C., and Grant I. P. New version: GRASP2K relativistic atomic structure package. *Comput. Phys. Commun.*, 84:2197–2203, 2013.

[7] Gilore G. and Wyse R. The chemical evolution of the galaxy. *Nature*, 322:806–807, 1986.

[8] Jabran Z., Geller M., Kewley L., Hwang H. S., Fabricant D., and Kurtz M. The chemical evolution of star-forming galaxies over the last 11 billion years. *Astrophys. J.*, 771(2):L19, 2013.

[9] Gerner T., Beuther H., Semenov D., Linz H., Vasyunina T., Bihr S., Shirley Y. L., and Henning Th. Chemical evolution in the early phases of massive star formation. I. *A&A*, 563:A97, 2014.

[10] Wang K., Song C. X., Jönsson P., Del Zanna G., Schiffmann S., Godefroid M., Gaigalas G., Zhao X. H., Si R., Chen C. Y., and Yan J. Benchmarking atomic data from large-scale multiconfiguration Dirac–Hartree–Fock calculations for astrophysics: S-like ions from Cr ix to Cu xiv. *Astrophys. J. Suppl. S.*, 239(2):30, 2018.

[11] Hawkins I. and Jura M. The C-12/C-13 isotope ratio of the interstellar medium in the neighborhood of the Sun. *Astrophys. J.*, 317:926–950, 1987.

[12] Federman S. R., Lambert D.L., Cardelli J.A., and Sheffer Y. The boron isotope ratio in the interstellar medium. *Nature*, 381(6585):764–766, 1996.

[13] Proffitt C. R., Jönsson P., Litzén U., Pickering J. C., and Wahlgren G. M. Goddard high-resolution spectrograph observations of the B III resonance doublet in early B stars: abundances and isotope ratios. *Astrophys. J.*, 516:342–348, 1999.

[14] Kurucz R. L. Atomic data for interpreting stellar spectra: isotopic and hyperfine data. *Physica Scripta*, T47:110, 1993.

[15] Nazé C., Gaidamauskas E., Gaigalas G., Godefroid M., and Jönsson P. RIS3: A program for relativistic isotope shift calculations. *Comput. Phys. Commun.*, 184:2187–2196, 2013.

[16] Parthey C. G., Matveev A., Alnis J., Bernhardt B., Beyer A., Holzwarth R., Maistrou A., Pohl R., Predehl K., Udem T., et al. Improved measurement of the hydrogen $1S-2S$ transition frequency. *Phys. Rev. Lett.*, 107:203001, 2011.

[17] Mané E., Voss A., Behr J. A., Billowes J., Brunner T., Buchinger F., Crawford J. E., Dilling J., Ettenauer S., Levy C. D. P., et al. First experimental determination of the charge radius of ^{74}Rb and its application in tests of the unitarity of the Cabibbo-Kobayashi-Maskawa matrix. *Phys. Rev. Lett.*, 107:212502, 2011.

[18] Yordanov D. T., Bissell M. L., Blaum K., De Rydt M., Geppert Ch., Kowalska M., Krämer J., Kreim K., Krieger A., Lievens P., et al. Nuclear charge radii of $^{21-32}$Mg. *Phys. Rev. Lett.*, 108:042504, 2012.

[19] Angeli I. and Marinova K.P. Table of experimental nuclear ground state charge radii: An update. *Atomic Data and Nuclear Data Tables*, 99:69–95, 2013.

[20] Berengut J. C., Budker D., Delaunay C., Flambaum V. V., Frugiuele C., Fuchs E., Grojean C., Harnik R., Ozeri R., Perez G., et al. Probing new long-range interactions by isotope shift spectroscopy. *Phys. Rev. Lett.*, 120:091801, 2018.

[21] Stadnik Yevgeny V. Probing long-range neutrino-mediated forces with atomic and nuclear spectroscopy. *Phys. Rev. Lett.*, 120:223202, 2018.

[22] De Vries H., De Jager C. W., and De Vries C. Nuclear charge-density-distribution parameters from elastic electron scattering. *At. Data Nucl. Data Tables*, 36:495–536, 1987.

[23] Anni R., Co G., and Pellegrino P. Nuclear charge density distributions from elastic electron scattering data. *Nucl. Phys. A*, 584:35–39, 1995.

[24] Grant I. P. *Relativistic quantum theory of atoms and molecules. Theory and computation. Atomic, Optical and Plasma Physics.* Springer, New York, USA, 2007.

[25] Johnson W. R. *Atomic structure theory: Lectures on atomic physics.* Springer Verlag, Berlin, Heidelberg, Springer-Verlag edition, 2007.

[26] Dyall K. G., Grant I. P., Johnson C. T., Parpia F. A., and Plummer E. P. Grasp: A general-purpose relativistic atomic structure program. *Comput. Phys. Commun.*, 55(3):425–456, 1989.

[27] Froese Fischer C., Godefroid M., Brage T., Jönsson P., and Gaigalas G. Advanced muliconfiguration methods for complex atoms: I. energies and wave functions. *J. Phys. B: At. Mol. Opt. Phys.*, 49(18):182004, 2016.

[28] Parpia F. A. and Mohanty A. K. Relativistic basis-set calculations for atoms with fermi nuclei. *Phys. Rev. A*, 46(7):3735, 1992.

[29] Tomonaga S. On a Relativistically Invariant Formulation of the Quantum Theory of Wave Fields*. *Prog.*, 1(2):27–42, 1946.

[30] Schwinger J. On quantum-electrodynamics and the magnetic moment of the electron. *Phys. Rev.*, 73:416–417, 1948.

[31] Feynman R. P. Mathematical formulation of the quantum theory of electromagnetic interaction. *Phys. Rev.*, 80:440–457, 1950.

[32] Grant I. P., McKenzie B. J., Norrington P. H., Mayers D. F., and Pyper N. C. An atomic multiconfiguration Dirac-Fock package. *Comput. Phys. Commun.*, 21:207–231, 1980.

[33] Mann J. B. and Johnson W. R. Breit interaction in multielectron atoms. *Phys. Rev. A*, 4:41–51, 1971.

[34] Pauli W. *Z. Phys.*, 31:765, 1925.

[35] Löwdin P. Quantum theory of many-particle systems. III. Extension of the Hartree-Fock scheme to include degenerate systems and correlation effects. *Phys. Rev.*, 97:1509–1520, 1955.

[36] Kemble E. C. *The Fundamental Principles of Quantum Mechanics.* Dover Publications, Inc., New York, USA, 1958.

[37] Nesbet R. *Variational Principles and Methods in Theoretical Physics and Chemistry.* Cambridge University Press, Cambridge, UK, 2004.

[38] Hartree D. *The Calculation of Atomic Structures.* Wiley, New York, USA, 1957.

[39] Gaigalas G., Rudzikas Z., and Froese Fischer C. An efficient approach for spin-angular integrations in atomic structure calculations. *J. Phys. B: At. Mol. Opt. Phys.*, 30:13747–3771, 1997.

[40] Gaigalas G., Fritzsche S., and Grant I. P. Program to calculate pure angular momentum coefficients in jj-coupling. *Comput. Phys. Commun.*, 139:263–278, 2001.

[41] Cowan R. D. *The Theory of Atomic Structure and Spectra.* Los Alamos Series in Basic and Applied Sciences, University California Press, USA, 1981.

[42] Pehlivan Rhodin A., Hartman H., Nilsson H., and Jönsson P. Experimental and theoretical oscillator strengths of Mg I for accurate abundance analysis. *A&A*, 598:A102, 2017.

[43] Grant I. P. Gauge invariance and relativistic radiative transitions. *J. Phys. B: At. Mol. Opt. Phys.*, 7(12):1458–1475, 1974.

[44] Froese Fischer C. and Godefroid M. R. Programs for computing *LS* and *LSJ* transitions from MCHF wave functions. *Comput. Phys. Commun.*, 64:501–519, 1991.

[45] Froese Fischer C. Evaluating the accuracy of theoretical transition data. T134:014019, 2009.

[46] Ekman J., Godefroid M., and Hartman H. Validation and implementation of uncertainty estimates of calculated transition rates. *Atoms*, 2:215–224, 2014.

[47] Seltzer E. C. K X-Ray Isotope Shifts. *Phys. Rev.*, 188:1916, (1969).

[48] Torbohm G., Fricke B., and Rosén A. State-dependent volume isotope shifts of low-lying states of group-IIa and -IIb elements. *Phys. Rev. A*, 31:2038, 1985.

[49] Blundell S., Baird P., Palmer C., Stacey D., and Woodgate G. A reformulation of the theory of field isotope shift in atoms. *J. Phys. B: At. Mol. Phys.*, 20:3663, 1987.

[50] Froese Fischer C., Brage T., and Jönsson P. *Computational atomic structure: An MCHF approach.* Institute of Physics Publishing, Bristol and Philadelphia, 1997.

[51] Kato T. On the eigenfunctions of many-particle systems in quantum mechanics. *Commun. Pure Appl. Math.*, 10:151, 1957.

[52] Olsen J., Roos B. O., Jørgensen P., and Jensen H. J. A. Determinant based configuration interaction algorithms for complete and restricted configuration interaction spaces. *J. Chem. Phys.*, 89:2185, 1988.

[53] Sturesson L., Jönsson P., and Froese Fischer C. JJGEN: A flexible program for generating lists of jj-coupled configuration state functions. *Comput. Phys. Commun.*, 177:539–550, 2007.

[54] Verdebout S., P. Jönsson, Gaigalas G., Godefroid M., and Froese Fischer C. Exploring biorthonormal transformations of pair-correlation functions in atomic structure variational calculations. *J. Phys. B: At. Mol. Opt. Phys.*, 43:074017, 2010.

[55] Godefroid M., Jönsson P., and Froese Fischer C. Atomic structure variational calculations in spectroscopy. *Phys. Scr.*, T78:33–46, 1998.

[56] Froese Fischer C., Jönsson P., and Godefroid M. Some two-electron properties of sodium. *Phys. Rev. A*, 57:1753, 1998.

[57] Henrik Jönsson. Personal communication on October 11, 2018.

[58] Käufl H-U., Ballester P., Biereichel P., et al. CRIRES: A high-resolution infrared spectrograph for ESO's VLT. *Ground-based Instrumentation for Astronomy*, 5492:1218–1227, 2004.

[59] Young E. T., Becklin E., Marcum P. M., and al. Early Science with SOFIA, the Stratospheric Observatory for Infrared Astronomy. *Astrophys. J. Lett.*, 749:L17, 2012.

[60] Dorn R. J., Anglada-Escude G., Baade D., et al. CRIRES+: Exploring the Cold Universe at High Spectral Resolution. *Messenger*, 156:7–11, 2014.

[61] Kramida A., Ralchenko Yu., Reader J., and NIST ASD Team. NIST Atomic Spectra Database (ver. 5.6.1), [Online]. Available: `https://physics.nist.gov/asd` [2015, April 16]. National Institute of Standards and Technology, Gaithersburg, MD., 2018.

[62] Weiss A. W. Series perturbations in atomic spectra: Superposition-of-configurations calculations on Al I and Al II. *Phys. Rev. A*, 9:1524–1536, 1974.

[63] Jörgen Ekman. ECT Workshop held in Trento, Italy, on August 25, 2015.

[64] Van Wijngaarden W. A. and Li J. Hyperfine splittings and isotope shifts of $(6s)^2\ ^1s_0 \longrightarrow (6s6p)\ ^1p_1$ transition in barium. *Can. J. Phys.*, 73:484, 1995.

[65] Nazé C., Li J. G., and Godefroid M. Theoretical isotope shifts in neutral barium. *Phys. Rev. A*, 91:032511, 2015.

[66] Brandau C., Kozhuharov C., Harman Z., Müller A., Schippers S., Kozhedub Y. S., Bernhardt D., Böhm S., Jacobi J., Schmidt E. W., et al. Isotope shift in the dielectronic recombination of three-electron $^A\mathrm{Nd}^{57+}$. *Phys. Rev. Lett.*, 100:073201, 2008.

[67] Reinhard P. G., Nazarewicz W., and Garcia Ruiz R. F. Beyond the charge radius: the information content of the fourth radial moment. arXiv preprint, 2019.

Scientific publications

Paper I

A&A 621, A16 (2019)
https://doi.org/10.1051/0004-6361/201833764

Astronomy & Astrophysics

Extended transition rates and lifetimes in Al I and Al II from systematic multiconfiguration calculations*

A. Papoulia (Ασημίνα Παπούλια)[1,2], J. Ekman[1], and P. Jönsson[1]

[1] Materials Science and Applied Mathematics, Malmö University, 20506 Malmö, Sweden
e-mail: asimina.papoulia@mau.se
[2] Division of Mathematical Physics, Lund University, Post Office Box 118, 22100 Lund, Sweden

Received 3 July 2018 / Accepted 22 September 2018

ABSTRACT

MultiConfiguration Dirac-Hartree-Fock (MCDHF) and relativistic configuration interaction (RCI) calculations were performed for 28 and 78 states in neutral and singly ionized aluminium, respectively. In Al I, the configurations of interest are $3s^2nl$ for $n = 3, 4, 5$ with $l = 0$ to 4, as well as $3s3p^2$ and $3s^26l$ for $l = 0, 1, 2$. In Al II, in addition to the ground configuration $3s^2$, the studied configurations are 3snl with $n = 3$ to 6 and $l = 0$ to 5, $3p^2$, 3s7s, 3s7p, and 3p3d. Valence and core-valence electron correlation effects are systematically accounted for through large configuration state function (CSF) expansions. Calculated excitation energies are found to be in excellent agreement with experimental data from the National Institute of Standards and Technology (NIST) database. Lifetimes and transition data for radiative electric dipole (E1) transitions are given and compared with results from previous calculations and available measurements for both Al I and Al II. The computed lifetimes of Al I are in very good agreement with the measured lifetimes in high-precision laser spectroscopy experiments. The present calculations provide a substantial amount of updated atomic data, including transition data in the infrared region. This is particularly important since the new generation of telescopes are designed for this region. There is a significant improvement in accuracy, in particular for the more complex system of neutral Al I. The complete tables of transition data are available at the CDS.

Key words. atomic data

1. Introduction

Aluminium is an important element in astrophysics. In newly born stars the galactic [Al/H] abundance ratio and the [Al/Mg] ratio are found to be increased in comparison to early stars (Clayton 2003). The aluminium abundance and its anti-correlation with that of magnesium is the best tool to determine which generation a globular cluster star belongs to. The abundance variations of different elements and the relative numbers of first- and second-generation stars can be used to determine the nature of polluting stars, the timescale of the star formation episodes, and the initial mass function of the stellar cluster (Carretta et al. 2010). The aluminium abundance is of importance for other types and groups of stars as well. A large number of spectral lines of neutral and singly ionized aluminium are observed in the solar spectrum and in many stellar spectra. Aluminium is one of the interesting elements for chemical analysis of the Milky Way, and one example is the *Gaia*-ESO Survey[1]; medium- and high-resolution spectra from more than 10^5 stars are analysed to provide public catalogues with astrophysical parameters. As part of this survey, Smiljanic et al. (2014) analysed high-resolution UVES[2] spectra of FGK-type stars and derived abundances for 24 elements, including aluminium.

In addition, aluminium abundances have been determined in local disk and halo stars by Gehren et al. (2004), Reddy et al. (2006), Mishenina et al. (2008), Adibekyan et al. (2012), and Bensby et al. (2014). However, chemical evolution models still have problems reproducing the observed behaviour of the aluminium abundance in relation to abundances of other elements. Such examples are the observed trends of the aluminium abundances in relation to metallicity [Fe/H], which are not well reproduced at the surfaces of stars, for example giants and dwarfs (Smiljanic et al. 2016). In light of the above issues, Smiljanic et al. (2016) redetermined aluminium abundances within the *Gaia*-ESO Survey. Furthermore, strong deviations from local thermodynamic equilibrium (LTE) are found to significantly affect the inferred aluminium abundances in metal poor stars, which was highlighted in the work by Gehren et al. (2006). Nordlander & Lind (2017) presented a non-local thermodynamic equilibrium (NLTE) modelling of aluminium and provided abundance corrections for lines in the optical and near-infrared regions.

Correct deduction of aluminium abundances and chemical evolution modelling is thus necessary to put together a complete picture of the stellar and Galactic evolution. Obtaining the spectroscopic reference data to achieve this goal is demanding. A significant amount of experimental research has been conducted to probe the spectra of Al II and Al I and to facilitate the analysis of the astrophysical observations. Even so, some laboratory measurements still lack reliability and in many cases, especially when going to higher excitation energies, only theoretical values of transition properties exist. Accurate computed atomic data are

* The data are only available available at the CDS via anonymous ftp to cdsarc.u-strasbg.fr (130.79.128.5) or via http://cdsarc.u-strasbg.fr/viz-bin/qcat?J/A+A/621/A16
[1] http://casu.ast.cam.ac.uk/surveys-projects/ges
[2] http://www.eso.org/sci/facilities/paranal/instruments/uves.html

therefore essential to make abundance analyses in the Sun and other stars possible.

For the singly ionized Al II, there are a number of measurements of transition properties. The radiative lifetime of the $3s3p\ ^3P^o_1$ level was measured by Johnson et al. (1986) using an ion storage technique and the transition rate value for the inter-combination $3s3p\ ^3P^o_1 \rightarrow 3s^2\ ^1S_0$ transition was provided. Träbert et al. (1999) measured lifetimes in an ion storage ring and the result for the lifetime of the $3s3p\ ^3P^o_1$ level is in excellent agreement with the value measured by Johnson et al. (1986). Using the beam-foil technique, Andersen et al. (1971) measured lifetimes for the $3snf\ ^3F$ series with $n = 4$–7, although these measurements are associated with significant uncertainties. By using the same technique, the lifetime of the singlet $3s3p\ ^1P^o_1$ level was measured in four different experimental works (Kernahan et al. 1979; Head et al. 1976; Berry et al. 1970; Smith 1970), which are in very good agreement.

In the case of neutral Al I, several measurements have also been performed. Following a sequence of earlier works (Jönsson & Lundberg 1983; Jönsson et al. 1984), Buurman et al. (1986) used laser spectroscopy to obtain experimental values for the oscillator strengths of the lowest part of the spectrum. A few years later, Buurman & Dönszelmann (1990) redetermined the lifetime of the $3s^24p\ ^2P$ level and separated the different fine-structure components. Using similar laser techniques, Davidson et al. (1990) measured the natural lifetimes of the $3s^2nd\ ^2D$ Rydberg series and obtained oscillator strengths for transitions to the ground state. In a more recent work, Vujnović et al. (2002) used the hollow cathode discharge method to measure relative intensities of spectral lines of both neutral and singly ionized aluminium. Absolute transition probabilities were evaluated based on available results from previous studies, such as the ones mentioned above.

Al II is a nominal two-electron system and the lower part of its spectrum is strongly influenced by the interaction between the $3s3d\ ^1D$ and $3p^2\ ^1D$ configuration states. Contrary to neutral Mg I where no level is classified as $3p^2\ ^1D$, in Al II the $3p^2$ configuration dominates the lowest ^1D term and yields a well-localized state below the $3s3d\ ^1D$ term. The interactions between the $3snd\ ^1D$ Rydberg series and the $3p^2\ ^1D$ perturber were investigated by Tayal & Hibbert (1984). Going slightly further up, the spectrum of Al II is governed by the strong mixing of the $3snf\ ^3F$ Rydberg series with the $3p3d\ ^3F$ term. Despite the widespread mixing, $3p3d\ ^3F$ is also localized, between the $3s6f\ ^3F$ and $3s7f\ ^3F$ states. The configuration interaction between doubly excited states (e.g. the $3p^2\ ^1D$ and $3p3d\ ^3F$ states) and singly excited $3snl\ ^{1,3}L$ states was thoroughly investigated by Chang & Wang (1987). However, the extreme mixing of the $3p3d\ ^3F$ term in the $3snf\ ^3F$ series and its effect on the computation of transition properties was first investigated by Weiss (1974). Although the work by Chang & Wang (1987) was more of a qualitative nature, computed transition data were provided based on configuration interaction (CI) calculations. Using the B-spline configuration interaction (BSCI) method, Chang & Fang (1995) also predicted transition properties and lifetimes of Al II excited states.

Despite the large number of measured spectral lines in Al I, the $3s3p^2\ ^2D$ state could not be experimentally identified and for a long time theoretical calculations had been trying to localize it and predict whether it lies above or below the first-ionization limit. Al I is a system with three valence electrons, and the correlation effects are even stronger than in the singly ionized Al II. Especially strong is the two-electron interaction of $3s3d\ ^1D$ with $3p^2\ ^1D$, which becomes evident between the $3s^23d\ ^2D$ and $3s3p^2\ ^2D$ states. The $3s3p^2\ ^2D$ state is strongly coupled to the $3s^23d\ ^2D$ state, but it is also smeared out over the entire discrete part of the $3s^2nd\ ^2D$ series and contributes to a significant mixing of all those states (Weiss 1974). Asking for the position of the $3s3p^2\ ^2D$ level is thus meaningless since it does not correspond to any single spectral line (Lin 1974; Trefftz 1988). Due to this strong two-electron interaction, the line strength of one of the ^2D states involved in a transition appears to be enhanced, while the line strength of the other ^2D state is suppressed. This makes the computation of transition properties in Al I far from trivial (Froese Fischer et al. 2006). More theoretical studies on the system of neutral aluminium were conducted by Taylor et al. (1988) and Theodosiou (1992).

In view of the great astrophysical interest for accurate atomic data, close coupling (CC) calculations were carried out for the systems of Al II and Al I by Butler et al. (1993) and Mendoza et al. (1995), respectively, as part of the Opacity Project. These extended spectrum calculations produced transition data in the infrared region (IR), which had been scarce until then. However, the neglected relativistic effects and the insufficient amount of correlation included in the calculations constitute limiting factors to the accuracy of the results. Later on, Froese Fischer et al. (2006) performed MultiConfiguration Hartree-Fock (MCHF) calculations and used the Breit-Pauli (BP) approximation to also capture relativistic effects for Mg- and Al-like sequences. Focusing more on correlation, relativistic effects were kept to lower order. Even so, in Al I, correlation in the core and core-valence effects were not included due to limited computational resources. The latest compilation of Al II and Al I transition probabilities was made available by Kelleher & Podobedova (2008a). Wiese & Martin (1980) had earlier updated the first critical compilation of atomic data by Wiese et al. (1969).

Although for the past decades a considerable amount of research has been conducted for the systems of Al II and Al I, there is still a need for extended and accurate theoretical transition data. The present study is motivated by such a need. To obtain energy separations and transition data, the fully relativistic MultiConfiguration Dirac-Hartree-Fock (MCDHF) scheme has been employed. Valence and core-valence electron correlation is included in the computations of both systems. Spectrum calculations have been performed to include the first 28 and 78 lowest states in neutral and singly ionized aluminium, respectively. Transition data corresponding to IR lines have also been produced. The excellent description of energy separations is an indication of highly accurate computed atomic properties, which can be used to improve the interpretation of abundances in stars.

2. Theory

2.1. MultiConfiguration Dirac-Hartree-Fock approach

The wave functions describing the states of the atom, referred to as atomic state functions (ASFs), are obtained by applying the MCDHF approach (Grant 2007; Froese Fischer et al. 2016). In the MCDHF method, the ASFs are approximate eigenfunctions of the Dirac-Coulomb Hamiltonian given by

$$H_{DC} = \sum_{i=1}^{N}[c\ \boldsymbol{\alpha}_i \cdot \mathbf{p}_i + (\beta_i - 1)c^2 + V_{\rm nuc}(r_i)] + \sum_{i<j}^{N}\frac{1}{r_{ij}}, \qquad (1)$$

where $V_{\rm nuc}(r_i)$ is the potential from an extended nuclear charge distribution, $\boldsymbol{\alpha}$ and β are the 4×4 Dirac matrices, c the speed of light in atomic units, and $\mathbf{p} \equiv -i\nabla$ the electron momentum

operator. An ASF $\Psi(\gamma PJM_J)$ is given as an expansion over $N_{\rm CSF}$ configuration state functions (CSFs), $\Phi(\gamma_i PJM_J)$, characterized by total angular momentum J and parity P:

$$\Psi(\gamma PJM_J) = \sum_{i=1}^{N_{\rm CSF}} c_i \Phi(\gamma_i PJM_J). \quad (2)$$

The CSFs are anti-symmetrized many-electron functions built from products of one-electron Dirac orbitals and are eigenfunctions of the parity operator P, the total angular momentum operator J^2 and its projection on the z-axis J_z (Grant 2007; Froese Fischer et al. 2016). In the expression above, γ_i represents the configuration, coupling, and other quantum numbers necessary to uniquely describe the CSFs.

The radial parts of the Dirac orbitals together with the mixing coefficients c_i are obtained in a self-consistent field (SCF) procedure. The set of SCF equations to be iteratively solved results from applying the variational principle on a weighted energy functional of all the studied states according to the extended optimal level (EOL) scheme (Dyall et al. 1989). The angular integrations needed for the construction of the energy functional are based on the second quantization method in the coupled tensorial form (Gaigalas et al. 1997, 2001).

The transverse photon (Breit) interaction and the leading quantum electrodynamic (QED) corrections (vacuum polarization and self-energy) can be accounted for in subsequent relativistic configuration interaction (RCI) calculations (McKenzie et al. 1980). In the RCI calculations, the Dirac orbitals from the previous step are fixed and only the mixing coefficients of the CSFs are determined by diagonalizing the Hamiltonian matrix. All calculations were performed using the relativistic atomic structure package GRASP2K (Jönsson et al. 2013).

In the MCDHF relativistic calculations, the wave functions are expansions over jj-coupled CSFs. To identify the computed states and adapt the labelling conventions followed by the experimentalists, the ASFs are transformed from jj-coupling to a basis of LSJ-coupled CSFs. In the GRASP2K code this is done using the methods developed by Gaigalas et al. (2003, 2004, 2017).

2.2. Transition parameters

In addition to excitation energies, lifetimes τ and transition parameters, such as emission transition rates A and weighted oscillator strengths gf, were also computed. The transition parameters between two states $\gamma' P' J'$ and γPJ are expressed in terms of reduced matrix elements of the transition operator $\mathbf{T}$ (Grant 1974):

$$\langle \Psi(\gamma PJ) \| \mathbf{T} \| \Psi(\gamma' P' J') \rangle = \sum_{k,l} c_k c'_l \langle \Phi(\gamma_k PJ) \| \mathbf{T} \| \Phi(\gamma'_l P' J') \rangle. \quad (3)$$

For electric multipole transitions, there are two forms of the transition operator: the length, which in fully relativistic calculations is equivalent to the Babushkin gauge, and the velocity form, which is equivalent to the Coulomb gauge. The transitions are governed by the outer part of the wave functions. The length form is more sensitive to this part of the wave functions and it is generally considered to be the preferred form. Regardless, the agreement between the values of these two different forms can be used to indicate the accuracy of the wave functions (Froese Fischer 2009; Ekman et al. 2014). This is particularly useful when no experimental measurements are available. The transitions can be organized in groups determined, for instance, by the magnitude of the transition rate value. A statistical analysis of the uncertainties of the transitions can then be performed. For each group of transitions the average uncertainty of the length form of the computed transition rates is given by

$$\langle {\rm d}T \rangle = \frac{1}{N} \sum_{i=1}^{N} \frac{|A_l^i - A_v^i|}{\max(A_l^i, A_v^i)}, \quad (4)$$

where A_l and A_v are respectively the transition rates in length and velocity form for a transition i and N is the number of the transitions belonging to a group. In this work, we only computed transition parameters for the electric dipole (E1) transitions. The electric quadrupole (E2) and magnetic multipole (Mk) transitions are much weaker and therefore less likely to be observed.

3. Calculations

3.1. Al I

In neutral aluminium, calculations were performed in the EOL scheme (Dyall et al. 1989) for 28 targeted states. These states belong to the $3s^2$ns configurations with $n = 4, 5, 6$, the $3s^2$nd configurations with $n = 3, ..., 6$, and the $3s3p^2$ and $3s^25g$ configurations, characterized by even parity, and on the other hand the $3s^2$np configurations with $n = 3, .., 6$ and the $3s^24f$ and $3s^25f$ configurations, characterized by odd parity. These configurations define what is known as the multireference (MR). From initial calculations and analysis of the eigenvector compositions, we deduced that all $3p^2$nl configurations, in addition to the targeted $3s^2$nl, give considerable contributions to the total wave functions and should be included in the MR. Following the active set (AS) approach (Olsen et al. 1988; Sturesson et al. 2007), the CSF expansions (see Eq. (2)) were obtained by allowing single and restricted double (SD) substitutions of electrons from the reference (MR) orbitals to an AS of correlation orbitals. The AS is systematically increased by adding layers of orbitals to effectively build nearly complete wave functions. This is achieved by keeping track of the convergence of the computed excitation energies, and of the other physical quantities of interest, such as the transition parameters here.

As a first step an MCDHF calculation was performed for the orbitals that are part of the MR. States with both even and odd parity were simultaneously optimized. Following this step, we continued to optimize six layers of correlation orbitals based on valence (VV) substitutions. The VV expansions were obtained by allowing SD substitutions from the three outer valence orbitals in the MR, with the restriction that there will be at most one substitution from orbitals with $n = 3$. In this manner, the correlation orbitals will occupy the space between the inner $n = 3$ valence orbitals and the outer orbitals involved in the higher Rydberg states (see Fig. 1). These orbitals have been shown to be of crucial importance for the transition probabilities, which are weighted towards this part of the space (Pehlivan Rhodin et al. 2017; Pehlivan Rhodin 2018). The six correlation layers correspond to the 12s, 12p, 12d, 11f, 11g, and 10h set of orbitals.

Each MCDHF calculation was followed by an RCI calculation for an extended expansion, obtained by single, double, and triple (SDT) substitutions from the valence orbitals. As a final step, an RCI calculation was performed for the largest SDT valence expansion augmented by a core-valence (CV) expansion. The CV expansion was obtained by allowing SD substitutions from the valence orbitals and the $2p^6$ core, with the restriction that there will be at most one substitution from

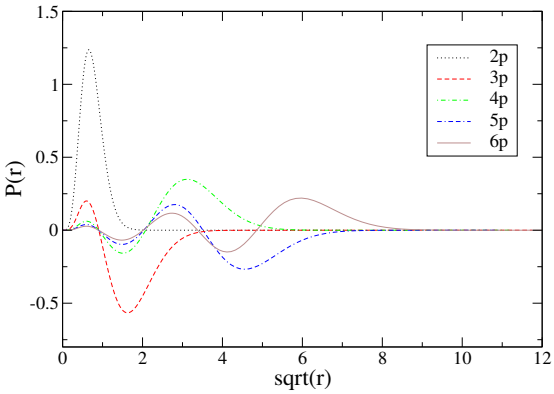

Fig. 1. Al I Dirac-Fock radial orbitals for the p symmetry, as a function of $\sqrt{r}$. The 2p orbital is part of the core and the orbitals from $n = 3$ to $n = 6$ are part of the valence electron cloud. These orbitals occupy different regions in space and the overlap between some of the Rydberg states is minor.

$2p^6$. All the RCI calculations included the Breit interaction and the leading QED effects. Accounting for CV correlation does not lower the total energies significantly, but it can have large effects on the energy separations and thus we considered it crucial. Core-valence correlation is also important for transition properties (Hibbert 1989). Core-core (CC) correlation, obtained by allowing double excitations from the core, is known to be less important and has not been considered in the present work. The number of CSFs in the final even and odd state expansions, accounting for both VV and CV electron correlation, were 4 362 628 and 2 889 385, respectively, distributed over the different J symmetries.

3.2. Al II

In the singly ionized aluminium, the calculations were more extended, including 78 targeted states. These states belong to the $3s^2$ ground configuration, and to the $3p^2$; the 3sns configurations with $n = 4, ..., 7$; the 3snd with $n = 3, ..., 6$; and the 3s5g and 3s6g configurations, characterized by even parity, and on the other hand, the 3snp configurations with $n = 3, ..., 7$; the 3snf with $n = 4, 5, 6$; and the 3s6h and 3p3d configurations, characterized by odd parity. These configurations define the multireference (MR). In the computations of Al II, the EOL scheme was applied and the CSF expansions were obtained following the active set (AS) approach, accounting for VV and CV correlation. Al II is less complex and the CSF expansions generated from (SD) substitutions are not as large as those in Al I. Hence, we can afford both 2s and 2p orbitals to account for CV correlation. The 1s core orbital remained closed and, as it was for Al I, core-core correlation was neglected. The MCDHF calculations were performed in a similar way to the calculations in Al I, yet no particular restrictions were imposed on the VV substitutions. We optimized six correlation layers corresponding to the 13s, 13p, 12d, 12f, 12g, 8h, and 7i set of orbitals. Each MCDHF calculation was followed by an RCI calculation. Finally, an RCI calculation was performed for the largest SD valence expansion augmented by the CV expansion. The number of CSFs in the final even and odd state expansions, accounting for both VV and CV electron correlation, were 911 795 and 1 269 797, respectively, distributed over the different J symmetries.

4. Results

4.1. Al I

In Table 1 the computed excitation energies, based on VV correlation, are given as a function of the increasing active set of orbitals. After adding the $n = 11$ correlation layer, we note that the energy values for all 28 targeted states have converged. For comparison, in the second last column the observed energies from the National Institute of Standards and Technology (NIST) Atomic Spectra Database (Kramida et al. 2018) are displayed. All energies but those belonging to the $3s3p^2$ configuration are already in good agreement with the NIST recommended values. The relative differences between theory and experiment for all three levels of the quartet $3s3p^2\ ^4P$ state is 3.1%, while the mean relative difference for the rest of the states is less than 0.2%. In the third last column, the computed excitation energies after accounting for CV correlation are displayed. When taking into account CV effects the agreement with the observed values is better overall. Most importantly, for the $3s3p^2\ ^4P$ levels the relative differences between observed and computed values decrease to less than 0.6%. The likelihood that the $1s^22s^22p^6$ core overlaps with the $3s3p^2$ cloud of electrons is much less than that for $3s^2$nl. Consequently, when CV correlation is taken into account the lowering of the $3s3p^2$ energy levels is much smaller than for levels belonging to any $3s^2$nl configuration. Thus, the adjustments to the separation energies will be minor between the ground state $3s^23p$ and $3s^2$nl levels, but significant between the $3s^23p$ and $3s3p^2$ levels. In the last column of Table 1 the differences $\Delta E = E_{\rm obs} - E_{\rm theor}$, between the final (CV) computed and the observed energies, are also displayed. In principle, there are two groups of values; the one consisting of the $3s^2$nd configurations exhibits the smallest absolute discrepancies from the observed energies. For the rest, the absolute discrepancies are somewhat larger.

In the calculations, the labelling of the eigenstates is determined by the CSF with the largest coefficient in the expansion of Eq. (2). When the same label is assigned to different eigenstates, a detailed analysis can be performed by displaying their LS-compositions. In Table 1, we note that two of the states have been assigned the same label, i.e. $3s^24d\ ^2D$, and thus the subscripts a and b are used to distinguish them. In Table 2, we give the LS-composition of all computed $3s^2$nd ^{2}D states, including the three most dominant CSFs. The $3s^24d\ ^2D$ term appears twice as the CSF with the largest LS-composition. Moreover, the admixture of the $3s3p^2\ ^2D$ in the four lowest $3s^2$nd ^{2}D states is rather strong and adds up to 65%. That being so, the $3s3p^2\ ^2D$ does not exist in the calculated spectrum as a localized state. For comparison, in the last column of Table 2 the labelling of the observed $3s^2$nd ^{2}D states is also given. In the observed configurations presented by NIST (Kramida et al. 2018), the second highest $3s^2$nd ^{2}D term has not been given any specific label and it is therefore designated as $y\ ^2D$. The higher ^{2}D terms are designated as $3s^24d$, $3s^25d$, and so on.

In Table 3, the current results for the lowest excitation energies are compared with the values from the MCHF-BP calculations by Froese Fischer et al. (2006). The latter calculations are extended up to levels corresponding to the doublet $3s^24p\ ^2P$ state. The differences ΔE between observed and computed energies are given in the last two columns for the different computational approaches. As can be seen, when using the current MCDHF and RCI method the agreement with the observed energies is substantially improved for all levels and in particular, for those belonging to the quartet $3s3p^2\ ^4P$ state. In the MCHF-BP calculations, core-valence correlation was neglected. As

Table 1. Computed excitation energies in cm^{-1} for the 28 lowest states in Al I.

			VV								
Pos.	Conf.	*LS J*	$n = 7$	$n = 8$	$n = 9$	$n = 10$	$n = 11$	$n = 12$	CV	E_{obs}[a]	ΔE
1	$3s^2\,3p$	$^2P^o_{1/2}$	0	0	0	0	0	0	0	0	0
2		$^2P^o_{3/2}$	108	108	108	108	108	108	104	112	8
3	$3s^2\,4s$	$^2S_{1/2}$	25 318	25 377	25 416	25 419	25 427	25 429	25 196	25 348	152
4	$3s\,3p^2$	$^4P_{1/2}$	27 788	27 966	28 073	28 085	28 109	28 111	28 863	29 020	157
5		$^4P_{3/2}$	27 833	28 011	28 118	28 130	28 154	28 156	28 907	29 067	160
6		$^4P_{5/2}$	27 906	28 085	28 191	28 204	28 227	28 230	28 981	29 143	162
7	$3s^2\,3d$	$^2D_{3/2}$	32 211	32 077	32 135	32 139	32 150	32 150	32 414	32 435	21
8		$^2D_{5/2}$	32 212	32 079	32 137	32 141	32 152	32 152	32 416	32 437	21
9	$3s^2\,4p$	$^2P^o_{1/2}$	32 770	32 879	32 935	32 937	32 946	32 949	32 801	32 950	149
10		$^2P^o_{3/2}$	32 786	32 894	32 951	32 952	32 962	32 964	32 814	32 966	152
11	$3s^2\,5s$	$^2S_{1/2}$	37 493	37 637	37 693	37 694	37 704	37 706	37 512	37 689	177
12	$3s^2\,4d$	$^2D_{3/2\,a}$	38 733	38 659	38 711	38 707	38 717	38 718	38 951	38 929	−22
13		$^2D_{5/2\,a}$	38 736	38 664	38 717	38 712	38 722	38 724	38 957	38 934	−23
14	$3s^2\,5p$	$^2P^o_{1/2}$	40 038	40 187	40 252	40 249	40 259	40 262	40 101	40 272	171
15		$^2P^o_{3/2}$	40 043	40 193	40 258	40 255	40 265	40 268	40 106	40 278	172
16	$3s^2\,4f$	$^2F^o_{5/2}$	41 050	41 209	41 282	41 287	41 297	41 300	41 163	41 319	156
17		$^2F^o_{7/2}$	41 050	41 209	41 282	41 287	41 297	41 300	41 163	41 319	156
18	$3s^2\,6s$	$^2S_{1/2}$	41 897	42 069	42 133	42 135	42 144	42 143	41 964	42 144	180
19	$3s^2\,4d$	$^2D_{3/2\,b}$	42 105	42 071	42 121	42 108	42 119	42 121	42 232	42 234	2
20		$^2D_{5/2\,b}$	42 109	42 075	42 126	42 112	42 123	42 125	42 237	42 238	1
21	$3s^2\,6p$	$^2P^o_{1/2}$	43 076	43 246	43 316	43 311	43 321	43 324	43 160	43 335	175
22		$^2P^o_{3/2}$	43 079	43 249	43 318	43 313	43 324	43 326	43 162	43 338	176
23	$3s^2\,5f$	$^2F^o_{5/2}$	43 549	43 721	43 795	43 801	43 811	43 813	43 660	43 831	171
24		$^2F^o_{7/2}$	43 549	43 721	43 795	43 801	43 811	43 813	43 660	43 831	171
25	$3s^2\,5g$	$^2G_{7/2}$	43 576	43 763	43 838	43 845	43 856	43 859	43 687	43 876	189
26		$^2G_{9/2}$	43 576	43 763	43 838	43 845	43 856	43 859	43 687	43 876	189
27	$3s^2\,5d$	$^2D_{3/2}$	44 034	44 059	44 115	44 096	44 106	44 109	44 126	44 166	40
28		$^2D_{5/2}$	44 036	44 062	44 117	44 099	44 109	44 111	44 129	44 169	40

Notes. The energies are given as a function of the increasing active set of orbitals, accounting for VV correlation, where n indicates the maximum principle quantum number of the orbitals included in the active set. In Col. 10, the final energy values are displayed after accounting for CV correlation. The differences ΔE between the final computations and the observed values are shown in the last column. The sequence and labelling of the configurations and *LS J*-levels are in accordance with the final (CV) computed energies. The $3s^24d\ ^2D$ term is assigned twice throughout the calculations (see also Table 2) and the subscripts *a* and *b* are used to distinguish them. See text for details.
References. [(a)]NIST Atomic Spectra Database 2018 (Kramida et al. 2018).

Table 2. *LS*-composition of the computed states belonging to the strongly mixed $3s^2$nd Rydberg series in Al I.

Pos.	Conf.	*LS J*	*LS*-composition	Label used in NIST[(1)]
7,8	$3s^2\,3d$	$^2D_{3/2,5/2}$	$0.67 + 0.19\ 3s\,3p^2\ ^2D + 0.04\ 3s^2\,4d\ ^2D$	$3s^2\,3d\ ^2D_{3/2,5/2}$
12,13	$3s^2\,4d$	$^2D_{3/2,5/2\,a}$	$0.41 + 0.22\ 3s^2\,3d\ ^2D + 0.21\ 3s\,3p^2\ ^2D$	$3s^2$ nd y $^2D_{3/2,5/2}$
19,20	$3s^2\,4d$	$^2D_{3/2,5/2\,b}$	$0.44 + 0.25\ 3s^2\,5d\ ^2D + 0.15\ 3s\,3p^2\ ^2D$	$3s^2\,4d\ ^2D_{3/2,5/2}$
27,28	$3s^2\,5d$	$^2D_{3/2,5/2}$	$0.58 + 0.19\ 3s^2\,6d\ ^2D + 0.10\ 3s\,3p^2\ ^2D$	$3s^2\,5d\ ^2D_{3/2,5/2}$

Notes. The three most dominant *LS*-components are displayed. The first percentage value corresponds to the assigned configuration and term. In all these cases, the percentages for the two different *LS J*-levels are the same and are therefore given in the same line. In the last column we provide the labelling of the corresponding observed terms as given in the NIST Database. The first column refers to the positions according to Table 1.
References. [(1)]Kramida et al. (2018).

mentioned above and also acknowledged by Froese Fischer et al. (2006), capturing such correlation effects is crucial for 3s-hole states, such as states with significant $3s3p^2$ composition. Furthermore, the $\Delta E_{MCHF-BP}$ values do not always have the same sign, while the ΔE_{RCI} differences are consistently positive. This is particularly important when calculating transition properties. On average, properties for transitions between two levels for which the differences $\Delta E_{MCHF-BP}$ have opposite signs are estimated less accurately.

The complete transition data tables, for all computed E1 transitions in Al I, can be found at the CDS. In the CDS table, the transition energies, wavelengths and the length form of the

Table 3. Observed and computed excitation energies in cm^{-1} for the 10 and 20 lowest states in Al I and Al II, respectively.

Pos.	Conf.	LSJ	E_{obs} [a]	E_{RCI} [b]	ΔE_{RCI} [b]	$\Delta E_{MCHF-BP}$ [c]
			Al I			
1	$3s^2\,3p$	$^2P^o_{1/2}$	0	0	0	0
2		$^2P^o_{3/2}$	112	104	8	22
3	$3s^2\,4s$	$^2S_{1/2}$	25 348	25 196	152	−235
4	$3s\,3p^2$	$^4P_{1/2}$	29 020	28 863	157	940
5		$^4P_{3/2}$	29 067	28 907	160	949
6		$^4P_{5/2}$	29 143	28 981	162	964
7	$3s^2\,3d$	$^2D_{3/2}$	32 435	32 414	21	250
8		$^2D_{5/2}$	32 437	32 416	21	251
9	$3s^2\,4p$	$^2P^o_{1/2}$	32 950	32 801	149	−98
10		$^2P^o_{3/2}$	32 966	32 814	152	−94
			Al II			
1	$3s^2$	$^1S_0$	0	0	0	0
2	$3s\,3p$	$^3P^o_0$	37 393	37 445	−52	9
3		$^3P^o_1$	37 454	37 503	−49	8
4		$^3P^o_2$	37 578	37 626	−48	6
5		$^1P^o_1$	59 852	59 982	−130	−177
6	$3p^2$	$^1D_2$	85 481	85 692	−211	−305
7	$3s\,4s$	$^3S_1$	91 275	91 425	−150	−376
8	$3p^2$	$^3P_0$	94 085	94 211	−126	−107
9		$^3P_1$	94 147	94 264	−117	−111
10		$^3P_2$	94 269	94 375	−106	−113
11	$3s\,4s$	$^1S_0$	95 351	95 543	−192	−400
12	$3s\,3d$	$^3D_2$	95 549	95 791	−242	−527
13		$^3D_1$	95 551	95 794	−243	−527
14		$^3D_3$	95 551	95 804	−253	−529
15	$3s\,4p$	$^3P^o_0$	105 428	105 582	−154	−357
16		$^3P^o_1$	105 442	105 594	−152	−360
17		$^3P^o_2$	105 471	105 623	−152	−363
18		$^1P^o_1$	106 921	107 132	−211	−365
19	$3s\,3d$	$^1D_2$	110 090	110 330	−240	−475
20	$3p^2$	$^1S_0$	111 637	112 086	−449	−445

Notes. In the last two columns, the difference ΔE between observed and computed energies is compared for the current RCI and previous MCHF-BP calculations.
References. [(a)]Kramida et al. (2018); [(b)]present calculations; [(c)]Froese Fischer et al. (2006).

Table 4. Statistical analysis of the uncertainties of the computed transition rates in Al I and Al II.

	A^{low}_{RCI}	A^{high}_{RCI}	No.Trans.	$\langle dT\rangle$	Q_3	Max
			Al I			
1		1.00E+05	31	0.62	0.83	0.98
2	1.00E+05	1.00E+06	25	0.29	0.37	0.81
3	1.00E+06	1.00E+07	24	0.055	0.076	0.15
4	1.00E+07		20	0.043	0.073	0.14
			Al II			
1		1.00E+05	109	0.07	0.11	0.61
2	1.00E+05	1.00E+06	81	0.09	0.11	0.67
3	1.00E+06	1.00E+07	99	0.043	0.036	0.39
4	1.00E+07		141	0.011	0.009	0.12

Notes. The transition rates are arranged in four groups and in Col. 4, the number of transitions belonging to each group is given. In the last three columns, the average value, the value Q_3 containing 75% of the lowest computed dT values, and the maximum value are given for each group of transitions. All transition rates are given in s^{-1}.

transition rates A, and weighted oscillator strengths gf are given. Based on the agreement between the length and velocity forms of the computed transition rates A_{RCI}, a statistical analysis of the uncertainties can be preformed. The transitions were arranged in four groups based on the magnitude of the A_{RCI} values. The first two groups contain all the weak transitions with transition rates up to $A = 10^6\ s^{-1}$, while the next two groups contain the strong transitions with $A > 10^6\ s^{-1}$. In Table 4, the average value of the uncertainties $\langle dT\rangle$ (see Eq. (4)) is given for each group of transitions. To better understand how the individual uncertainties dT are distributed, the maximum value and the value Q_3 containing 75% of the lowest computed dT values (third quartile) are also given in Table 4. When examining the predicted uncertainties of the individual groups, we deduce that for all the strong transitions dT always remains below 15%. Most of the strong transitions are associated with small uncertainties, which justifies the low average values. Contrary to the strong transitions, the weaker transitions are associated with considerably larger uncertainties. This is even more pronounced for the first group of transitions where A is less than $10^5\ s^{-1}$. The weak E1 transitions are challenging, and therefore interesting, from a theoretical point

Table 5. Comparison between computed and observed transition rates A in s^{-1} for selected transitions in Al I.

Upper	Lower	A_{RCI} [a]	$A_{MCHF-BP}$ [b]	A_{CC} [c]	A_{obs} [d,e,f]	A_{obs} [g]
$3s^2\ 4s\ ^2S_{1/2}$	$3s^2\ 3p\ ^2P^o_{1/2}$	4.966E+07	5.098E+07		4.93E+07 [d C]	4.70E+07 [B]
	$3s^2\ 3p\ ^2P^o_{3/2}$	9.884E+07	10.15E+07		9.80E+07 [d C]	9.90E+07 [B]
$3s^2\ 5s\ ^2S_{1/2}$	$3s^2\ 3p\ ^2P^o_{1/2}$	1.277E+07			1.33E+07 [d C]	1.42E+07 [C+]
	$3s^2\ 3p\ ^2P^o_{3/2}$	2.534E+07			2.64E+07 [d C]	2.84E+07 [C+]
$3s^2\ 5s\ ^2S_{1/2}$	$3s^2\ 4p\ ^2P^o_{1/2}$	3.815E+06				3.00E+06 [D]
	$3s^2\ 4p\ ^2P^o_{3/2}$	7.599E+06				6.00E+06 [D]
$3s^2\ 4p\ ^2P^o_{1/2}$	$3s^2\ 4s\ ^2S_{1/2}$	1.580E+07	1.507E+07		1.69E+07 [e C+]	1.60E+07 [A]
$3s^2\ 4p\ ^2P^o_{3/2}$	$3s^2\ 4s\ ^2S_{1/2}$	1.587E+07	1.514E+07		1.69E+07 [e C+]	1.50E+07 [B]
$3s^2\ 3d\ ^2D_{3/2}$	$3s^2\ 3p\ ^2P^o_{1/2}$	6.542E+07	5.651E+07		6.30E+07 [d C]	5.90E+07 [C+]
	$3s^2\ 3p\ ^2P^o_{3/2}$	1.321E+07	1.140E+07			(1.20)E+07
$3s^2\ 3d\ ^2D_{5/2}$	$3s^2\ 3p\ ^2P^o_{3/2}$	7.877E+07	6.806E+07		7.40E+07 [d C]	7.10E+07 [A]
$3s^2\ 4d\ ^2D_{3/2\ a}$	$3s^2\ 3p\ ^2P^o_{1/2}$	1.722E+07			1.92E+07 [f C+]	
					2.30E+07 [d C]	
	$3s^2\ 3p\ ^2P^o_{3/2}$	3.293E+06		5.99E+06	3.80E+06 [f C+]	
					4.40E+06 [d C]	
$3s^2\ 4d\ ^2D_{5/2\ a}$	$3s^2\ 3p\ ^2P^o_{3/2}$	2.010E+07		3.60E+07	2.30E+07 [f]	
					2.80E+07 [d C]	
$3s^2\ 4d\ ^2D_{3/2\ b}$	$3s^2\ 3p\ ^2P^o_{1/2}$	7.128E+07		7.61E+07	7.20E+07 [d C]	
					5.26E+07 [f]	
	$3s^2\ 3p\ ^2P^o_{3/2}$	1.386E+07		1.51E+07	1.40E+07 [d C]	
					1.05E+07 [f A]	
$3s^2\ 4d\ ^2D_{5/2\ b}$	$3s^2\ 3p\ ^2P^o_{3/2}$	8.412E+07		9.07E+07	8.60E+07 [d C]	
					6.31E+07 [f]	
$3s^2\ 5d\ ^2D_{3/2}$	$3s^2\ 3p\ ^2P^o_{1/2}$	8.204E+07			6.60E+07 [d C]	
					5.76E+07 [f]	
	$3s^2\ 3p\ ^2P^o_{3/2}$	1.596E+07		1.26E+07	1.30E+07 [d C]	
					1.15E+07 [f]	
$3s^2\ 5d\ ^2D_{5/2}$	$3s^2\ 3p\ ^2P^o_{3/2}$	9.706E+07		7.58E+07	7.90E+07 [d C]	
					6.91E+07 [f]	

Notes. The present values from the RCI calculations are given in Col. 3. In the next two columns, theoretical values from former MCHF-BP and close coupling (CC) calculations are displayed. The CC values complement the MCHF-BP values, which are restricted to transitions between levels in the lower part of the Al I spectrum. All theoretical transition rates are presented in length form. The last two columns contain the results from experimental observations. The experimental results go along with a letter grade, whenever accessible, which indicates the accuracy level. The correspondence between the accuracy ratings and the estimated relative uncertainty of the experimental results is $A \leq 3\%$, $B \leq 10\%$, $C+ \leq 15\%$, $C \leq 25\%$, $D+ \leq 30\%$, $D \leq 50\%$.

References. [a]Present calculations; [b]Froese Fischer et al. (2006); [c]Mendoza et al. (1995); [d]Wiese & Martin (1980); [e]Buurman et al. (1986); [f]Davidson et al. (1990); [g]Vujnović et al. (2002).

of view, although they are less likely to be observed. The computation of transition properties in the system of Al I is overall far from trivial due to the extreme mixing of the $3s^2nd\ ^2D$ series. Transitions involving any ^2D state as upper or lower level appear to be associated with large uncertainties. However, the predicted energy separations are in excellent agreement with observations, meaning that the LS-composition of the $3s^2nd\ ^2D$ states is well described. This should serve as a quality indicator of the computed transition data.

Transition rates A_{obs} evaluated from experimental measurements are compared with the current RCI theoretical values (see Table 5) and with values from the MCHF-BP calculations by Froese Fischer et al. (2006) and the close coupling (CC) calculations by Mendoza et al. (1995). Even though the measurements by Davidson et al. (1990) are more recent than the compiled values by Wiese & Martin (1980), the latter seem to be in better overall agreement with the transition rates predicted by the RCI calculations. In all cases the A_{RCI} values fall into the range of the estimated uncertainties by Wiese & Martin (1980). The only exceptions are the transitions with $3s^24d\ ^2D_{3/2,5/2\ a}$ as upper levels, for which the A_{RCI} values agree better with the ones suggested by Davidson et al. (1990). Although the evaluated transition rates by Vujnović et al. (2002) slightly differ from the other observations, they are still in fairly good agreement with the present work. For the $3s^24p\ ^2P^o_{3/2} \rightarrow 3s^24s\ ^2S_{1/2}$ and $3s^23d\ ^2D_{5/2} \rightarrow 3s^23p\ ^2P^o_{3/2}$ transitions, the values by Vujnović et al. (2002) are better reproduced by the $A_{MCHF-BP}$ results, yet not enough correlation is included in the calculations by Froese Fischer et al. (2006) and the transition rates predicted by the RCI calculations should be considered more accurate. Whenever values from the close coupling (CC) calculations are presented to complement the MCHF-BP

Table 6. Comparison between computed and observed lifetimes τ in seconds for the 26 lowest excited states in Al I.

			RCI[a]		MCHF-BP[b]	Expt.[c,d,e]
Pos.	Conf.	$LS\,J$	τ_l	τ_v	τ_l	$\tau_{\rm obs}$
1	$3s^2\,4s$	$^2S_{1/2}$	6.734E-09	6.745E-09	6.558E-09	6.85(6)E-09[c]
2	$3s\,3p^2$	$^4P_{1/2}$	1.652E-03	1.182E-03	4.950E-03	
3		$^4P_{3/2}$	6.702E-03	6.911E-03	13.24E-03	
4		$^4P_{5/2}$	2.604E-03	3.681E-03	9.486E-03	
5	$3s^2\,3d$	$^2D_{3/2}$	1.272E-08	1.372E-08	1.472E-08	1.40(2)E-08[c]
6		$^2D_{5/2}$	1.270E-08	1.371E-08	1.469E-08	1.40(2)E-08[c]
7	$3s^2\,4p$	$^2P^o_{1/2}$	6.329E-08	6.357E-08	6.621E-08	6.05(9)E-08[e]
8		$^2P^o_{3/2}$	6.300E-08	6.328E-08	6.590E-08	6.5 (2) E-08[e]
9	$3s^2\,5s$	$^2S_{1/2}$	2.019E-08	2.027E-08		1.98(5)E-08[c]
10	$3s^2\,4d$	$^2D_{3/2\,a}$	3.117E-08	2.919E-08		2.95(7)E-08[c]
11		$^2D_{5/2\,a}$	3.158E-08	2.953E-08		2.95(7)E-08[c]
12	$3s^2\,5p$	$^2P^o_{1/2}$	2.448E-07	2.532E-07		2.75(8)E-07[c]
13		$^2P^o_{3/2}$	2.429E-07	2.512E-07		2.75(8)E-07[c]
14	$3s^2\,4f$	$^2F^o_{5/2}$	6.041E-08	6.162E-08		
15		$^2F^o_{7/2}$	6.041E-08	6.160E-08		
16	$3s^2\,6s$	$^2S_{1/2}$	4.812E-08	4.885E-08		
17	$3s^2\,4d$	$^2D_{3/2\,b}$	1.136E-08	1.083E-08		1.32(3)E-08[d]
18		$^2D_{5/2\,b}$	1.150E-08	1.093E-08		1.32(3)E-08[d]
19	$3s^2\,6p$	$^2P^o_{1/2}$	4.886E-07	6.952E-07		
20		$^2P^o_{3/2}$	4.845E-07	6.882E-07		
21	$3s^2\,5f$	$^2F^o_{7/2}$	1.176E-07	1.172E-07		
22		$^2F^o_{5/2}$	1.175E-07	1.172E-07		
23	$3s^2\,5g$	$^2G_{7/2}$	2.301E-07	2.315E-07		
24		$^2G_{9/2}$	2.301E-07	2.315E-07		
25	$3s^2\,5d$	$^2D_{3/2}$	1.011E-08	9.855E-09		14.0(2)E-09[d]
26		$^2D_{5/2}$	1.020E-08	9.921E-09		14.0(2)E-09[d]

Notes. For the current RCI calculations both length τ_l and velocity τ_v forms are displayed. In Col. 6, the predicted lifetimes from MCHF-BP calculations are given in length form. The last column contains available lifetimes from experimental measurements together with their uncertainties.

References. [(a)]Present calculations; [(b)]Froese Fischer et al. (2006); [(c)]Buurman et al. (1986); [(d)]Davidson et al. (1990); [(e)]Buurman & Dönszelmann (1990).

results, the $A_{\rm RCI}$ values appear to be in better agreement with the experimental values. Exceptionally, for the $3s^25d\ ^2D_{3/2,5/2} \rightarrow 3s^23p\ ^2P^o_{3/2}$ transitions, the $A_{\rm CC}$ values by Mendoza et al. (1995) approach the corresponding experimental values more closely. Even so, the $A_{\rm RCI}$ values are still within the given experimental uncertainties. One should bear in mind that according to the estimation of uncertainties by Kelleher & Podobedova (2008b) the $A_{\rm CC}$ values carry relative uncertainties up to 30%. On the contrary, based on the agreement between length and velocity forms, the estimated uncertainties of the current RCI calculations for the above-mentioned transitions are of the order of 3% percent. Therefore, we suggest that the current transition rates are used as a reference.

From the computed E1 transition rates, the lifetimes of the excited states are estimated. Transition data for transitions other than E1 have not been computed in this work since the contributions to the lifetimes from magnetic or higher electric multipoles are expected to be negligible. In Table 6 the currently computed lifetimes are given in both length τ_l and velocity τ_v forms. The agreement between these two forms probes the level of accuracy of the calculations. Because of the poor agreement between the length and velocity form of the quartet $3s3p^2\ ^4P$ and doublet $3s^26p\ ^2P$ states, the average relative difference appears overall to be ∼8%. The differences between the length and velocity gauges of the quartet $3s3p^2\ ^4P$ states are of the order of 25% on average. These long-lived states are associated with weak transitions and computations involving such transitions are, as mentioned above, rather challenging. In addition, we note that the relative differences corresponding to the $3s^26p\ ^2P$ states exceed 40%. As the computations involve Rydberg series, states between the lowest and highest computed levels might not occupy the same region in space. Nevertheless, these states are part of the same multireference (MR). The highest computed levels correspond to configurations with orbitals up to $n = 6$, such as $3s^26p$. To obtain a better description of these levels it is probably necessary to perform initial calculations including in the MR $3s^2$nl configurations with $n = 7$ and perhaps even $n = 8$. This would lead to a more complete and balanced orbital set (Pehlivan Rhodin et al. 2017). When excluding the above-mentioned states, the mean relative difference between τ_l and τ_v is ∼3%, which is satisfactory.

In Table 6, the lifetimes from the current RCI calculations are compared with results from the MCHF-BP calculations by Froese Fischer et al. (2006) and observations. Only for the $3s^24p\ ^2P$ state are separated observed values of the lifetimes given for the two fine-structure components. For the rest of the

measured lifetimes, a single value for the two fine-structure levels is provided. As can be seen, the overall agreement between the theoretical and the measured lifetimes τ_{obs} is rather good. However, the measured lifetimes are better represented by the current RCI results than by the MCHF-BP values. For most of the states, the differences between the RCI and MCHF-BP values are small, except for the levels of the quartet $3s3p^2\ ^4P$ state. For these long-lived states, no experimental lifetimes exist for comparison.

4.2. Al II

In Table A.1, the computed excitation energies, based on VV correlation, are given as a function of the increasing active set of orbitals. When adding the $n = 12$ correlation layer, the values for all computed energy separations have converged. The agreement with the NIST observed energies (Kramida et al. 2018) is, at this point, fairly good. The mean relative difference between theory and experiment is of the order of 1.2%. However, when accounting for CV correlation, the agreement with the observed values is significantly improved, resulting in a mean relative difference being less than 0.2%. Accounting for CV effects also results in a labelling of the eigenstates that matches observations. For instance, when only VV correlation is taken into account, the ^{3}F triplet with the highest energy is labelled as a 3s6f level. After taking CV effects into account, the eigenstates of this triplet are assigned the 3p3d configuration, now the one with the largest expansion coefficient, which agrees with observations. There are no experimental excitation energies for the singlet and triplet $3s6h\ ^{1,3}H$ terms. In the last column of Table A.1, the differences ΔE between computed and observed energies are displayed. All ΔE values maintain the same sign, being negative.

In Table 3, a comparison between the present computed excitation energies and those from the MCHF-BP calculations by Froese Fischer et al. (2006) is also performed for Al II. The latter spectrum calculations are extended up to levels corresponding to the singlet $3p^2\ ^1S$ state and all types of correlation, i.e. VV, CV, and CC, were accounted for. Both computational approaches are highly accurate, yet the majority of the levels is better represented by the current RCI results. The average relative difference for the RCI values is ∼0.2% and for the MCHF-BP ∼0.3%. Moreover, the $\Delta E_{\mathrm{MCHF-BP}}$ values do not always maintain the same sign, while the ΔE_{RCI} values do. Hence, in general, the MCHF-BP calculations do not predict the transition energies as precisely as the present RCI method.

For all computed E1 transitions in Al II, transition data tables can also be found at the CDS. In Table 4, a statistical analysis of the uncertainties to the computed transition rates A_{RCI} is performed in a similar way to that for Al I. The transitions are also arranged here in four groups. Following the conclusions by Pehlivan Rhodin et al. (2017) and Pehlivan Rhodin (2018), the transitions involving any of the $3s7p\ ^{1,3}P$ states have been excluded from this analysis. The discrepancies between the length and velocity forms for transitions including the $3s7p\ ^{1,3}P$ states are consistently large, and thus the computed transition rates are not trustworthy. We note that overall the average uncertainty, as well as the value that includes 75% of the data, appear to be smaller, for each group of transitions, than the predicted values in Al I. Nevertheless, the maximum values of the uncertainties for the last two groups are larger in comparison to Al I. This is due to some transitions involving $3p3d\ ^3F$ as the upper level. The strong mixing between the $3p3d\ ^3F$ and the $3s6f\ ^3F$ levels results in strong cancellation effects. Such effects often hamper the accuracy of the computed transition data and result in large discrepancies between the length and velocity forms.

In Table 7, current RCI theoretical transition rates are compared with the values from the MCHF-BP calculations by Froese Fischer et al. (2006) and, whenever available, results from the B-spline configuration interaction (BSCI) calculations by Chang & Fang (1995). For the majority of the transitions, there is an excellent agreement between the RCI and MCHF-BP values with the relative difference being less than 1%. Some of the largest discrepancies are observed for the $3s3d, 3p^2\ ^1D \rightarrow 3s3p\ ^{1,3}P^o$ transitions. According to Froese Fischer et al. (2006), correlation is extremely important for transitions from such ^{1}D states. In the MCHF-BP calculations, all three types of correlation, i.e. VV, CV, and CC, have been accounted for; however, the CSF expansions obtained from SD-substitutions are not as large as in the present calculations and the *LS*-composition of the configurations might not be predicted as accurately. Hence, the evaluation of line strengths for transitions involving ^{1}D states and in turn the computation of transition rates involving these states will be affected. Computed transition rates using the BSCI approach are provided for transitions that involve only singlet states. The BSCI calculations do not account for the relativistic interaction and no separate values are given for the different fine-structure components of triplet states. For the $3p^2\ ^1D \rightarrow 3s3p\ ^1P^o$ transition, the discrepancy between the RCI and BSCI values is also quite large. On the other hand, for the $3s3d\ ^1D \rightarrow 3s3p\ ^1P^o$ transition, the BSCI result is in perfect agreement with the present A_{RCI} value. The agreement between the current RCI and BSCI transition rates exhibits a broad variation. The advantage of the BSCI approach is that it takes into account the effect of the positive-energy continuum orbitals in an explicit manner. Nevertheless, the parametrized model potential that is being used in the work by Chang & Fang (1995) is not sufficient to describe states that are strongly mixed. Finally, we note the discrepancy for the $3s4p\ ^1P^o \rightarrow 3s^2\ ^1S_0$ transition, which is quite large between the RCI and MCHF-BP values and inexplicably large between the RCI and BSCI values.

In singly ionized aluminium, measurements of transition properties are available only for a few transitions. In Table 7, the available experimental results are compared with the theoretical results from the current RCI calculations, and with the former calculations by Froese Fischer et al. (2006) and Chang & Fang (1995). Transition rates have been experimentally observed for the $3s3p\ ^{1,3}P^o_1 \rightarrow 3s^2\ ^1S_0$ transitions in the works by Kernahan et al. (1979), Smith (1970), Berry et al. (1970) and Head et al. (1976), and by Träbert et al. (1999) and Johnson et al. (1986), respectively. In Table 7, the average value of these works is displayed. The agreement with the current RCI results is fairly good. Nonetheless, the averaged A_{obs} by Träbert et al. (1999) and Johnson et al. (1986) is in better agreement with the value by Froese Fischer et al. (2006). Additionally, Vujnović et al. (2002) provided experimental transition rates for the $3p^2\ ^1D_2 \rightarrow 3s3p\ ^1P_1$ and $3p^2\ ^1D_2 \rightarrow 3s3p\ ^3P_{1,2}$ transitions by measuring relative intensities of spectral lines. These experimental results, however, differ from the theoretical values.

In the last portion of Table 7, current rates for transitions between states with higher energies are compared with the results from the close coupling (CC) calculations by Butler et al. (1993) and the early results from the configuration interaction (CI) calculations by Chang & Wang (1987). The results from the latter two calculations are found to be in very good agreement. Furthermore, the agreement between the RCI results and those from the CC and CI calculations is also very good

Table 7. Comparison between computed and observed transition rates A in s^{-1} for selected transitions in Al II.

Upper	Lower	A_{RCI} [a]	A_{theor} [b,c]	A_{theor} [e,f]	A_{obs} [d,h,g]
$3s3p\ ^3P^o_1$	$3s^2\ ^1S_0$	3.054E+03	3.277E+03[b]		3.30E+03[h]
$3s3p\ ^1P^o_1$	$3s^2\ ^1S_0$	1.404E+09	1.400E+09[b]	1.486E+09[f]	1.45E+09[g]
$3s4s\ ^3S_1$	$3s3p\ ^3P^o_0$	8.612E+07	8.572E+07[b]		
	$3s3p\ ^3P^o_1$	2.555E+08	2.547E+08[b]		
	$3s3p\ ^3P^o_2$	4.173E+08	4.162E+08[b]		
$3s4s\ ^1S_0$	$3s3p\ ^1P^o_1$	3.422E+08	3.455E+08[b]	3.408E+08[f]	
$3p^2\ ^1D_2$	$3s3p\ ^1P^o_1$	2.523E+05	3.804E+05[b]	3.980E+05[f]	1.84E+04[d]
	$3s3p\ ^3P^o_1$	1.790E+04	2.016E+04[b]		0.19E+04[d]
	$3s3p\ ^3P^o_2$	2.827E+04	3.141E+04[b]		0.30E+04[d]
$3p^2\ ^3P_0$	$3s3p\ ^3P^o_1$	1.236E+09	1.235E+09[b]		
$3p^2\ ^3P_1$	$3s3p\ ^3P^o_0$	4.148E+08	4.144E+08[b]		
	$3s3p\ ^3P^o_1$	3.058E+08	3.062E+08[b]		
	$3s3p\ ^3P^o_2$	5.170E+08	5.167E+08[b]		
$3p^2\ ^3P_2$	$3s3p\ ^3P^o_1$	3.145E+08	3.144E+08[b]		
	$3s3p\ ^3P^o_2$	9.264E+08	9.272E+08[b]		
$3p^2\ ^1S_0$	$3s3p\ ^1P^o_1$	1.020E+09	6.738E+08[b]		
	$3s3p\ ^3P^o_1$	5.021E+08	3.399E+07[b]		
$3s3d\ ^3D_2$	$3s3p\ ^3P^o_1$	8.977E+08	9.072E+08[b]		
	$3s3p\ ^3P^o_2$	3.019E+08	3.046E+08[b]		
$3s3d\ ^3D_3$	$3s3p\ ^3P^o_2$	1.197E+09	1.208E+09[b]		
$3s3d\ ^1D_2$	$3s3p\ ^1P^o_1$	1.388E+09	1.429E+09[b]	1.388E+09[f]	
$3s4p\ ^3P^o_0$	$3s4s\ ^3S_1$	5.639E+07	5.705E+07[b]		
	$3s3d\ ^3D_1$	1.556E+07	1.520E+07[b]		
$3s4p\ ^3P^o_1$	$3s4s\ ^3S_1$	5.649E+07	5.724E+07[b]		
	$3s3d\ ^3D_1$	3.905E+06	3.816E+06[b]		
	$3s3d\ ^3D_2$	1.172E+07	1.146E+07[b]		
$3s4p\ ^3P^o_2$	$3s4s\ ^3S_1$	5.683E+07	5.762E+07[b]		
	$3s3d\ ^3D_1$	1.568E+05	1.541E+05[b]		
	$3s3d\ ^3D_2$	2.361E+06	2.312E+06[b]		
	$3s3d\ ^3D_3$	1.319E+07	1.294E+07[b]		
$3s4p\ ^1P^o_1$	$3s^2\ ^1S_0$	1.527E+06	0.981E+06[b]	5.079E+06[f]	
	$3p^2\ ^1D_2$	5.835E+07	5.897E+07[b]	6.307E+07[f]	
	$3s4s\ ^1S_0$	3.109E+07	2.965E+07[b]	3.111E+07[f]	
$3p3d\ ^3F^o_2$	$3s3d\ ^3D_1$	2.956E+08	2.07E+08[c]	2.14E+08[e]	
$3p3d\ ^3F^o_3$	$3s3d\ ^3D_2$	3.174E+08	2.19E+08[c]	2.25E+08[e]	
$3p3d\ ^3F^o_4$	$3s3d\ ^3D_3$	3.794E+08	2.47E+08[c]	2.54E+08[e]	
$3s4f\ ^3F^o_2$	$3s3d\ ^3D_1$	1.981E+08	1.97E+08[c]	1.98E+08[e]	
$3s4f\ ^3F^o_3$	$3s3d\ ^3D_2$	2.096E+08	2.09E+08[c]	2.07E+08[e]	
$3s4f\ ^3F^o_4$	$3s3d\ ^3D_3$	2.360E+08	2.35E+08[c]	2.33E+08[e]	
$3s5f\ ^3F^o_2$	$3s3d\ ^3D_1$	2.801E+07	2.40E+07[c]	2.50E+07[e]	
$3s5f\ ^3F^o_4$	$3s3d\ ^3D_3$	3.438E+07	2.85E+07[c]	2.90E+07[e]	
$3s6f\ ^3F^o_2$	$3s3d\ ^3D_1$	1.957E+07	2.90E+07[c]	3.10E+07[e]	
	$3s4d\ ^3D_1$	1.116E+07	1.07E+07[c]	1.00E+07[e]	
$3s6f\ ^3F^o_3$	$3s3d\ ^3D_2$	1.910E+07	3.07E+07[c]	3.30E+07[e]	
	$3s4d\ ^3D_2$	1.200E+07	1.14E+07[c]	1.10E+07[e]	
$3s6f\ ^3F^o_4$	$3s3d\ ^3D_3$	1.920E+07	3.46E+07[c]	3.70E+07[e]	
	$3s4d\ ^3D_3$	1.367E+07	1.28E+07[c]	1.20E+07[e]	

Notes. The present values from the RCI calculations are given in Col. 3. In the next two columns, theoretical values from former MCHF-BP, close coupling (CC), configuration interaction (CI), and B-spline configuration interaction (BSCI) calculations are given. The last column contains the results from experimental observations. All theoretical transition rates are presented in length form.

References. [(a)]Present calculations; [(b)]Froese Fischer et al. (2006); [(c)]Butler et al. (1993); [(d)]Vujnović et al. (2002); [(e)]Chang & Wang (1987); [(f)]Chang & Fang (1995); [(g)]Kernahan et al. (1979), Smith (1970), Berry et al. (1970), Head et al. (1976); [(h)]Träbert et al. (1999), Johnson et al. (1986).

for the $3s4f\ ^3F \rightarrow 3s3d\ ^3D$ transitions and fairly good for the $3s5f\ ^3F \rightarrow 3s3d\ ^3D$ transitions. On the other hand, for the 3p3d, $3s6f\ ^3F \rightarrow 3s3d\ ^3D$ transitions, the observed discrepancy between the current RCI values and those from the two previous calculations is substantial. This outcome indicates that the calculations by Butler et al. (1993) and Chang & Wang (1987) are insufficient to properly account for correlation and further emphasizes the quality of the present work.

In the same way as for Al I, the lifetimes of Al II excited states were also estimated based on the computed E1 transitions. In Table A.2, both length τ_l and velocity τ_v forms of the currently computed lifetimes are displayed. As already mentioned, the agreement between these two forms serves as an indication of the quality of the results. The average relative difference between the two forms is ∼2%. The largest discrepancies are observed between the length and velocity gauges of the singlet $3p^2\ ^1D$ state, and between the singlet and triplet $3s7p\ ^{1,3}P$ states. The highest computed levels in the calculations of Al II correspond to configuration states with orbitals up to $n = 7$, such as 3s7p. Similarly to the conclusions for the lifetimes of Al I, better agreement between the length and velocity forms of the $3s7p\ ^{1,3}P$ states could probably be obtained by including 3snl configurations with $n > 7$ in the MR.

In Table A.2, the lifetimes from the current RCI calculations are compared with results from previous MCHF-BP and BSCI calculations by Froese Fischer et al. (2006) and Chang & Fang (1995), respectively. Except for the lifetimes of the triplet $3s3p\ ^3P^o_1$ and singlet $3p^2\ ^1D_2$ states, the agreement between the RCI and MCHF-BP calculations is very good. Furthermore, the overall agreement between the RCI and BSCI calculations is sufficiently good. Despite the poor agreement between the RCI and BSCI values for the $3p^2\ ^1D_2$ and $3s7p\ ^{1,3}P$ states, for the rest of the states the discrepancies are small. The BSCI results are more extended. However, no separate values are provided for the different *LS J*-components of the triplet states and the average lifetime is presented for them instead.

In Table A.2, the theoretical lifetimes are also compared with available measurements. The measured lifetime of the $3s3p\ ^3P^o_1$ state by Träbert et al. (1999) and Johnson et al. (1986) agrees remarkably well with the calculated value by Froese Fischer et al. (2006). The agreement with the current results is fairly good too. The lifetime of the $3s3p\ ^1P^o_1$ state measured by Kernahan et al. (1979), Head et al. (1976), Berry et al. (1970), and Smith (1970) is well represented by all theoretical values. On the other hand, the results from the measurements of the 3snf ^3F states by Andersen et al. (1971) differ substantially from the theoretical RCI values. For the 3snf ^3F Rydberg series, only theoretical lifetimes using the current MCDHF and RCI approach are available. Given the large uncertainties associated with early beam-foil measurements, the discrepancies between theoretical and experimental values are in some way expected. The only exception is the lifetime of the $3s5f\ ^3F$ state, which is in rather good agreement with the RCI values. In the experiments by Andersen et al. (1971) the different fine-structure components have not been separated and a single value is provided for all three different *LS J*-levels.

5. Summary and conclusions

In the present work, updated and extended transition data and lifetimes are made available for both Al I and Al II. The computations of transition properties in these two systems are challenging mainly due to the strong two-electron interaction between the $3s3d\ ^1D$ and $3p^2\ ^1D$ states, which dominates the lowest part of their spectra. Thus, some of the states are strongly mixed and highly correlated wave functions are needed to accurately predict their *LS*-composition. We are confident that in this work enough correlation has been included to affirm the reliability of the results. The predicted excitation energies are in excellent agreement with the experimental data provided by the NIST database, which is a good indicator of the quality of the produced transition data and lifetimes.

We have performed an extensive comparison of the computed transition rates and lifetimes with the most recent theoretical and experimental results. There is a significant improvement in accuracy, in particular for the more complex system of neutral Al I. The computed lifetimes of Al I are in very good agreement with the measured lifetimes in high-precision laser spectroscopy experiments. The same holds for the measured lifetimes of Al II in ion storage rings. The present calculations are extended to higher energies and many of the computed transitions fall in the infrared spectral region. The new generation of telescopes are designed for this region and these transition data are of high importance. The objective of this work is to make available atomic data that could be used to improve the interpretation of abundances in stars. Lists of trustworthy elemental abundances will permit the tracing of stellar evolution, as well as the formation and chemical evolution of the Milky Way.

The agreement between the length and velocity gauges of the transition operator serves as a criterion for the quality of the transition data and for the lifetimes. For most of the strong transitions in both Al I and Al II, the agreement between the two gauges is very good. For transitions involving states with the highest n quantum number for the s and p symmetries, we observe that the agreement between the length and velocity forms is not as good. This becomes more evident when estimating lifetimes of excited levels that are associated with those transitions.

Acknowledgements. The authors have been supported by the Swedish Research Council (VR) under contract 2015-04842. The authors acknowledge H. Hartman, Malmö University, and H. Jönsson, Lund University, for discussions.

References

Adibekyan, V. Z., Sousa, S. G., Santos, N. C., et al. 2012, A&A, 545, A32
Andersen, T., Roberts, J. R., & Sørensen, G. 1971, Phys. Scr., 4, 52
Bensby, T., Feltzing, S., & Oey, M. S. 2014, A&A, 562, A71
Berry, H. G., Bromander, J., & Buchta, R. 1970, Phys. Scr., 1, 181
Butler, K., Mendoza, C., & Zeippen, C. 1993, J. Phys. B, 26, 4409
Buurman, E., & Dönszelmann, A. 1990, A&A, 227, 289
Buurman, E., Dönszelmann, A., Hansen, J. E., & Snoek, C. 1986, A&A, 164, 224
Carretta, E., Bragaglia, A., Gratton, R. G., et al. 2010, A&A, 516, A55
Chang, T. N., & Fang, T. K. 1995, Phys. Rev. A, 52, 2638
Chang, T. N., & Wang, R. 1987, Phys. Rev. A, 36, 3535
Clayton, D. D. 2003, Handbook of Isotopes in the Cosmos: Hydrogen to Gallium (Cambridge: Cambridge University Press)
Davidson, M. D., Volten, H., & Dönszelmann, A. 1990, A&A, 238, 452
Dyall, K. G., Grant, I. P., Johnson, C., Parpia, F. A., & Plummer, E. P. 1989, Comput. Phys. Commun., 55, 425
Ekman, J., Godefroid, M., & Hartman, H. 2014, Atoms, 2, 215
Froese Fischer, C. 2009, Phys. Scr., T134, 014019
Froese Fischer, C., Tachiev, G., & Irimia, A. 2006, At. Data Nucl. Data Tables, 92, 607
Froese Fischer, C., Godefroid, M., Brage, T., Jönsson, P., & Gaigalas, G. 2016, J. Phys. B: At. Mol. Opt. Phys., 49, 182004
Gaigalas, G., Rudzikas, Z., & Froese Fischer, C. 1997, J. Phys. B: At. Mol. Opt. Phys., 30, 3747
Gaigalas, G., Fritzsche, S., & Grant, I. P. 2001, Comput. Phys. Commun., 139, 263
Gaigalas, G., Zalandauskas, T., & Rudzikas, Z. 2003, At. Data Nucl. Data Tables, 84, 99
Gaigalas, G., Zalandauskas, T., & Fritzsche, S. 2004, Comput. Phys. Commun., 157, 239
Gaigalas, G., Froese Fischer, C., Rynkun, P., & Jönsson, P. 2017, Atoms, 5, 6
Gehren, T., Liang, Y. C., Shi, J. R., Zhang, H. W., & Zhao, G. 2004, A&A, 413, 1045
Gehren, T., Shi, J. R., Zhang, H. W., Zhao, G., & Korn, A. J. 2006, A&A, 451, 1065
Grant, I. P. 1974, J. Phys. B, 7, 1458

Grant, I. P. 2007, Relativistic Quantum Theory of Atoms and Molecules (New York: Springer)
Head, M. E. M., Head, C. E., & Lawrence, J. N. 1976, in Atomic Structure and Lifetimes, eds. F. A. Sellin, & D. J. Pegg (NY: Plenum), 147
Hibbert, A. 1989, Phys. Scr., 39, 574
Jönsson, G., & Lundberg, H. 1983, Z. Phys. A, 313, 151
Johnson, B. C., Smith, P. L., & Parkinson, W. H. 1986, ApJ, 308, 1013
Jönsson, G., Kröll, S., Persson, A., & Svanberg, S. 1984, Phys. Rev. A, 30, 2429
Jönsson, P., Gaigalas, G., Bieroń, J., Froese Fischer, C., & Grant, I. P. 2013, Phys. Commun., 184, 2197
Kelleher, D. E., & Podobedova, L. I. 2008a, J. Phys. Chem. Ref. Data, 37, 709
Kelleher, D. E., & Podobedova, L. I. 2008b, J. Phys. Chem. Ref. Data, 37, 267
Kernahan, J. A., Pinnington, E. H., O'Neill, J. A. M., Brooks, R. L., & Donnely, K. E. 1979, Phys. Scrip., 19, 267
Kramida, A., Ralchenko, Y. u., & Reader, J. NIST ASD Team 2018, NIST Atomic Spectra Database, ver. 5.5.3 (Online), available: https://physics.nist.gov/asd (2018, March 15), National Institute of Standards and Technology, Gaithersburg, MD
Lin, C. D. 1974, ApJ, 187, 385
McKenzie, B. J., Grant, I. P., & Norrington, P. H. 1980, Comput. Phys. Commun., 21, 233
Mendoza, C., Eissner, W., Le Dourneuf, M., & Zeippen, C. J. 1995, J. Phys. B, 28, 3485
Mishenina, T. V., Soubiran, C., Bienaymé, O., et al. 2008, A&A, 489, 923
Nordlander, T., & Lind, K. 2017, A&A, 607, A75
Olsen, J., Roos, B. O., Jorgensen, P., & Jensen, H. J. A. a. 1988, J. Chem. Phys., 89, 2185
Pehlivan Rhodin, A., Hartman, H., Nilsson, H., & Jönsson, P. 2017, A&A, 598, A102
Pehlivan Rhodin, A. 2018, Ph. D. Thesis, Lund Observatory
Reddy, B. E., Lambert, D. L., & Allende Prieto, C. 2006, MNRAS, 367, 1329
Smiljanic, R., Korn, A. J., Bergemann, M., Frasca, A., et al. 2014, A&A, 570, A122
Smiljanic, R., Romano, D., Bragaglia, A., Donati, P., et al. 2016, A&A, 589, A115
Smith, W. H. 1970, NIM, 90, 115
Sturesson, L., Jönsson, P., & Fischer, C. F. 2007, Comput. Phys. Commun., 177, 539
Tayal, S. S., & Hibbert, A. 1984, J. Phys. B, 17, 3835
Taylor, P. R. C. W., Bauschlicher, J., & Langhoff, S. 1988, J. Phys. B, 21, L333
Theodosiou, C. E. 1992, Phys. Rev. A, 45, 7756
Trefftz, E. 1988, J. Phys. B: At. Mol. Opt. Phys., 21, 1761
Träbert, E., Wolf, A., & Linkemann, J. 1999, J. Phys. B, 32, 637
Vujnović, V., Blagoev, K., Fürböck, C., Neger, T., & Jäger, H. 2002, A&A, 338, 704
Weiss, A. W. 1974, Phys. Rev., 9, 1524
Wiese, W. L., Smith, M. W., & Miles, B. M. 1969, NSRDS-NBS, 22, 47
Wiese, W. L., & Martin, G. A. 1980, in Transition Probabilities, Part II, Vol. Natl. Stand. Ref. Data System., (Washington DC), Natl. Bur. Std., 68

Appendix A: Additional tables

Table A.1. Computed excitation energies in cm^{-1} for the 78 lowest states in Al II.

			VV								
Pos.	Conf.	LSJ	$n = 8$	$n = 9$	$n = 10$	$n = 11$	$n = 12$	$n = 13$	CV	E_{obs}[a]	ΔE
1	$3s^2$	$^1S_0$	0	0	0	0	0	0	0	0	0
2	3s 3p	$^3P^o_0$	36 227	36 280	36 298	36 318	36 332	36 335	37 445	37 393	−52
3		$^3P^o_1$	36 286	36 339	36 357	36 377	36 391	36 394	37 503	37 454	−49
4		$^3P^o_2$	36 405	36 459	36 477	36 496	36 511	36 514	37 626	37 578	−48
5		$^1P^o_1$	59 810	59 698	59 617	59 619	59 606	59 602	59 982	59 852	−130
6	$3p^2$	$^1D_2$	83 542	83 596	83 620	83 641	83 657	83 660	85 692	85 481	−211
7	3s 4s	$^3S_1$	89 965	90 028	90 059	90 082	90 099	90 102	91 425	91 275	−150
8	$3p^2$	$^3P_0$	92 679	92 709	92 716	92 736	92 750	92 752	94 211	94 085	−126
9		$^3P_1$	92 739	92 769	92 776	92 795	92 809	92 812	94 264	94 147	−117
10		$^3P_2$	92 855	92 885	92 892	92 912	92 926	92 928	94 375	94 269	−106
11	3s 4s	$^1S_0$	94 003	94 057	94 084	94 101	94 111	94 114	95 543	95 351	−192
12	3s 3d	$^3D_2$	94 262	94 243	94 241	94 262	94 278	94 280	95 791	95 549	−242
13		$^3D_1$	94 261	94 243	94 242	94 263	94 279	94 281	95 794	95 551	−243
14		$^3D_3$	94 263	94 242	94 239	94 261	94 276	94 279	95 804	95 551	−253
15	3s 4p	$^3P^o_0$	103 935	104 003	104 030	104 053	104 070	104 073	105 582	105 428	−154
16		$^3P^o_1$	103 948	104 017	104 044	104 067	104 084	104 087	105 594	105 442	−152
17		$^3P^o_2$	103 976	104 045	104 073	104 095	104 112	104 115	105 623	105 471	−152
18		$^1P^o_1$	105 597	105 643	105 655	105 673	105 683	105 685	107 132	106 921	−211
19	3s 3d	$^1D_2$	109 010	108 919	108 897	108 910	108 918	108 918	110 330	110 090	−240
20	$3p^2$	$^1S_0$	111 100	110 804	110 659	110 643	110 618	110 608	112 086	111 637	−449
21	3s 5s	$^3S_1$	118 564	118 632	118 661	118 685	118 702	118 705	120 259	120 093	−166
22		$^1S_0$	119 807	119 878	119 908	119 931	119 946	119 948	121 544	121 367	−177
23	3s 4d	$^3D_2$	120 013	120 034	120 045	120 068	120 085	120 088	121 684	121 484	−200
24		$^3D_1$	120 013	120 034	120 046	120 068	120 085	120 088	121 685	121 484	−201
25		$^3D_3$	120 014	120 034	120 045	120 068	120 084	120 087	121 688	121 484	−204
26	3s 4f	$^3F^o_2$	121 657	121 739	121 772	121 797	121 815	121 818	123 606	123 418	−188
27		$^3F^o_3$	121 659	121 742	121 775	121 799	121 817	121 820	123 608	123 420	−188
28		$^3F^o_4$	121 663	121 745	121 778	121 802	121 820	121 824	123 612	123 423	−189
29		$^1F^o_3$	121 735	121 818	121 852	121 876	121 894	121 898	123 657	123 471	−186
30	3s 4d	$^1D_2$	123 606	123 489	123 461	123 473	123 482	123 483	125 049	124 794	−255
31	3s 5p	$^3P^o_0$	124 108	124 185	124 212	124 236	124 254	124 257	125 869	125 703	−166
32		$^3P^o_1$	124 114	124 190	124 218	124 242	124 259	124 262	125 874	125 709	−165
33		$^3P^o_2$	124 126	124 203	124 231	124 254	124 272	124 275	125 887	125 722	−165
34		$^1P^o_1$	124 302	124 375	124 401	124 424	124 440	124 443	126 078	125 869	−209
35	3s 6s	$^3S_1$	130 615	130 689	130 716	130 740	130 758	130 761	132 386	132 216	−170

Notes. The energies are given as a function of the increasing active set of orbitals, accounting for VV correlation, where n indicates the maximum principle quantum number of the orbitals included in the active set. In Col. 10, the final energy values are displayed after accounting for CV correlation. The differences ΔE between the final computations and the observed values are shown in the last column. The sequence and naming of the configurations and LSJ-levels are in accordance with the final (CV) computed energies. The levels of the singlet and triplet 3s6h ^{1,3}H and the 3p3d ^{1}D level have not yet been observed, and so the ΔE values are not available.

References. [a]NIST Atomic Spectra Database 2018 (Kramida et al. 2018).

Table A.1. continued.

			VV								
Pos.	Conf.	LSJ	$n = 8$	$n = 9$	$n = 10$	$n = 11$	$n = 12$	$n = 13$	CV	E_{obs}[a]	ΔE
36		$^1S_0$	131 160	131 237	131 268	131 291	131 308	131 311	132 953	132 779	−174
37	3s 5d	$^3D_2$	131 265	131 307	131 326	131 348	131 365	131 368	133 013	132 823	−190
38		$^3D_1$	131 265	131 307	131 327	131 348	131 365	131 368	133 013	132 823	−190
39		$^3D_3$	131 266	131 307	131 326	131 347	131 365	131 368	133 017	132 823	−194
40	3s 5f	$^3F^o_2$	131 641	131 712	131 745	131 769	131 787	131 790	133 639	133 438	−201
41		$^3F^o_3$	131 647	131 718	131 751	131 776	131 794	131 797	133 644	133 443	−201
42		$^3F^o_4$	131 655	131 727	131 760	131 785	131 803	131 806	133 654	133 450	−204
43		$^1F^o_3$	131 968	132 048	132 082	132 106	132 124	132 128	133 866	133 682	−184
44	3s 5d	$^1D_2$	132 490	132 447	132 445	132 460	132 474	132 476	134 143	133 916	−227
45	3s 5g	$^3G_3$	132 487	132 577	132 611	132 636	132 654	132 657	134 359	134 184	−175
46		$^3G_4$	132 487	132 577	132 611	132 636	132 654	132 658	134 360	134 184	−176
47		$^3G_5$	132 487	132 577	132 611	132 636	132 654	132 657	134 360	134 184	−176
48		$^1G_4$	132 487	132 577	132 611	132 636	132 654	132 658	134 360	134 184	−176
49	3s 6p	$^1P^o_1$	133 288	133 366	133 387	133 411	133 428	133 431	135 132	134 919	−213
50		$^3P^o_0$	133 378	133 459	133 485	133 509	133 526	133 530	135 183	135 012	−171
51		$^3P^o_1$	133 381	133 462	133 488	133 512	133 530	133 533	135 186	135 016	−170
52		$^3P^o_2$	133 388	133 468	133 494	133 518	133 536	133 539	135 192	135 022	−170
53	3s 7s	$^3S_1$	136 870	136 949	136 975	136 999	137 014	137 017	138 675	138 500	−175
54	3s 6f	$^3F^o_2$	136 665	136 628	136 655	136 678	136 695	136 698	138 810	138 521	−289
55		$^3F^o_3$	136 684	136 649	136 677	136 699	136 717	136 720	138 829	138 539	−290
56		$^3F^o_4$	136 709	136 677	136 704	136 727	136 745	136 748	138 862	138 562	−300
57	3s 7s	$^1S_0$	137 154	137 236	137 267	137 291	137 307	137 311	138 974	138 801	−173
58	3s 6d	$^3D_2$	137 217	137 273	137 297	137 314	137 331	137 333	139 005	138 815	−190
59		$^3D_1$	137 217	137 273	137 297	137 314	137 331	137 333	139 005	138 815	−190
60		$^3D_3$	137 218	137 273	137 297	137 314	137 331	137 333	139 010	138 815	−195
61	3s 6f	$^1F^o_3$	137 562	137 625	137 657	137 681	137 699	137 702	139 437	139 245	−192
62	3s 6d	$^1D_2$	137 753	137 754	137 767	137 786	137 801	137 803	139 497	139 289	−208
63	3s 6g	$^3G_3$	137 898	137 988	138 022	138 046	138 065	138 067	139 766	139 591	−175
64		$^3G_4$	137 898	137 988	138 022	138 046	138 065	138 068	139 766	139 591	−175
65		$^3G_5$	137 898	137 988	138 022	138 046	138 065	138 067	139 766	139 591	−175
66		$^1G_4$	137 898	137 988	138 022	138 047	138 065	138 068	139 766	139 591	−175
67	3s 6h	$^3H^o_4$	137 965	138 043	138 079	138 103	138 121	138 125	139 817		
68		$^3H^o_5$	137 965	138 043	138 079	138 103	138 121	138 125	139 817		
69		$^1H^o_5$	137 965	138 043	138 079	138 103	138 121	138 125	139 817		
70		$^3H^o_6$	137 965	138 043	138 079	138 103	138 121	138 125	139 817		
71	3s 7p	$^1P^o_1$	138 286	138 364	138 360	138 384	138 401	138 402	140 148	139 919	−229
72		$^3P^o_0$	138 439	138 522	138 545	138 569	138 587	138 589	140 266	140 090	−176
73		$^3P^o_1$	138 441	138 524	138 547	138 571	138 589	138 591	140 268	140 092	−176
74		$^3P^o_2$	138 445	138 529	138 552	138 575	138 593	138 595	140 272	140 096	−176
75	3p 3d	$^3F^o_2$	136 665	136 628	136 655	136 678	136 695	139 291	141 615	141 085	−531
76		$^3F^o_3$	136 684	136 649	136 677	136 699	136 717	139 311	141 665	141 110	−555
77		$^3F^o_4$	136 709	136 677	136 704	136 727	136 745	139 338	141 768	141 143	−625
78	3p 3d	$^1D^o_2$	140 333	140 372	140 385	140 408	140 425	140 428	142 964		

Table A.2. Comparison between computed and observed lifetimes τ in seconds for 75 excited states in Al II.

			RCI[a]		MCHF-BP[b]	BSCI[c]	Expt.[d,e,f]
Pos.	Conf.	$LS\,J$	τ_l	τ_v	τ_l		$\tau_{\rm obs}$
1	3s3p	$^3P^o_1$	3.274E-04	2.965E-04	3.051E-04		3.02 (2) E-04[e]
2		$^1P^o_1$	7.120E-10	7.089E-10	7.141E-10	6.70 E-10	6.90(13)E-10[d]
3	$3p^2$	$^1D_2$	3.351E-06	2.630E-06	2.270E-06	2.51 E-06	
4	3s4s	$^3S_1$	1.318E-09	1.325E-09	1.322E-09	1.32 E-09	
5	$3p^2$	$^3P_0$	8.091E-10	8.032E-10	8.098E-10		
6		$^3P_1$	8.081E-10	8.023E-10	8.082E-10		
7		$^3P_2$	8.059E-10	8.000E-10	8.054E-10		
8	3s4s	$^1S_0$	2.921E-09	2.922E-09	2.893E-09	2.93 E-09	
9	3s3d	$^3D_2$	8.337E-10	8.346E-10	8.252E-10	8.00 E-10	
10		$^3D_1$	8.319E-10	8.328E-10	8.233E-10	8.00 E-10	
11		$^3D_3$	8.358E-10	8.357E-10	8.277E-10	8.00 E-10	
12	3s4p	$^3P^o_0$	1.390E-08	1.394E-08	1.384E-08	1.403E-08	
13		$^3P^o_1$	1.386E-08	1.391E-08	1.379E-08	1.403E-08	
14		$^3P^o_2$	1.379E-08	1.384E-08	1.369E-08	1.403E-08	
15		$^1P^o_1$	1.099E-08	1.113E-08	1.116E-08	1.007E-08	
16	3s3d	$^1D_2$	7.204E-10	7.192E-10	6.994E-10	7.20 E-10	
17	$3p^2$	$^1S_0$	9.804E-10	9.758E-10	9.720E-10	9.50 E-10	
18	3s5s	$^3S_1$	2.767E-09	2.785E-09		2.78 E-09	
19		$^1S_0$	4.059E-09	4.055E-09		4.33 E-09	
20	3s4d	$^3D_2$	3.862E-09	3.872E-09		3.71 E-09	
21		$^3D_1$	3.850E-09	3.860E-09		3.71 E-09	
22		$^3D_3$	3.880E-09	3.889E-09		3.71 E-09	
23	3s4f	$^3F^o_2$	4.235E-09	4.254E-09			6.4 (5)E-09[f]
24		$^3F^o_3$	4.230E-09	4.248E-09			6.4 (5)E-09[f]
25		$^3F^o_4$	4.230E-09	4.256E-09			6.4 (5)E-09[f]
26		$^1F^o_3$	3.428E-09	3.438E-09			
27	3s4d	$^1D_2$	1.366E-09	1.368E-09		1.31 E-09	
28	3s5p	$^3P^o_0$	4.903E-08	4.941E-08		4.928E-08	
29		$^3P^o_1$	4.862E-08	4.899E-08		4.928E-08	
30		$^3P^o_2$	4.850E-08	4.903E-08		4.928E-08	
31		$^1P^o_1$	1.315E-08	1.377E-08		1.263E-08	
32	3s6s	$^3S_1$	5.196E-09	5.242E-09		5.19 E-09	
33		$^1S_0$	7.265E-09	7.254E-09		7.61 E-09	
34	3s5d	$^3D_2$	1.077E-08	1.081E-08		1.03 E-08	
35		$^3D_1$	1.073E-08	1.077E-08		1.03 E-08	

Notes. For the current RCI calculations length τ_l and velocity τ_v forms are both displayed. In Cols. 6 and 7, the predicted lifetimes from MCHF-BP and BSCI calculations are, respectively, given in length form. The last column contains available lifetimes from experimental measurements, together with their uncertainties.

References. [(a)]Present calculations; [(b)]Froese Fischer et al. (2006); [(c)]Chang & Fang (1995); [(d)]Kernahan et al. (1979), Smith (1970), Berry et al. (1970), Head et al. (1976); [(e)]Träbert et al. (1999), Johnson et al. (1986); [(f)]Andersen et al. (1971).

Table A.2. continued.

Pos.	Conf.	*LS J*	RCI[a] τ_l	RCI[a] τ_v	MCHF-BP[b] τ_l	BSCI[c]	Expt.[d,e,f] τ_{obs}
36		$^3D_3$	1.085E-08	1.090E-08		1.03 E-08	
37	3s5f	$^3F^o_2$	1.337E-08	1.356E-08			1.4 (2)E-08[f]
38		$^3F^o_3$	1.328E-08	1.348E-08			1.4 (2)E-08[f]
39		$^3F^o_4$	1.320E-08	1.345E-08			1.4 (2)E-08[f]
40		$^1F^o_3$	5.981E-09	6.015E-09			
41	3s5d	$^1D_2$	3.523E-09	3.525E-09		3.37 E-09	
42	3s5g	$^3G_3$	1.389E-08	1.390E-08			
43		$^3G_4$	1.389E-08	1.389E-08			
44		$^3G_5$	1.389E-08	1.390E-08			
45		$^1G_4$	1.383E-08	1.384E-08			
46	3s6p	$^1P^o_1$	1.322E-08	1.425E-08		1.211E-08	
47		$^3P^o_0$	1.147E-07	1.171E-07		1.105E-07	
48		$^3P^o_1$	1.097E-07	1.122E-07		1.105E-07	
49		$^3P^o_2$	1.137E-07	1.173E-07		1.105E-07	
50	3s7s	$^3S_1$	9.039E-09	9.167E-09		8.78 E-09	
51	3s6f	$^3F^o_2$	2.041E-08	2.051E-08			1.5 (1)E-08[f]
52		$^3F^o_3$	2.111E-08	2.125E-08			1.5 (1)E-08[f]
53		$^3F^o_4$	2.222E-08	2.236E-08			1.5 (1)E-08[f]
54	3s7s	$^1S_0$	1.174E-08	1.170E-08			
55	3s6d	$^3D_2$	2.386E-08	2.399E-08		2.234E-08	
56		$^3D_1$	2.376E-08	2.391E-08		2.234E-08	
57		$^3D_3$	2.423E-08	2.445E-08		2.234E-08	
58	3s6f	$^1F^o_3$	9.655E-09	9.720E-09			
59	3s6d	$^1D_2$	7.546E-09	7.518E-09		7.46 E-09	
60	3s6g	$^3G_3$	2.415E-08	2.417E-08			
61		$^3G_4$	2.412E-08	2.413E-08			
62		$^3G_5$	2.417E-08	2.415E-08			
63		$^1G_4$	2.373E-08	2.375E-08			
64	3s6h	$^3H^o_4$	3.753E-08	3.759E-08			
65		$^3H^o_5$	3.753E-08	3.759E-08			
66		$^1H^o_5$	3.753E-08	3.759E-08			
67		$^1H^o_6$	3.753E-08	3.759E-08			
68	3s7p	$^1P^o_1$	1.238E-08	1.450E-08		1.081E-08	
69		$^3P^o_0$	1.904E-07	2.090E-07		1.608E-07	
70		$^3P^o_1$	1.897E-07	2.078E-07		1.608E-07	
71		$^3P^o_2$	1.865E-07	2.148E-07		1.608E-07	
72	3p3d	$^3F^o_2$	2.769E-09	2.735E-09			3.5 (3)E-09[f]
73		$^3F^o_3$	2.736E-09	2.701E-09			3.5 (3)E-09[f]
74		$^3F^o_4$	2.586E-09	2.539E-09			3.5 (3)E-09[f]
75		$^1D^o_2$	8.207E-10	8.198E-10			

Paper II

Effect of realistic nuclear charge distributions on isotope shifts and progress towards the extraction of higher-order nuclear radial moments

A. Papoulia,[1] B. G. Carlsson,[1,*] and J. Ekman[2]

[1]*Division of Mathematical Physics, LTH, Lund University, Post Office Box 118, S-22100 Lund, Sweden*

[2]*Group for Materials Science and Applied Mathematics, Malmö University, S-20506 Malmö, Sweden*

(Received 13 April 2016; published 3 October 2016)

Atomic spectral lines from different isotopes display a small shift in energy, commonly referred to as the line isotope shift. One of the components of the isotope shift is the field shift, which depends on the extent and the shape of the nuclear charge density distribution. The purpose of this work is to investigate how sensitive field shifts are with respect to variations in the nuclear size and shape and what information of nuclear charge distributions can be extracted from measurements. Nuclear properties are obtained from nuclear density functional theory calculations based on the Skyrme-Hartree-Fock-Bogoliubov approach. These results are combined with multiconfiguration Dirac-Hartree-Fock methods to obtain realistic field shifts and it is seen that phenomena such as nuclear deformation and variations in the diffuseness of nuclear charge distributions give measurable contributions to the isotope shifts. Using a different approach, we demonstrate the possibility to extract information concerning the nuclear charge densities from the observed field shifts. We deduce that combining methods used in atomic and nuclear structure theory gives an improved description of field shifts and that extracting additional nuclear information from measured isotope shifts is possible in the near future with improved experimental methods.

DOI: 10.1103/PhysRevA.94.042502

I. INTRODUCTION

Information of nuclear sizes has grown rapidly during the last decades. In the compilation by Angeli and Marinova in 2013 [1], root-mean-square (rms) radii were reported for more than 900 isotopes of which the majority are radioactive systems. This development is a consequence of refined experimental and theoretical methods, and a state-of-the-art example is the frequency comb measurement of the hydrogen-deuterium radius difference by Parthey *et al.* [2]. The plenitude of available data has allowed for detailed investigations of the evolution of nuclear radii for isotope sequences along virtually the entire periodic table. These studies have revealed unexpected trends, especially close to magic numbers, which serve as benchmarks for nuclear structure calculations [3].

However, more detailed and model-independent experimental information of nuclear charge distributions beyond the rms radius is only available for stable or long-lived isotopes from electron scattering experiments. On the theoretical side it has been shown that isotope shifts in heavier systems depend on the nuclear model used [4] and that the contribution from nuclear deformation to the isotope shift in some cases is comparable to the uncertainty in recent dielectronic recombination experiments [5,6].

Experimental techniques such as high-precision laser measurements at the COLLAPS and CRIS experiments at ISOLDE/CERN [7] and dielectronic recombination experiments at the envisaged realization of CRYRING at GSI [8] are constantly evolving. This justifies a more systematic theoretical investigation of what information can be revealed about nuclear charge distributions in exotic systems.

The main objective of this work is to study the effect of realistic charge distributions, taken from nuclear density functional theory (DFT), on the isotope shift in heavier atoms. In addition, a promising method for the extraction of higher-order radial moments from experimental isotope shifts is also presented and tested.

II. ISOTOPE SHIFTS

The atomic nucleus is $\sim 10^4$ smaller than the size of the atom. Even so, the finite mass and extended charge distribution of the nucleus have a measurable effect on atomic spectra. Spectral lines from different isotopes display a small shift in energy referred to as the isotope shift (IS), which can further be decomposed into a mass shift (MS) and a field shift (FS) contribution. The difference in energy between the corresponding atomic level i of two isotopes A and A', the level isotope shift, can thus be expressed as

$$\delta E_{i,\mathrm{IS}}^{A,A'} = \delta E_{i,\mathrm{MS}}^{A,A'} + \delta E_{i,\mathrm{FS}}^{A,A'} = E_i^{A'} - E_i^{A}. \tag{1}$$

For a particular atomic transition k between upper u and lower l levels, the difference in energy for a pair of isotopes, namely, the line frequency isotope shift, is consequently given by

$$\begin{aligned}\delta\nu_{k,\mathrm{IS}}^{A,A'} &= \delta\nu_{k,\mathrm{MS}}^{A,A'} + \delta\nu_{k,\mathrm{FS}}^{A,A'} = \nu_k^{A'} - \nu_k^{A} \\ &= \frac{\delta E_{u,\mathrm{IS}}^{A,A'} - \delta E_{l,\mathrm{IS}}^{A,A'}}{h}.\end{aligned} \tag{2}$$

The level mass shift contribution can be expressed as

$$\delta E_{i,\mathrm{MS}}^{A,A'} = \left(\frac{M' - M}{MM'}\right) K_{\mathrm{MS}}^{i}, \tag{3}$$

where M and M' are the atomic masses of the isotopes and K_{MS}^{i} is the mass-independent mass shift parameter [9–11]. Although the computation of the mass shift parameters, and hence the mass shift contribution to the isotope shift, represents a challenging task, it is not the main focus of this work. Instead,

*gillis.carlsson@matfys.lth.se

the focus here is on the extent and shape of nuclear charge distributions which almost exclusively affect the field shift described in detail below.

A. Field shift

The field shift arises from differences in the nuclear charge density distribution between isotopes caused by the different number of neutrons. Unlike pointlike charge distributions, more realistic charge distributions alter the central field that the atomic electrons experience, and hence the atomic level and transition energies will be affected. Evidently, the field shift effect is more pronounced for electrons moving in $s_{1/2}$ and $p_{1/2}$ orbitals due to the nonzero probability of the radial wave functions at the origin. Moreover, the nuclear charge and extent, together with the contraction of the atomic orbitals, increase with the proton number Z and thus the contribution from the field shift to the isotope shift is found to be dramatically larger in heavier systems.

1. Nonperturbative "exact" method

In atomic structure calculations, where the contribution from the mass shift is neglected, the level field shift can be computed according to Eq. (1) by performing separate calculations for two isotopes A and A', with different parameter sets describing the respective nuclear charge distributions. This method is in general highly model dependent since the description of the nucleus is normally restricted to an approximate model. Moreover, this procedure is cumbersome if calculations are to be performed for many isotope pairs and in addition it may suffer from numerical instabilities since it involves the substraction of large quantities (atomic binding energies) to obtain a tiny quantity. Nevertheless, this strategy constitutes an "exact" method for estimating the validity of perturbative approaches and the resulting field shifts will be denoted $\delta\nu^{\text{exact}}_{k,\text{VA}}$ below.

2. Perturbative method

To eliminate the disadvantages of the exact method described above and allow for a more flexible analysis of the field shift, an alternative approach based on perturbation theory may be used. Within the framework of perturbation, the first-order level field shift of level i can be written

$$\delta E^{(1)A,A'}_{i,\text{FS}} = -\int_{R^3} [V_{A'}(\boldsymbol{r}) - V_A(\boldsymbol{r})]\rho^e_i(\boldsymbol{r})d^3\boldsymbol{r}, \tag{4}$$

where $V_A(\boldsymbol{r})$ and $V_{A'}(\boldsymbol{r})$ are the one-electron potentials arising from the different nuclear charge distributions of the two isotopes and $\rho^e_i(\boldsymbol{r})$ is the electron density inside the nuclear volume of the reference isotope A.

Following the work by Seltzer [12], Torbohm *et al.* [13], and Blundell *et al.* [14] and assuming an extended spherical symmetric nuclear charge distribution, it can be shown that the electron density to a very good approximation can be expanded around $r = 0$ as an even polynomial function keeping only the first few terms:

$$\rho^e_i(\boldsymbol{r}) \approx b_i(r) = b_{i,1} + b_{i,2}r^2 + b_{i,3}r^4 + b_{i,4}r^6. \tag{5}$$

Inserting the expression above in Eq. (4) and making use of the Laplacian operator in spherical coordinates, $\nabla^2 r^{2N} = 2N(2N+1)r^{2N-2}$, Poisson's equation $\nabla^2 V_A(\boldsymbol{r}) = -4\pi\rho_A(\boldsymbol{r})$, and finally Eq. (2), the first-order line frequency field shift is given by [14,15]

$$\delta\nu^{(1)A,A'}_{k,\text{FS}} \approx \delta\nu^{A,A'}_{k,\text{RFS}} = \sum_{N=1}^{4} F_{k,N}\delta\langle r^{2N}\rangle^{A,A'}, \tag{6}$$

where $F_{k,N}$ are the so-called line electronic factors expressed as

$$F_{k,N} = \frac{2\pi}{h}\frac{Z\Delta b_{k,N}}{N(2N+1)}, \tag{7}$$

and

$$\delta\langle r^{2N}\rangle^{A,A'} = \langle r^{2N}\rangle^{A} - \langle r^{2N}\rangle^{A'} \tag{8}$$

are the differences of the nuclear radial moments, of order $2N$, of the isotopes A and A'. The electronic factors are proportional to the difference of the electronic density inside the nucleus between the upper and lower atomic level, thus, $\Delta b_{k,N} = b_{u,N} - b_{l,N}$.

The reformulated field shift (RFS) according to Eq. (6) enables a more versatile analysis of field shifts. This is due to the fact that the radial moments $\langle r^{2N}\rangle$ used in the expression can be taken from any model, calculation, or experiment. In addition, it is possible to analyze the contributions to the field shift order by order. For example, keeping only the first term in Eq. (6) we obtain

$$\delta\nu^{(1)A,A'}_{i,\text{FS}} \approx \frac{2\pi}{3h}Z\Delta\rho^e_i(\boldsymbol{0})\delta\langle r^2\rangle^{A,A'}, \tag{9}$$

which is a suitable approximation for lighter systems where a constant electron density within the nucleus can be assumed, $\rho^e_i(\boldsymbol{r}) \approx b_{i,1} = \rho^e_i(\boldsymbol{0})$. For heavier systems, however, the electron density varies inside the nuclear volume and thus the $N \geqslant 2$ terms in Eq. (6) must also be considered for an accurate description. Further on, by including these higher-order contributions, the effect on the isotope shift due to details in the nuclear charge distribution can be analyzed. As we shall see, the reversed approach is also possible, namely, to extract higher-order radial moments of the nuclear charge distribution from observed isotope shifts.

B. Computational procedure

Solutions to the many-body Hamiltonian describing the atom are obtained by performing calculations using the relativistic atomic structure package GRASP2K [16], which is based on the multiconfiguration Dirac-Hartree-Fock (MCDHF) approach. In the MCDHF method, atomic state functions $\Psi(\gamma PJM_J)$, which are approximate solutions to the Dirac-Coulomb Hamiltonian, are expanded over configuration state functions (CSFs), $\Phi(\gamma_i PJM_J)$, with appropriate total angular momentum (J) symmetry and parity P:

$$\Psi(\gamma PJM_J) = \sum_{i=1}^{N} c_i\Phi(\gamma_i PJM_J). \tag{10}$$

In the expression above, γ_i represents the configuration, coupling, and other quantum number necessary to uniquely describe the state i, M_J is the projection of J on the z axis, and c_i are mixing coefficients fulfilling the condition $\sum_{i=1}^{N} c_i^2 = 1$.

The CSFs are constructed from one-electron Dirac orbitals that together with the mixing coefficents are obtained in a relativistic self-consistent-field procedure by applying the variational principle [17]. The transverse photon interaction as well as leading quantum electrodynamic (QED) corrections can be accounted for in subsequent relativistic configuration interaction (RCI) calculations [18].

Once a set of ASFs is obtained, the computation of the isotope shift parameters is carried out using the program RIS4 [15], which represents an extension of the predecessor RIS3 [19]. In RIS4 the polynomial expansion $b_i(r)$ given by Eq. (5) is for each level fitted to the constructed electron density $\rho_i^e(\boldsymbol{r})$ using a least-squares method. Finally, by combining the expansion coefficients $b_{i,N}$ from two or more levels, the line electronic factors are computed for the reference isotope A according to Eq. (7).

III. REALISTIC NUCLEAR CHARGE DISTRIBUTIONS

As seen above, the reformulated field shift depends on the radial moments of the nuclear charge distribution. These moments can be calculated from nuclear models that provide accurate charge distributions. In this section, three such models are compared.

A. Nuclear charge distribution models

The nuclear charge distribution can be approximated by an analytical expression such as the Fermi distribution

$$\rho(r,\theta) = \frac{\rho_0}{1 + e^{\frac{r - c(\theta)}{a}}}, \tag{11}$$

where, if only axially symmetric quadrupole deformation is considered, $c(\theta) = c_0[1 + \beta_{20} Y_{20}(\theta)]$. This modified Fermi distribution has been used previously to investigate the effect of deformation on atomic binding energies in Li-like systems [5,20,21]. In these studies, nuclear deformation parameters extracted from highly accurate muonic atom studies were used [22,23]. The value of $\rho_0 \approx \rho(r = 0)$ is determined by the normalization condition

$$\int \rho(\boldsymbol{r}) d\boldsymbol{r} = 1, \tag{12}$$

and the parameter α is given by the relation

$$t = 4 \ln(3) \alpha, \tag{13}$$

where t is the skin thickness of the distribution. The skin thickness is defined as the interval where the density decreases from 90% to 10% of $\rho(0)$. The parameter c_0 reflects the size of the nucleus.

In the GRASP2K code [16], the explicit values for these parameters are taken as [4] $t = 2.3$ fm, $\beta_{20} = 0$ and the parameter c_0 is chosen so that the rms radius of the nuclear charge distribution becomes

$$\sqrt{\langle r^2 \rangle} = 0.836 A^{\frac{1}{3}} + 0.570 \text{ fm } (A > 9), \tag{14}$$

where A denotes the number of nucleons of the isotope.

Realistic nuclear charge distributions can also be obtained from microscopic nuclear models based on effective interactions. Such models have the advantage that the size, shape, and diffuseness of the nuclear density is obtained by solving a self-consistent set of Hartree-Fock-Bogoliubov (HFB) equations.

In this work, we adopt the effective Skyrme interaction [24] and consider two different sets of Skyrme parameters called SLY4 and UNEDF1. The parameters in both sets are adjusted to fit experimental data in a broad range of nuclei. The SLY4 set was fitted with an emphasis on describing neutron-rich nuclei [25], whereas the UNEDF1 set constitutes a more recent parametrization fitted to reproduce both ground-state energies as well as radii and single-particle energies [26]. In spherical symmetry, the solutions to the HFB equations are provided by the code HOSPHE (v2.00), which is a new version of the program HOSPHE (v1.02) [27]. In the case of deformed nuclei, we use the code HFBTHO (2.00d) [28], based on a cylindrically deformed harmonic oscillator (HO) basis.

For spherical nuclei, we take into account the finite nature of protons by folding the densities using the convolution formula

$$\varrho_c(\boldsymbol{r}) = \int d^3\boldsymbol{r}' \rho_p(\boldsymbol{r}') g(|\boldsymbol{r} - \boldsymbol{r}'|), \tag{15}$$

where $\rho_p(\boldsymbol{r})$ is the initially calculated proton density and

$$g(\boldsymbol{r}) = (r_0\sqrt{\pi})^{-3} e^{-(\boldsymbol{r}/r_0)^2} \tag{16}$$

the proton form factor, assumed to be a Gaussian with $r_0 = \sqrt{\frac{2}{3}} r_p^{\text{rms}}$, where r_p^{rms} is the proton rms radius [29]. Experiments to determine the proton radius have resulted in different values of r_p^{rms} [30,31], and in this work we adopt the results based on electron scattering measurements assuming $r_p^{\text{rms}} = 0.88$ fm.

In Fig. 1, the theoretical rms radii are compared to experimental data obtained from elastic electron scattering experiments [32,33]. A total of 16 spherical isotopes of various elements, O, S, Ca, Ni, Sn, and Pb, are used in the comparison. As seen in this figure, both the nuclear models as well as the empirical parametrization [Eq. (14)] are in good agreement with the experimental data.

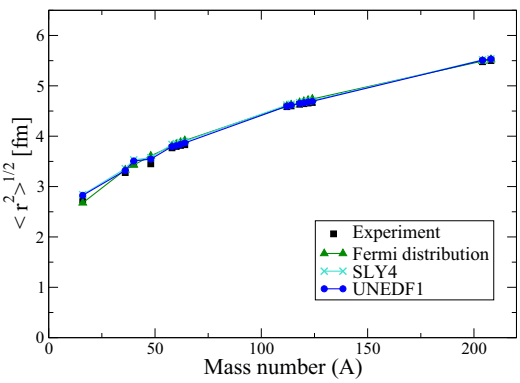

FIG. 1. Rms radii of theoretical charge distributions compared to experimental data. Two different Skyrme parameter sets, SLY4 and UNEDF1, are used with moments calculated after taking into account the finite proton size. The resulting $\sqrt{\langle r^2 \rangle}$ values from the Fermi distribution used in the GRASP2K code [Eq. (14)] are also included.

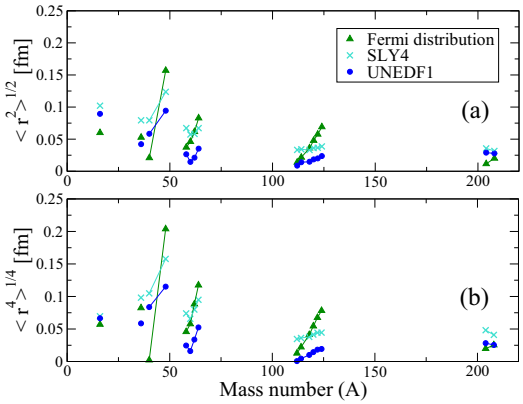

FIG. 2. Discrepancy of (a) the rms radii $\sqrt{\langle r^2 \rangle}$ and (b) the $\sqrt[4]{\langle r^4 \rangle}$ moment of the theoretical charge distributions compared to experimental data. Isotopic sequences are connected with lines.

The discrepancy between the theoretical and the experimental $\sqrt{\langle r^2 \rangle}$ values is shown in Fig. 2(a). As seen in this figure, the more recent Skyrme parameters (UNEDF1) give the best description of the data. The two microscopic models also stand out as they are in general better at capturing the isotopic trends giving flatter curves than the Fermi distribution.

For calculations of field shifts, the higher-order moments may also play an important role and in Fig. 2(b) the discrepancy in the prediction of the $\sqrt[4]{\langle r^4 \rangle}$ values is shown. This comparison shows the same trend as for the $\sqrt{\langle r^2 \rangle}$ values, namely, that microscopic models capture the isotopic trends better while the Fermi distribution in general does a good job for the stable nuclei. One might consider using more refined empirical expressions containing a dependence on the difference in proton and neutron numbers, but since such an approach would anyway not capture the important changes caused by deformations, the best approach comes from using state-of-the-art microscopic nuclear models.

In Table I, the standard deviations of the discrepancies for the three models are compared. Considering the average agreement, the Fermi distribution and the Skyrme-SLY4 give similar results while the more recent UNEDF1 is significantly better. In addition, the UNEDF1 set predicts the $\sqrt{\langle r^2 \rangle}$ and $\sqrt[4]{\langle r^4 \rangle}$ moments with about the same precision, while the precision deteriorates slightly for the two other models. This agrees with the fact that the full density profiles also tend to be better reproduced by UNEDF1. Higher-order moments are difficult to compare since more focus is then shifted towards the surface and tail of the density where insufficient precision in the data hampers a qualitative comparison. All in all, the UNEDF1 parametrization describes the nuclear charge distributions more accurately than both the Skyrme-SLY4 and Fermi distributions and therefore realistic nuclear radial moments resulting from this interaction will be used in the following in order to estimate the line field shifts.

TABLE I. Standard deviations of discrepancies in $\sqrt{\langle r^2 \rangle}$ and $\sqrt[4]{\langle r^4 \rangle}$, calculated for the three theoretical models.

	$\sqrt{\langle r^2 \rangle}$	$\sqrt[4]{\langle r^4 \rangle}$
Fermi distribution	0.01660	0.01954
Skyrme-SLY4	0.01821	0.01905
Skyrme-UNEDF1	0.01271	0.01260

B. Application to line field shifts

In this section, the atomic physics calculations for the electron energies are combined with the use of the microscopic nuclear models for the charge densities. As an example, we consider the resonance transition $6s^2\,{}^1S_0 \longrightarrow 6s6p\,{}^1P_1^o$ observed in several neutral Ba isotopes. By comparing the line field shift in the isotope series one may be able to draw conclusions on the shape and size of the nuclear density distributions. The most abundant barium isotope on Earth, ^{138}Ba, is taken as a reference and the shifts in electron energies are thus compared to the values for this isotope. This reference isotope is spherical, while the other isotopes obtained by removing or adding a couple of neutrons are predicted to have more deformed shapes.

Figure 3 shows the calculated line field shifts for the Ba isotope series compared to experimental isotope shifts [34], where theoretical mass shift contributions have been subtracted [35]. The calculations based on the Fermi distribution show a linear dependence on the mass number A' of the target isotope and fail to capture the general trend. The microscopic nuclear calculations capture both the right trend with neutron number and in addition some of the odd-even staggering.

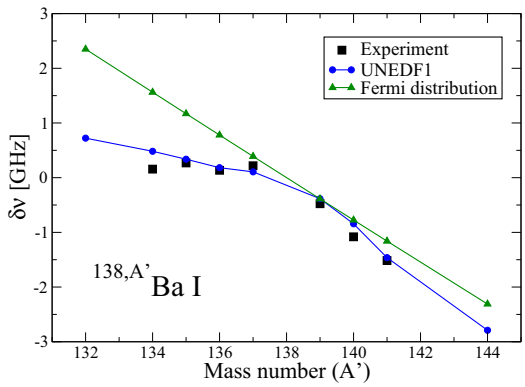

FIG. 3. The absolute line field shift values are compared to the available experimental data [34,35]. Nuclear radial moments resulted from the realistic HFB calculations using the Skyrme-UNEDF1 interaction, as well as from the Fermi distribution, have been used. All plotted values refer to the $6s^2\,{}^1S_0 \longrightarrow 6s6p\,{}^1P_1^o$ transition.

IV. EFFECT OF REALISTIC CHARGE DISTRIBUTIONS ON THE LINE FIELD SHIFTS

In order to investigate the resulting field shifts when replacing the commonly adopted Fermi distribution with more realistic nuclear models, we examine the differences in the predicted field shifts for a variety of isotopes. For such analysis, the Fermi distribution is fitted so that it has the same $\langle r^2\rangle$ value as computed from the realistic distributions. Then,

$$\delta\nu_{\text{Fermi}} = F_{k,1}\delta\langle r^2\rangle_{\text{realistic}} + \sum_{N=2}^{4} F_{k,N}\delta\langle r^{2N}\rangle_{\text{Fermi}}. \quad (17)$$

Thus, the correction when using realistic charge distributions is given by

$$\delta\nu_{\text{realistic}} - \delta\nu_{\text{Fermi}} = \sum_{n=2}^{4} F_{k,N}[\delta\langle r^{2N}\rangle_{\text{realistic}} - \delta\langle r^{2N}\rangle_{\text{Fermi}}]. \quad (18)$$

In the following two subsections, the size of this correction term will be investigated for lithium-like and neutral systems.

A. Li-like systems

Isotope shifts in lithium-like systems have been studied theoretically and experimentally in the past [5,6,36–38] and are thus of particular interest. In Fig. 4, the magnitude of the "correction term" $\delta\nu_{\text{realistic}} - \delta\nu_{\text{Fermi}}$ for one of the resonance transitions has been plotted as a function of the mass number A' of the target isotope for a wide range of Li-like systems. For the spherical Sn, Pb, Er, and Lv nuclear systems the magnitude of the corrections increases with A'. Moreover, the absolute magnitude of the $\delta\nu_{\text{realistic}} - \delta\nu_{\text{Fermi}}$ term increases with the difference between the neutron number $\Delta N^{A,A'}$ in the isotope sequences of Sn and Pb. When more neutrons are added, they alter the protons distribution, leading to changes in the diffuseness. This effect is not included in the Fermi model where a constant skin thickness $t \simeq 2.3$ fm is assumed and may be a reason for the observed difference.

In the deformed Rb, Nd, and U systems, the corrections depend on the size of the nuclei as well as the quadrupole deformation parameter β_{20}, which is assumed to be zero in the spherical Fermi model. Hence, for large deformations the corrections for the Rb and Nd isotope pairs are comparable to the ones obtained for the spherical Sn and Pb isotope pairs. For the heavier U isotopes, the corrections become significantly large in spite of the small difference in deformation between the reference and target isotopes.

In Fig. 5, the magnitude of the corrections has been plotted as a function of the calculated deformation parameter β_{20} corresponding to the isotope A' for some Nd and U isotope pairs. In both plots, the magnitude of the "correction term" increases as the difference between the deformation of reference and target isotope becomes large. The largest corrections are obtained for the uranium isotope pairs ^{240,238}U and ^{220,238}U. In this case, the correction amounts to ∼2.3% and ∼2%, respectively.

The two-parameter Fermi model does not take into account the effect of deformation. As a result, the effect of realistic charge distributions on the field shifts is larger in atomic systems with deformed nuclei. The correction term $\delta\nu_{\text{realistic}} - \delta\nu_{\text{Fermi}}$ can, however, be decomposed into two parts and written as

$$\delta\nu_{\text{realistic}} - \delta\nu_{\text{Fermi}} = \left(\delta\nu_{\text{realistic}} - \delta\nu^{\text{def}}_{\text{Fermi}}\right) + \left(\delta\nu^{\text{def}}_{\text{Fermi}} - \delta\nu^{\text{sph}}_{\text{Fermi}}\right). \quad (19)$$

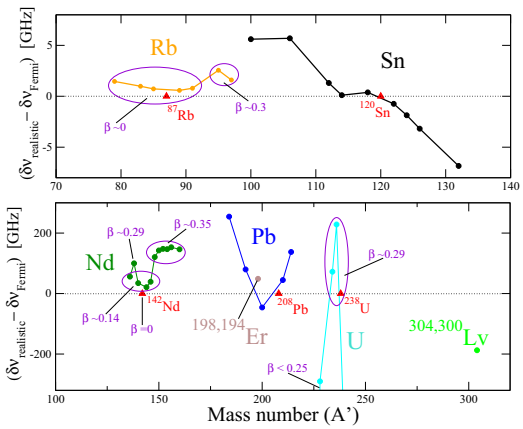

FIG. 4. The corrections $\delta\nu_{\text{realistic}} - \delta\nu_{\text{Fermi}}$ to the line field shift calculations as a function of the mass number A' of the target isotope for various Li-like systems. For the systems that contain deformed isotopes, the magnitude of the quadrupole deformation parameter β_{20} of the target isotopes A' is indicatively shown. The isotopes used as reference are marked with triangles and all plotted values refer to the $1s^2\,2s\,^2S_{1/2} \longrightarrow 1s^2\,2p\,^2P^o_{1/2}$ resonance transition.

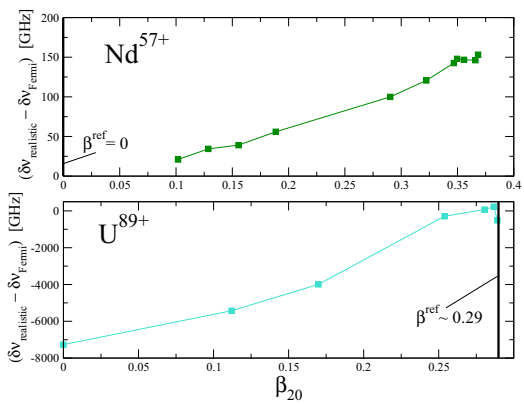

FIG. 5. The corrections $\delta\nu_{\text{realistic}} - \delta\nu_{\text{Fermi}}$ to the line field shift values as a function of the quadrupole deformation parameter β_{20} of the target A' isotope for various (a) Nd^{57+} and (b) U^{89+} isotope pairs. In each case, the corresponding deformation of the reference isotope A is indicated by a vertical line on the plots. All plotted values refer to the same resonance transition as in Fig. 4.

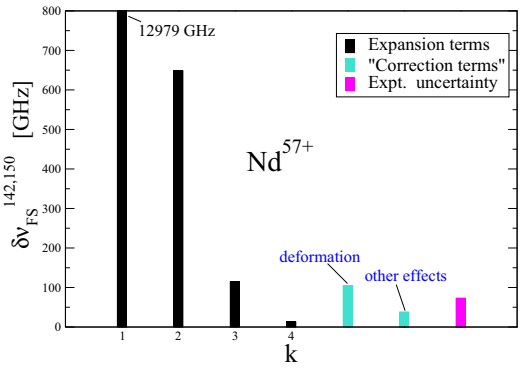

FIG. 6. Decomposition of expansion and correction terms of the $1s^2\,2s\,{}^2S_{1/2} \longrightarrow 1s^2\,2p\,{}^2P^o_{1/2}$ transition in Li-like ^{142,150}Nd.

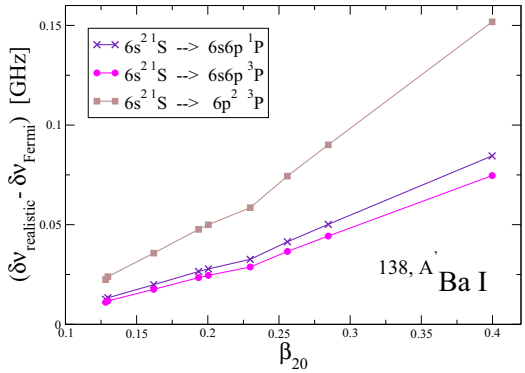

FIG. 7. The corrections $\delta\nu_{\text{realistic}} - \delta\nu_{\text{Fermi}}$ to the line field shift calculations as a function of the quadrupole deformation parameter β_{20} of the target A' isotope for the neutral barium isotope pairs.

The $\delta\nu^{\text{def}}_{\text{Fermi}} - \delta\nu^{\text{sph}}_{\text{Fermi}}$ part isolates the effect of deformation, while the remaining $\delta\nu_{\text{realistic}} - \delta\nu^{\text{def}}_{\text{Fermi}}$ part gives the corrections due to "other effects," such as density wiggles and differences in diffuseness. In order to separately estimate the effect of deformation in Li-like Nd, the deformed Fermi model was used with β_{20} values obtained from the microscopic nuclear calculations.

Isotope shift (IS) measurements have been performed for the first two resonance transitions of the ^{142,150}Nd^{57+} pair [37] and the statistical uncertainty of the observed isotope shift for the $1s^2\,2s\,{}^2S_{1/2} \longrightarrow 1s^2\,2p\,{}^2P^o_{1/2}$ transition is compared to the magnitude of the "correction terms" in Fig. 6. As seen in the figure, the effect of deformation is large enough to be detected by the experiments and the correction due to "other effects" is not negligible.

B. Neutral atoms

In this section, field shifts in neutral barium are investigated for the three well-known $6s^2\,{}^1S_0 \longrightarrow 6s6p\,{}^{1,3}P^o_1$ and $6s^2\,{}^1S_0 \longrightarrow 6p^2\,{}^3P_1$ transitions. Figure 7 illustrates the dependence of the magnitude of the corrections on the deformation parameter β_{20}. The same trend is seen for the three transitions. As already deduced for Nd^{57+} and U^{89+} (see Fig. 5) the magnitude of $\delta\nu_{\text{realistic}} - \delta\nu_{\text{Fermi}}$ increases as the difference between the deformation of reference and target isotope becomes large. However, in neutral barium the magnitude of the correction term $\delta\nu_{\text{realistic}} - \delta\nu_{\text{Fermi}}$ is a factor $\sim 10^3$ smaller.

In contrast to the IS measurements in Li-like systems, a greater number of measurements has been performed in neutral atomic systems. Furthermore, in such measurements the accuracy provided is generally much higher. Following the process described in the previous section, the correction term is decomposed for the $6s^2\,{}^1S_0 \longrightarrow 6s6p\,{}^1P^o_1$ transition of the ^{138,136}Ba isotope pair. The isotope shift measurements of the corresponding spectral lines [34] carries a statistical error, which is in Fig. 8 compared to the magnitude of the correction terms.

As seen in Fig. 8, the experimental uncertainty is remarkably small in comparison to the magnitude of the corrections. However, in reality the experimental uncertainty of the field shift is much larger since the theoretical mass shift contribution is in this case associated with large uncertainties, which are not reflected in this figure. The dominating corrections are the "other effects" that arise from the differences between the deformed Fermi distribution and the more realistic charge distributions obtained from the microscopic nuclear calculations.

The major improvement to the line field shift measurements illustrated in Fig. 3 is clearly due to the choice of using realistic rms radii. However, making in addition use of realistic higher-order nuclear moments leads to a non-negligible improvement in the description of the experimental data. According to the current experimental precision in the measurement of the isotope shifts in ^{136,138}Ba and ^{150,142}Nd^{57+}, effects like deformation captured by the higher nuclear moments could be detected (see Figs. 6 and 8). As a result, information about such

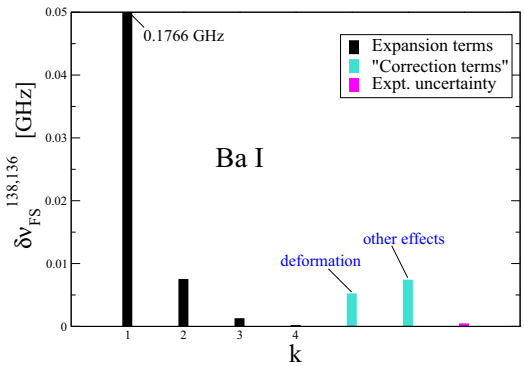

FIG. 8. Decomposition of expansion and correction terms of the $6s^2\,{}^1S_0 \longrightarrow 6s6p\,{}^1P^o_1$ transition in ^{138,136}Ba I.

a nuclear property could possibly be deduced from isotope shift observations.

V. $\delta\langle r^4\rangle^{A,A'}$ EXTRACTION

The nuclear charge radius is one of the most obvious and fundamental parameters, related to the size of the nucleus. Considering isotope shift measurements, the charge radii of an isotope sequence are typically determined in terms of the differences in the second radial moment $\delta\langle r^2\rangle$, between target isotope A' and reference isotope A. In contrast to light nuclei, in heavy nuclear systems the contribution of the higher-order radial moments to the line field shift can be significant and above the observable limit (see Figs. 6 and 8). Moreover, in highly charged heavy systems the contribution of the mass shift effect becomes smaller. This suggests the possibility to extract information about higher nuclear moments.

The reformulation of the field shift, combined with experimental isotope shift measurements, in principle enables the extraction of differences in higher-order radial moments $\delta\langle r^{2N}\rangle$, $N = 2,3,4$. Consequently, information about the nuclear shapes, deformations, density wiggles, and other nuclear properties can be provided. The extraction of all four radial moments requires four transitions k to be available. A system of four equations is then solved for

$$\delta\nu_{k,\mathrm{RFS}} = F_{k,1}\delta\langle r^2\rangle + F_{k,2}\delta\langle r^4\rangle + F_{k,3}\delta\langle r^6\rangle + F_{k,4}\delta\langle r^8\rangle, \tag{20}$$

where $k = 1,2,3,4$. However, it is rare that observed isotope shifts are available for four transitions and, in addition, such systems of equations cannot be formed so that they give trustworthy solutions for higher than second-order moments.

A. RFS expansion using orthogonal moments

As seen in Figs. 6 and 8, all four expansion terms do not equally contribute to the final field shift value. Considering in Fig. 9 the line field shift for the ^{208,200}Pb pair, the fourth-order radial moment adds ∼10% contribution, the sixth moment ∼2%, and the last term, which contains the eighth-order moment, contributes with much less. Thus, it is fair to say that the major correction to the approximation that assumes constant electron density $\rho_i^e(\boldsymbol{r}) \approx \rho_i^e(0)$ comes from the second expansion term, i.e., $F_{k,2}\delta\langle r^4\rangle$, which takes into account the differences between the $\langle r^4\rangle$ moments. However, the contribution from higher-order terms is not negligible.

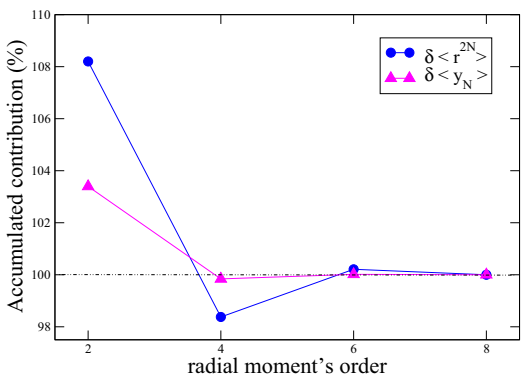

FIG. 9. $\sum_N F_N\delta\langle r^{2N}\rangle/\delta\nu$ in percent (circles) compared to the corresponding expression for the rearranged summation (triangles). The plot refers to the ^{208,200}Pb pair and the $1s^2\,2s\,{}^2S_{1/2} \longrightarrow 1s^2\,2p\,{}^2P^o_{1/2}$ transition.

In Eq. (20), the information about the nuclear charge distribution is encoded in a set of nuclear radial moments. These moments are not independent and a faster converging series may be found by instead expanding in a set of orthogonal polynomials (see Appendix). The convergence of this rearranged summation compared with the original summation is shown in Fig. 9. By taking into account only the first term, the line field shift is already much closer to the final value. The second term adds ∼3.5% contribution, the third ∼0.18%, while the last one adds ∼0.016%. Thus, accurate enough field shift predictions can now be provided using only the first two expansion terms containing the differences $\delta\langle y_1\rangle$ and $\delta\langle y_2\rangle$, which are in turn given as a function of the $\delta\langle r^2\rangle$ and $\delta\langle r^4\rangle$ moments (see Appendix). Having only two unknowns means that $\delta\langle r^2\rangle$ and $\delta\langle r^4\rangle$ can potentially be extracted from knowledge of two observed line field shifts in an isotope pair.

B. Testing the method

After expanding in the orthonormal basis, for a pair of isotopes A, A', the reformulated line field shift can to a very good approximation be expressed as

$$\delta\nu_{k,\mathrm{RFS}} \approx c_{k,1}\delta\langle y_1\rangle + c_{k,2}\delta\langle y_2\rangle, \tag{21}$$

where the $c_{k,1}$ and $c_{k,2}$ coefficients are expressed in terms of the $F_{k,N}$ factors. In order to test the method, theoretical line field shifts $\delta\nu_{\mathrm{RFS}}$ were obtained using realistic nuclear radial moments. These line field shifts refer to the $1s^2\,2s\,{}^2S_{1/2} \longrightarrow 1s^2\,2p\,{}^2P^o_{1/2}$ and $1s^2\,2s\,{}^2S_{1/2} \longrightarrow 1s^2\,2p\,{}^2P^o_{3/2}$ transitions of the uranium, lead, and neodymium isotope pairs studied in Sec. IV. Using these calculated field shifts as "pseudoexperimental" input data, the equations can be inverted and should yield, if the method is flawless, extracted radial moments which are identical to the realistic nuclear moments used in the computation of the field shifts.

In all cases, the extracted $\delta\langle r^2\rangle$ moments are almost identical to the exact $\delta\langle r^2\rangle_{\mathrm{realistic}}$ moments. The difference is less than 0.0002 fm^2 for all lead and uranium isotopes, as well as the neodymium isotopes that are close to spherical. For the highly deformed neodymium isotopes, the difference is slightly larger, of the order of ∼0.001 fm^2, which still represents a small discrepancy.

In Fig. 10, the extracted $\delta\langle r^4\rangle$ values have been plotted and compared to the $\delta\langle r^4\rangle_{\mathrm{realistic}}$ representing exact values. The extracted $\delta\langle r^4\rangle_{\mathrm{original}}$ values using the first two terms of the original summation $\delta\nu^{A,A'}_{k,\mathrm{RFS}} \approx \sum_{N=1}^{2} F_{k,N}\delta\langle r^{2N}\rangle$ are in addition illustrated in the same figure. When the rearranged summation is used, the extracted $\delta\langle r^4\rangle$ moments are in good agreement with the exact $\delta\langle r^4\rangle_{\mathrm{realistic}}$ moments, whereas the $\delta\langle r^4\rangle$ moments using the original, but truncated, summation display an observable discrepancy from the exact values. All in all, the expression using the rearranged summation for

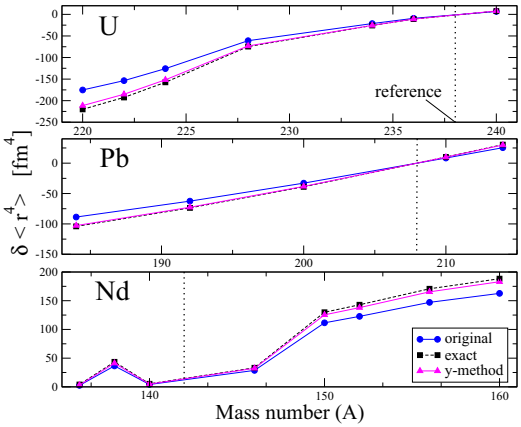

FIG. 10. The extracted $\delta\langle r^4\rangle$ values for the uranium, lead, and neodymium isotope pairs, previously studied. The dashed line with squares represents the exact $\delta\langle r^4\rangle_{\text{realistic}}$ values, obtained from the HFB and HFBTHO calculations for the spherical lead and the deformed uranium and neodymium isotopes, respectively. The line with triangle symbols represents the extracted $\delta\langle r^4\rangle$ when $\delta\nu_{k,\text{FS}} \approx c_{k,1}\delta\langle y_1\rangle + c_{k,2}\delta\langle y_2\rangle$ is assumed, while the line with circles corresponds to the $\delta\langle r^4\rangle_{\text{original}}$ extracted when the original summation in $\delta\nu_{k,\text{RFS}}$ has been used.

the reformulated field shift enables the determination of the differences between r^2 and r^4 moments, much more accurately than using the original expression.

C. Towards the extraction of $\delta\langle r^2\rangle$ and $\delta\langle r^4\rangle$ moments using experimental data

In what follows, the major objective is to discuss how $\delta\langle r^2\rangle$ and $\delta\langle r^4\rangle$ moments can be extracted from experimental data using the method tested above. From observed isotope shifts, experimental field shift values can be obtained by estimating and removing the mass shift contribution and residual effects $\delta\nu_{k,\text{RES}}$ from for example QED and nuclear polarization (see, e.g., [6]):

$$\delta\nu^{\text{expt}}_{k,\text{FS}} = \delta\nu^{\text{expt}}_{k,\text{IS}} - \delta\nu_{k,\text{MS}} - \delta\nu_{k,\text{RES}}. \tag{22}$$

The effect from nuclear polarization is not estimated in this work, but have been studied extensively in the past by Plunien *et al.* [39–42]. For Li-like systems, the contribution is comparable to the effect from deformation and must be taken into account in real situations.

Without making use of RFS, the difference in $\langle r^2\rangle$ moments can now be extracted by performing variational calculations where the rms radius of the reference isotope is estimated and $\delta\langle r^2\rangle$ is varied until agreement with experimental field shifts is observed (see, for example, [37]):

$$\delta\nu^{\text{expt}}_{k,\text{FS}} = \delta\nu^{\text{exact}}_{k,\text{VA}}. \tag{23}$$

The difference in higher moments then follows from the model used to mimic the nuclear charge distribution, for example the Fermi distribution, and hence this method is highly model dependent. However, making use of the reformulation of field shifts using an orthogonal moments basis, we instead use experimental field shift values from two transitions and solve the following equation system in order to extract the $\delta\langle r^2\rangle$ and $\delta\langle r^4\rangle$ moments virtually model independent:

$$\delta\nu^{\text{expt}}_{k,\text{FS}} = c_{k,1}\delta\langle y_1\rangle + c_{k,2}\delta\langle y_2\rangle + d_k. \tag{24}$$

In the expression above, a term d_k has been introduced which represents the discrepancy between the "exact" variational solution $\delta\nu^{\text{exact}}_{k,\text{VA}}$, and the RFS solution $\delta\nu_{k,\text{RFS}}$, assuming a spherical Fermi nuclear charge distribution for the reference and the target isotope. To examine the importance of the d_k term for the extraction of the radial moments, we used GRASP2K and RIS4 to compute $\delta\nu^{\text{exact}}_{k,\text{VA}}$ and $\delta\nu_{k,\text{RFS}}$ for the resonance transitions in several Li-like lead and uranium isotope pairs. In the calculations, rms radii were taken from the compilation by Angelis and Marinova [1] and the results are presented in Tables II and III. As seen, an expected discrepancy between the $\delta\nu^{\text{exact}}_{\text{VA}}$ and $\delta\nu_{\text{RFS}}$ values, i.e., the d_k term, is observed for both transitions. In our case, this discrepancy is mainly due to QED effects included in the VA calculation that become important in heavy nuclei and which are not included in the perturbative approach. In addition, these QED contributions (vacuum polarization and self-energy) depend on the nuclear size [43] and hence the d_k terms should be reevaluated when the nuclear parameters of the isotopes are changed. Other assumptions that have been made throughout the formulation of the perturbative approach are expected to play a minor role. Indicatively, for "transition 1" in the uranium isotope pairs the magnitude of the discrepancy is of the order of ∼1.5% of the $\delta\nu^{\text{exact}}_{\text{VA}}$ value, from which ∼0.1% is due to other than QED effects. It is also seen that the d_k terms for the two transitions are slightly different, and it turns out that accurately estimating this difference, rather than the magnitude of the

TABLE II. The line frequency field shift values, resulting from the variational calculations using GRASP2K and the reformulation of the field shift, are respectively displayed for a few lead and uranium isotope pair combinations. In the last column, the discrepancy between $\delta\nu^{\text{exact}}_{\text{VA}}$ and $\delta\nu_{\text{RFS}}$ is computed. "Transition 1" refers to the $1s^2\,2s\,{}^2S_{1/2} \longrightarrow 1s^2\,2p\,{}^2P^o_{1/2}$ transition.

Transition 1	$\delta\nu^{\text{exact}}_{\text{VA}}$ (GHz)	$\delta\nu_{\text{RFS}}$ (GHz)	d (GHz)
208,192	51 303	50 563	740
208,200	28 938	28 546	392
208,210	−14 186	−14 021	–165
238,234	54 796	53 976	820
238,236	27 412	27 015	397

TABLE III. Same as Table II. "Transition 2" refers to the $1s^2\,2s\,{}^2S_{1/2} \longrightarrow 1s^2\,2p\,{}^2P^o_{3/2}$ transition.

Transition 2	$\delta\nu^{\text{exact}}_{\text{VA}}$ (GHz)	$\delta\nu_{\text{RFS}}$ (GHz)	d (GHz)
208,192	55 459	54 642	817
208,200	31 282	30 848	434
208,210	−15 336	−15 152	–184
238,234	61 189	60 277	912
238,236	30 610	30 169	441

terms, is absolutely crucial in order to extract accurate $\delta\langle r^4\rangle$ moments.

We are now ready to show that it is possible to extract $\delta\langle r^2\rangle$ and $\delta\langle r^4\rangle$ moments if accurate experimental field shifts are available. This is due to the fact that the electronic factors c_k and the d_k terms can be accurately estimated also when the rms radii is not known for the reference and/or target isotope. In these cases, we make instead a "qualified guess" for the rms radii. The parametrization, given in Eq. (14), for the rms radius of an isotope A constitutes an example of such a "qualified guess" and will be used below.

1. Root-mean-square radii data available for the reference isotopes

When radial moment differences are deduced from isotope shift measurements, the nuclear parameters are usually known for the reference isotope but not for the target isotope. We will now demonstrate the procedure for how experimental $\delta\langle r^2\rangle$ and $\delta\langle r^4\rangle$ moments for the ^{238,234}U isotope can be extracted in such cases by considering the two resonance transitions in Li-like uranium. In what follows, ^{238}U is the reference isotope, $r_A^{\rm tab}$ denote a tabulated rms radius for isotope A taken from [1], $r_A^{\rm para}$ denote a parametrized rms radius for isotope A using Eq. (14), and spherical Fermi distributions with $t = 2.30$ fm are used everywhere. Further on it is assumed that accurate $\delta\nu_{k,\rm FS}^{\rm expt}$ values are available:

(1) Two separate variational calculations are performed using $r_{238}^{\rm tab} = 5.8571$ fm and $r_{234}^{\rm para} = 5.7216$ fm, respectively.

(2) $\delta\nu_{k,\rm VA}^{\rm exact}$ is constructed using the level energies from the $r_{238}^{\rm tab}$ and $r_{234}^{\rm para}$ calculations in step 1.

(3) $\delta\nu_{k,\rm RFS}$ is computed by using the electronic factors from the $r_{238}^{\rm tab}$ calculation and the difference in radial moments as predicted by two spherical Fermi distributions with $r_{238}^{\rm tab}$ and $r_{234}^{\rm para}$, respectively.

(4) $d_k = \delta\nu_{k,\rm VA}^{\rm exact} - \delta\nu_{k,\rm RFS}$ is computed.

(5) c_k factors are computed using the electronic factors in step 3 (see Appendix).

(6) $\delta\langle y_1\rangle$ and $\delta\langle y_2\rangle$ are extracted by solving Eq. (24).

(7) $\delta\langle r^2\rangle$ and $\delta\langle r^4\rangle$ are computed (see Appendix).

To quantitatively validate the method we replace $\delta\nu_{k,\rm FS}^{\rm expt}$ with "pseudoexperimental" field shifts constructed from two separate variational calculations using $r_{238}^{\rm tab}$ and $r_{234}^{\rm tab} = 5.8291$ fm, respectively. In addition, we repeat the procedure for the ^{238,236}U isotope pair using $r_{236}^{\rm para} = 5.7363$ fm and $r_{236}^{\rm tab} = 5.8431$ fm. In Table IV, the extracted $\delta\langle r^2\rangle$ and $\delta\langle r^4\rangle$ moments are compared to the experimental $\delta\langle r^2\rangle_{\rm expt}$ and $\delta\langle r^4\rangle_{\rm expt}$ moments. As seen, the extracted $\delta\langle r^2\rangle$ moments are almost identical to the "experimental" values. In addition, the $\delta\langle r^4\rangle$ moments are extracted with an accuracy of 5.3% and 4.2% for the ^{234,238}U and ^{236,238}U pairs, respectively. The errors, which are of systematical nature and remarkably small, arise from estimating the d term using rms radii for the target isotopes which differ by approximately 0.11 fm from the tabulated values used to construct the "pseudoexperimental" field shifts. However, after the extraction one obtains a better estimate for the rms radii of the target isotopes that allows the method to be iteratively improved.

2. Root-mean-square radii unknown for both target and reference isotopes

Assuming that the rms radius value of the reference isotope is also unknown, we again try to extract the $\delta\langle r^2\rangle$ and $\delta\langle r^4\rangle$ moments. A "qualified guess" for the rms radius of ^{238}U is then needed and we replace $r_{238}^{\rm tab}$ with $r_{238}^{\rm para} = 5.7508$ fm in the procedure described above.

The results from the extraction of the $\delta\langle r^2\rangle$ and $\delta\langle r^4\rangle$ moments are presented in Table V. As seen, the $\delta\langle r^2\rangle$ moment is extracted almost as accurate as before (see Table IV). Further on, the results from extracting the $\delta\langle r^4\rangle$ moments display a discrepancy of $\sim$10.3% and $\sim$6.5% from the exact values, for the ^{234,238}U and ^{236,238}U pairs, respectively.

The nuclear parameters relevant to the reference isotope have been modified here. Thus, the F_k factors have also been reevaluated since they are always deduced for the reference isotope. As a result, aside from the new radial moments differences, the $\delta\nu_{k,\rm RFS}$ field shifts are computed based on updated sets of $F_{k,N}$ factors. This explains the larger discrepancy that is observed when extracting the $\delta\langle r^2\rangle$ and $\delta\langle r^4\rangle$ moments in the latter case (see Table V). However, the results are remarkably good given that the "qualified guess" for the reference isotope is approximately 0.11 fm smaller than the tabulated value used to construct the pseudoexperimental field shifts.

D. Statistical errors when extracting the $\delta\langle r^2\rangle$ and $\delta\langle r^4\rangle$ moments

Above, the $\delta\langle r^2\rangle$ and $\delta\langle r^4\rangle$ moments were extracted by solving the matrix equation

$$\begin{bmatrix}\delta\nu_{1,\rm RFS}\\ \delta\nu_{2,\rm RFS}\end{bmatrix} = C\begin{bmatrix}\delta\langle y_1\rangle\\ \delta\langle y_2\rangle\end{bmatrix}. \tag{25}$$

TABLE IV. Errors, in fm^2 and fm^4, when extracting the $\delta\langle r^2\rangle$ and $\delta\langle r^4\rangle$ moments, for the ^{234,238}U and ^{236,238}U pairs. It is assumed that the rms radii are unknown for the target isotopes. See text for details.

	238,234	238,236
$\delta\langle r^2\rangle$	−0.3282	−0.1642
$\delta\langle r^2\rangle_{\rm expt}$	−0.3272	−0.1638
Error	0.0010	0.0004
$\delta\langle r^4\rangle$	−28.9026	−14.3453
$\delta\langle r^4\rangle_{\rm expt}$	−27.4419	−13.7693
Error	1.4607	0.5760

TABLE V. Same as Table IV. Here, it is assumed that rms radii are unknown for both the reference and the target isotopes. See text for details.

	238,234	238,236
$\delta\langle r^2\rangle$	−0.3287	−0.1640
$\delta\langle r^2\rangle_{\rm expt}$	−0.3272	−0.1638
Error	0.0015	0.0002
$\delta\langle r^4\rangle$	−30.2665	−14.6612
$\delta\langle r^4\rangle_{\rm expt}$	−27.4419	−13.7693
Error	2.8246	0.8919

In order to solve for y_1 and y_2, the matrix C must be invertible. If the matrix determinant is zero, then the matrix is singular and cannot be inverted. It is not rare that the determinant of such matrix can be close to zero, but still nonzero. In this case, the matrix is close to singular and as a result the values of $\delta\langle y_1\rangle$ and $\delta\langle y_2\rangle$ will be hugely affected, even by a small change in the field shifts $\delta\nu_{1,\mathrm{RFS}}$ and $\delta\nu_{2,\mathrm{RFS}}$. Namely, the extracted $\delta\langle y_1\rangle$ and $\delta\langle y_2\rangle$ values, and as a consequence the $\delta\langle r^2\rangle$ and $\delta\langle r^4\rangle$ moments, will to a great degree be affected by the uncertainties in the observed isotope shifts, making the extraction of the radial nuclear moments with high accuracy a difficult task. A C-matrix determinant equal to zero is obtained if the two equations are linearly dependent. In such case, it is not possible to extract two unknowns. Therefore, the transitions considered should be as independent as possible in terms of electronic factors.

The observed isotope shifts $\delta\nu_{k,\mathrm{IS}}^{\mathrm{expt}}$, and subsequently the observed field shifts $\delta\nu_{k,\mathrm{FS}}^{\mathrm{expt}}$, are associated with uncertainties of a certain magnitude. These uncertainties lead to statistical errors in the extracted nuclear moments. In the next subsections, the propagation of these errors is discussed and how they can be minimized by selecting atomic transitions.

1. Statistical errors in relation to the atomic number

In Sec. V B, our method was tested by using $\delta\nu_{\mathrm{RFS}}$ line field shifts as pseudoexperimental data. In order to extend this approach to consider uncertainties we assume uncorrelated errors with an uncertainty $\pm\epsilon$, where $\epsilon = \delta\nu_{k,\mathrm{RFS}} \times 10^{-m}$, in the $\delta\nu_{k,\mathrm{RFS}}$ values that are used for solving the matrix equation [see Eq. (25)]. By varying m, the magnitude of the field shift uncertainty changes. We can then investigate the effect these uncertainties have on the extracted $\delta\langle r^2\rangle$ and $\delta\langle r^4\rangle$ values.

The extraction of the $\delta\langle r^2\rangle$ and $\delta\langle r^4\rangle$ moments was in Sec. V B performed for several uranium, lead, and neodymium isotope pairs (see Fig. 10). By making a reasonable choice of $m = 3$ for the error ϵ in the $\delta\nu_{k,\mathrm{RFS}}$ values relevant to these isotope pairs, it is possible to estimate the magnitude of the statistical errors in the extracted $\delta\langle r^2\rangle$ and $\delta\langle r^4\rangle$ moments. The relative errors of the extracted values for one isotope pair of each of the above elements are indicatively presented in Table VI. The error in $\delta\langle r^2\rangle^{142,150}$ is approximately 72% of the magnitude of the resulting value. Besides, the $\delta\langle r^4\rangle^{142,150}$ is extracted with significantly greater error. However, the relative error in both $\delta\langle r^2\rangle$ and $\delta\langle r^4\rangle$ demonstrates a considerable decrease as the atomic number of the isotopes becomes larger.

TABLE VI. The relative error in the extraction of the $\delta\langle r^2\rangle$ and $\delta\langle r^4\rangle$ moments for the ^{142,150}Nd^{57+}, ^{208,192}Pb^{79+}, and ^{238,236}U^{89+} pairs. The relative errors are presented as a function of the atomic number of these three elements. The inaccuracy assumed in the $\delta\nu_{k,\mathrm{RFS}}$ field shift data is $\pm\epsilon = \delta\nu_{k,\mathrm{RFS}} \times 10^{-3}$.

	^{142,150}Nd	^{208,192}Pb	^{238,236}U
Z	60	82	92
$\frac{\Delta(\delta\langle r^2\rangle)}{\lvert\delta\langle r^2\rangle\rvert}$	0.72	0.39	0.28
$\frac{\Delta(\delta\langle r^4\rangle)}{\lvert\delta\langle r^4\rangle\rvert}$	13.84	5.54	3.65

So far, the extraction of the $\delta\langle r^2\rangle$ and $\delta\langle r^4\rangle$ moments was performed by making use of $\delta\nu_{k,\mathrm{RFS}}$ field shifts and $F_{k,N}$ line field shift factors that are attributed to the first two resonance transitions, i.e., $1s^2\,2s\,{}^2S_{1/2} \longrightarrow 1s^2\,2p\,{}^2P^o_{1/2}$ and $1s^2\,2s\,{}^2S_{1/2} \longrightarrow 1s^2\,2p\,{}^2P^o_{3/2}$. For these two transitions in lithium-like systems, the $F_{k,N}$ factors, as well as the line mass shift parameters $\Delta K_{k,\mathrm{MS}}$, can be determined with high accuracy. Therefore, when we in practice attempt to extract the $\delta\langle r^2\rangle$ and $\delta\langle r^4\rangle$ moments using actual experimental data, the uncertainties in the $\delta\nu_{k,\mathrm{FS}}^{\mathrm{expt}}$ values will normally be dominated by the uncertainties in the $\delta\nu_{k,\mathrm{IS}}^{\mathrm{expt}}$ measurements.

For the ^{142,150}Nd^{57+} pair and the previously mentioned transitions such measurements are available [37]. Taking into account the uncertainties in the measured isotope shifts $\delta\nu_{k,\mathrm{IS}}^{\mathrm{expt}}$, the corresponding uncertainties in $\delta\nu_{k,\mathrm{FS}}^{\mathrm{expt}}$ appear in the fourth and third digits for each of the above transitions, respectively. In this case, the choice of an error $\pm\epsilon = \delta\nu_{k,\mathrm{RFS}} \times 10^{-3}$ in the calculated field shift values seems to be quite realistic. However, according to Table VI the errors in the $\delta\langle r^2\rangle$ and $\delta\langle r^4\rangle$ values resulting from experimental uncertainties of this magnitude for the neodymium pair are evidently extremely large.

We can therefore draw the conclusion that the extraction of the $\delta\langle r^2\rangle^{142,150}$ and $\delta\langle r^4\rangle^{142,150}$ moments with satisfactory accuracy is not likely to be a possibility at the moment. Varying m we deduce that in order for the $\delta\langle r^2\rangle^{142,150}$ and $\delta\langle r^4\rangle^{142,150}$ to be determined with uncertainties of the order of $\lesssim 1\%$ and $\lesssim 14\%$, respectively, we should assume $m \geqslant 5$. In addition, considering Table VI, a more precise extraction of the $\delta\langle r^2\rangle$ and $\delta\langle r^4\rangle$ moments should be possible for the lead and in particular for the uranium isotope pairs.

2. Independent transitions

Considering the two resonance transitions that were used above for extracting $\delta\langle r^2\rangle$ and $\delta\langle r^4\rangle$ moments, we note that the same final state takes part in both. Therefore, these two transitions are not entirely independent and the corresponding $F_{k,N}$ factors do not constitute the best possible set so that we avoid matrix C being close to singular. As a consequence, the uncertainties in the $\delta\langle r^2\rangle$ and $\delta\langle r^4\rangle$ values are relatively large. In order to be able to accurately extract both $\delta\langle r^2\rangle$ and $\delta\langle r^4\rangle$ moments, the precision of the experimental methods must therefore be improved substantially. Alternatively, a larger number of transitions must be available. Using the GRASP2K package, we can easily compute line field shift parameters for more transitions and hence an extended set of $\delta\nu_{k,\mathrm{RFS}}$ values can be generated. The matrix equation will then be formed using $k > 2$ equations, which need to be solved for the same unknowns y_1 and y_2. Having more equations than number of unknowns leads to a reduction of the statistical errors.

Choosing, for instance, to extract the $\delta\langle r^2\rangle$ and $\delta\langle r^4\rangle$ moments for the ^{238,236}U pair, we solve a matrix equation that consists of 16 equations corresponding to 16 different transitions. These transitions involve the following even $1s^2\,2s\,{}^2S_{1/2}$, $1s^2\,3s\,{}^2S_{1/2}$, $1s^2\,3d\ {}^2D_{3/2,5/2}$ and odd $1s^2\,2p\,{}^2P^o_{1/2,3/2}$, $1s^2\,3p\,{}^2P^o_{1/2,3/2}$ states in Li-like uranium. By making the same choice of $m = 3$ for the error $\epsilon = \delta\nu_{k,\mathrm{RFS}} \times 10^{-m}$ in the $\delta\nu_{k,\mathrm{RFS}}$ values, we extract the $\delta\langle r^2\rangle$ and $\delta\langle r^4\rangle$ moments. The extracted $\delta\langle r^2\rangle$ moment has exactly the same value

TABLE VII. The relative error in the extraction of the $\delta\langle r^2\rangle$ and $\delta\langle r^4\rangle$ moments for the $^{238,236}U^{89+}$ pair, initially calculated when the first two resonance transitions were studied, when all 16 theoretically available transitions are used and when we finally choose one set of as independent as possible transitions. The uncertainties assumed in the $\delta\nu_{k,\mathrm{RFS}}$ field shift data are, as in Table VI, $\pm\epsilon = \delta\nu_{k,\mathrm{RFS}} \times 10^{-3}$.

^{238,236}U	2 res.	All 16	2 ind.
$\frac{\Delta(\delta\langle r^2\rangle)}{\lvert\delta\langle r^2\rangle\rvert}$	0.28	0.03	0.02
$\frac{\Delta(\delta\langle r^4\rangle)}{\lvert\delta\langle r^4\rangle\rvert}$	3.65	0.38	0.30

as before, whereas the $\delta\langle r^4\rangle$ value is also about the same, suffering from approximately the same systematical errors. However, the statistical errors in the extraction of both $\delta\langle r^2\rangle$ and $\delta\langle r^4\rangle$ have now been decreased significantly (see Table VII).

In practice, such large number of measured transitions is not likely to be available. Trying all different combinations, we realize that the error in the extraction of the $\delta\langle r^2\rangle$ and $\delta\langle r^4\rangle$ moments, by using a set of only two transitions, varies with the choice of the transitions. For the ^{238,236}U pair and $\epsilon = \delta\nu_{k,\mathrm{RFS}} \times 10^{-3}$ we get $0.0014 \leqslant \frac{\Delta(\delta\langle r^2\rangle)}{\lvert\delta\langle r^2\rangle\rvert} \leqslant 80$ and $0.0012 \leqslant \frac{\Delta(\delta\langle r^4\rangle)}{\lvert\delta\langle r^4\rangle\rvert} \leqslant 1100$, for the relative errors in the extraction of the $\delta\langle r^2\rangle$ and $\delta\langle r^4\rangle$ moments, respectively.

We therefore deduce that in order to limit the magnitude of the statistical errors, it is more important to make a choice of as independent as possible transitions that form the set of equations solved, rather than increasing the number of transitions. Based on this conclusion, instead of extracting the $\delta\langle r^2\rangle$ and $\delta\langle r^4\rangle$ moments using the first two resonance transitions, a set of two more independent transitions is chosen. Thus, we attempt to extract the $\delta\langle r^2\rangle$ and $\delta\langle r^4\rangle$ moments for the ^{238,236}U isotope pair, using the resonance transition $1s^2\,2s\,{}^2S_{1/2} \longrightarrow 1s^2\,2p\,{}^2P^o_{1/2}$ combined with the $1s^2\,3p\,{}^2P^o_{1/2} \longrightarrow 1s^2\,3d\,{}^2D_{3/2}$ transition. The resulting relative errors for this combination of transitions are also displayed in Table VII. As seen, the relative errors in the extraction of both $\delta\langle r^2\rangle$ and $\delta\langle r^4\rangle$ moments are decreased when a more optimal combination of 2 out of the total 16 available transitions is chosen.

TABLE VIII. Same as Table IV. Here, the line field shift factors $F_{k,N}$ correspond to the $1s^2\,2s\,{}^2S_{1/2} \longrightarrow 1s^2\,2p\,{}^2P^o_{1/2}$ and $1s^2\,3p\,{}^2P_{1/2} \longrightarrow 1s^2\,3d\,{}^2D_{3/2}$ transitions. Statistical errors are given in the rightmost column assuming uncertainties in the "pseudoexperimental" field shifts according to $\epsilon = \delta\nu_{k,\mathrm{RFS}} \times 10^{-3}$.

	238,236	
$\delta\langle r^2\rangle$	−0.1646	±0.0036
$\delta\langle r^2\rangle_{\mathrm{exact}}$	−0.1638	
Error	0.0008	
$\delta\langle r^4\rangle$	−14.7283	±3.5279
$\delta\langle r^4\rangle_{\mathrm{exact}}$	−13.7693	
Error	0.9590	

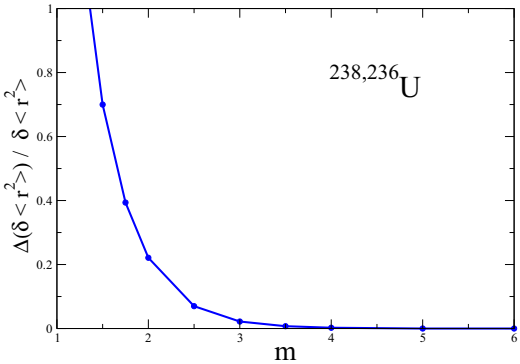

FIG. 11. The relative error in the extraction of the $\delta\langle r^2\rangle$ moment as a function of m number in the assumed uncertainty $\epsilon = \delta\nu_{k,\mathrm{RFS}} \times 10^{-m}$ of the field shift. For the extraction, the pair of $1s^2\,2s\,{}^2S_{1/2} \longrightarrow 1s^2\,2p\,{}^2P^o_{1/2}$ and $1s^2\,3p\,{}^2P_{1/2} \longrightarrow 1s^2\,3d\,{}^2D_{3/2}$ transitions in Li-like ^{238,236}U has been used.

3. *Errors in the extraction of* $\delta\langle r^4\rangle^{238,236}$

Having ascertained that the "right" combination of transitions provides us with reasonably small statistical errors, we can extract the $\delta\langle r^2\rangle$ and $\delta\langle r^4\rangle$ moments for the ^{238,236}U isotope pair using pseudoexperimental field shifts, as described in Sec. V C 1, for this "optimal" pair of transitions. The statistical uncertainties are estimated as $\epsilon = \delta\nu_{k,\mathrm{RFS}} \times 10^{-m}$ with $m = 3$, which has been used so far for determining the assumed uncertainty in the $\delta\nu_{k,\mathrm{RFS}}$ values.

The extracted radial moments together with the resulting errors are displayed in Table VIII. Comparing the respective results of Table IV with the results in Table VIII, we deduce that although in the latter case the systematical errors are larger the statistical errors of the extracted $\delta\langle r^2\rangle$ and $\delta\langle r^4\rangle$ values are significantly smaller. We see that now the relative statistical errors are $\frac{\Delta(\delta\langle r^2\rangle)}{\lvert\delta\langle r^2\rangle\rvert} = 0.022$ and $\frac{\Delta(\delta\langle r^4\rangle)}{\lvert\delta\langle r^4\rangle\rvert} = 0.24$, respectively.

In Figs. 11 and 12, the relative errors in the extraction of the $\delta\langle r^2\rangle$ and $\delta\langle r^4\rangle$ moments are illustrated as a function of the m value. As seen, the results are rather sensitive to the m value and the relative error increases dramatically as the precision of the field shift values decreases. This is even more pronounced for the errors in the extracted $\delta\langle r^4\rangle$ moments. Nevertheless, for $m = 3$ both $\delta\langle r^2\rangle$ and $\delta\langle r^4\rangle$ moments are extracted with satisfactory accuracy. Thus, we deduce that provided the current experimental precision in the isotope shift measurements, an accurate enough extraction of the $\delta\langle r^2\rangle$ and $\delta\langle r^4\rangle$ moments could be possible as long as the measured transitions are sufficiently independent in terms of electronic factors.

VI. SUMMARY AND CONCLUSIONS

Combining nuclear DFT-type models with MCHF calculations for atomic states it is possible to achieve a higher precision in the predictions of atomic line field shifts. Changes in the nuclear charge distribution caused by shell structure, deformations, and variations in the diffuseness of the nuclei

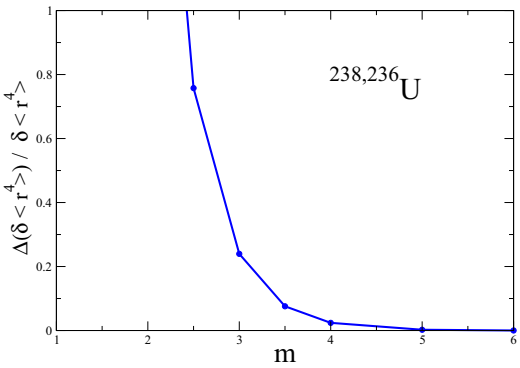

FIG. 12. Same as Fig. 11, but for the relative uncertainty in the extraction of the $\delta\langle r^4\rangle$ moment using the same pair of transitions.

are then automatically taken into account. In this work, it is shown that capturing all these effects leads to an improved description of experiments.

With the continuous advancement in experimental methods, one may ask whether the improved precision and access to several atomic transitions makes it possible to obtain more data on the nuclear isotopes than just the $\delta\langle r^2\rangle$ values commonly extracted so far. By constructing a set of theoretical field shifts we explore the possibility of extracting information about the nucleus by inverting the first-order perturbation theory equations for the field shifts. In this way, we demonstrate that the electron states are sensitive not only to the $\delta\langle r^2\rangle$ values but also to changes in $\langle r^4\rangle$ values. This opens the possibility for systematic tabulation of these higher-order nuclear moments. Considering both statistical and systematical errors in the extraction procedure we conclude that an increase in experimental precision by one to two orders of magnitude or access to data for more independent atomic transitions would be essential. As a promising candidate for future experiments, we suggest Li-like uranium where an increase in precision with one order of magnitude along with access to at least two independent transitions would allow accurate $\delta\langle r^4\rangle$ values to be extracted.

ACKNOWLEDGMENTS

This work was supported by the Swedish Research Council (VR). The authors acknowledge P. Jönsson, Malmö University, and C. Brandau, GSI, for discussions and C. Nazé, J. G. Li, and M. Godefroid for providing the barium MCDHF wave functions.

APPENDIX: RFS EXPANSION IN ORTHONORMAL BASIS

The RFS is, for a certain transition, given by the expansion

$$\sum_{N=1}^{4} F_N \delta\langle r^{2N}\rangle = F_1\delta\langle r^2\rangle + F_2\delta\langle r^4\rangle + F_3\delta\langle r^6\rangle + F_4\delta\langle r^8\rangle,$$

where the line field shift factors F_N play the role of expansion coefficients. The set of r^{2N} that forms the basis $\{r^2, r^4, r^6, r^8\}$ is not orthonormal. It is reasonable to assume that a rearrangement using an orthonormal basis should lead to faster convergence. Here, we orthonormalize the initial basis with respect to the scalar product:

$$\langle u \mid v\rangle = \int u * v * w r^2 dr,$$

where w is the weight function that approximates the nucleus. Since the functions y_N, forming the basis $\{y_1, y_2, y_3, y_4\}$, are constructed to be orthogonal they will probe different aspects of the nuclear charge distribution within the nuclear volume. Thus, we expect that the expansion

$$\sum_{N=1}^{4} c_N \delta\langle y_N\rangle = c_1\delta\langle y_1\rangle + c_2\delta\langle y_2\rangle + c_3\delta\langle y_3\rangle + c_4\delta\langle y_4\rangle$$

will converge faster than $\sum_{N=1}^{4} F_N\delta\langle r^{2N}\rangle$ does. In the expression above, c_N are the expansion coefficients. Assuming that the nucleus can be approximated as a hard sphere, one can use $w = \rho_0\Theta(R-r)$ with $R = 1.25A^{1/3}$. The value of ρ_0 is determined by the normalization condition $4\pi\int\rho_0 r^2 dr = 1$. Following the Gram-Schmidt process [44], we obtain

$$y_1 = \frac{3.46556}{\bar{A}^{2/3}} r^2,$$

$$y_2 = -\frac{15.2051}{\bar{A}^{2/3}} r^2 + \frac{12.5116}{\bar{A}^{4/3}} r^4,$$

$$y_3 = \frac{39.9503}{\bar{A}^{2/3}} r^2 - \frac{80.3573}{\bar{A}^{4/3}} r^4 + \frac{37.1429}{\bar{A}^{2}} r^6,$$

$$y_4 = -\frac{82.4315}{\bar{A}^{2/3}} r^2 + \frac{293.927}{\bar{A}^{4/3}} r^4 - \frac{313.522}{\bar{A}^{2}} r^6 + \frac{103.367}{\bar{A}^{8/3}} r^8,$$

where $\bar{A}$ is taken as the average of the mass numbers of the two isotopes. The sum of the expansion terms has been rearranged but $\sum_{N=1}^{4} F_N\delta\langle r^{2N}\rangle = \sum_{N=1}^{4} c_N\delta\langle y_N\rangle$ must still hold. The c_N coefficients can be found by equating same order terms in the above equation. Hence, the new coefficients are

$$c_1 = 0.288554\bar{A}^{2/3}F_1 + 0.350673\bar{A}^{4/3}F_1 + 0.448303\bar{A}^2F_3 + 0.592709\bar{A}^{8/3}F_4,$$

$$c_2 = 0.0799258\bar{A}^{4/3}F_2 + 0.172916\bar{A}^2F_3 + 0.2972\bar{A}^{8/3}F_4,$$

$$c_3 = 0.026923\bar{A}^2F_3 + 0.08166\bar{A}^{8/3}F_4,$$

$$c_4 = 0.00967424\bar{A}^{8/3}F_4.$$

Now, the RFS is given by the summation

$$\sum_{N=1}^{4} c_N\delta\langle y_N\rangle$$

and the matching percentage to the final field shift after each term has been added differs from the one when the original summation is used.

As seen in Fig. 9, the orthogonal expansion converges substantially faster than the original summation. In fact, only the $\delta\langle r^2\rangle$ and $\delta\langle r^4\rangle$ moments need to be considered as long as the sum is rearranged. Thus, for a pair of isotopes A, A'

and a transition k, the RFS is to a very good approximation expressed as

$$\delta\nu^{A,A'}_{k,\mathrm{RFS}} \approx c_{k,1}\delta\langle y_1\rangle + c_{k,2}\delta\langle y_2\rangle.$$

In case the isotope shifts are known for two transitions, a system of two equations can be formed, and the $c_{k,1}$ and $c_{k,2}$ constants can be evaluated using the expressions above. They depend on the line field shift factors $F_{k,N}$ that are different for each transition and which are calculated for the reference isotope A. Therefore, for two transitions, the problem takes the form of a matrix equation

$$\begin{bmatrix}\delta\nu^{A,A'}_{1,\mathrm{RFS}}\\ \delta\nu^{A,A'}_{2,\mathrm{RFS}}\end{bmatrix} \approx \begin{bmatrix}c_{1,1} & c_{1,2}\\ c_{2,1} & c_{2,2}\end{bmatrix}\begin{bmatrix}\delta\langle y_1\rangle\\ \delta\langle y_2\rangle\end{bmatrix}.$$

The unknown y_1 and y_2 can thus be solved according to

$$\begin{bmatrix}\delta\langle y_1\rangle\\ \delta\langle y_2\rangle\end{bmatrix} \approx C^{-1}\begin{bmatrix}\delta\nu^{A,A'}_{1,\mathrm{RFS}}\\ \delta\nu^{A,A'}_{2,\mathrm{RFS}}\end{bmatrix},$$

where C^{-1} is the inverse matrix of $\left[\begin{smallmatrix}c_{1,1} & c_{1,2}\\ c_{2,1} & c_{2,2}\end{smallmatrix}\right]$. The $\delta\langle r^2\rangle$ and $\delta\langle r^4\rangle$ moments are finally extracted by solving the equations

$$\begin{bmatrix}\delta\langle y_1\rangle\\ \delta\langle y_2\rangle\end{bmatrix} = \begin{bmatrix}3.46556/\bar{A}^{2/3} & 0\\ -15.2051/\bar{A}^{2/3} & 12.5116/\bar{A}^{4/3}\end{bmatrix}\begin{bmatrix}\delta\langle r^2\rangle\\ \delta\langle r^4\rangle\end{bmatrix}.$$

This can be compared with the original summation, where if the approximate relation

$$\delta\nu^{A,A'}_{k,\mathrm{RFS}} \approx F_{k,1}\delta\langle r^2\rangle + F_{k,2}\delta\langle r^4\rangle$$

is assumed, the matrix equation to be solved is given by

$$\begin{bmatrix}\delta\nu^{A,A'}_{1,\mathrm{RFS}}\\ \delta\nu^{A,A'}_{2,\mathrm{RFS}}\end{bmatrix} \approx \begin{bmatrix}F_{1,1} & F_{1,2}\\ F_{2,1} & F_{2,2}\end{bmatrix}\begin{bmatrix}\delta\langle r^2\rangle\\ \delta\langle r^4\rangle\end{bmatrix}.$$

[1] I. Angeli and K. Marinova, Table of experimental nuclear ground state charge radii: An update, At. Data Nucl. Data Tables **99**, 69 (2013).

[2] C. G. Parthey *et al.*, Precision measurement of the hydrogen-deuterium $1s-2s$ isotope shift, Phys. Rev. Lett. **104**, 233001 (2010).

[3] S. E. Agbemava, A. V. Afanasjev, D. Ray, and P. Ring, Global performance of covariant energy density functionals: Ground state observables of even-even nuclei and the estimate of theoretical uncertainties, Phys. Rev. C **89**, 054320 (2014).

[4] D. Andrae, Finite nuclear charge density distributions in electronic structure calculations for atoms and molecules, Phys. Rep. **336**, 413 (2000).

[5] Y. S. Kozhedub, O. V. Andreev, V. M. Shabaev, I. I. Tupitsyn, C. Brandau, C. Kozhuharov, G. Plunien, and T. Stöhlker, Nuclear deformation effect on the binding energies in heavy ions, Phys. Rev. A **77**, 032501 (2008).

[6] N. A. Zubova, Y. S. Kozhedub, V. M. Shabaev, I. I. Tupitsyn, A. V. Volotka, G. Plunien, C. Brandau, and Th. Stöhlker, Relativistic calculations of the isotope shifts in highly charged Li-like ions, Phys. Rev. A **90**, 062512 (2014).

[7] M. J. G. Borge, Recent highlights of the isolde facility, J. Phys.: Conf. Ser. **580**, 012049 (2015).

[8] C. Brandau, M. Lestinsky, C. Kozhuharov, A. Müller, S. Schippers, and Th. Stöhlker, High-resolution dielectronic recombination experiments at the upcoming cryring@esr facility, J. Phys.: Conf. Ser. **635**, 022084 (2015).

[9] C. W. P. Palmer, Reformulation of the theory of the mass shift, J. Phys. B: At. Mol. Phys. **20**, 5987 (1987).

[10] V. M. Shabaev, Mass corrections in a strong nuclear field, Theor. Math. Phys. **63**, 588 (1985).

[11] V. Shabaev and A. Artemyev, Relativistic nuclear recoil corrections to the energy levels of multicharged ions, J. Phys. B: At. Mol. Phys. **27**, 1307 (1994).

[12] E. C. Seltzer, k x-ray isotope shifts, Phys. Rev. **188**, 1916 (1969).

[13] G. Torbohm, B. Fricke, and A. Rosén, State-dependent volume isotope shifts of low-lying states of group-ii a and -ii b elements, Phys. Rev. A **31**, 2038 (1985).

[14] S. Blundell, P. Baird, C. Palmer, D. Stacey, and G. Woodgate, A reformulation of the theory of field isotope shift in atoms, J. Phys. B: At. Mol. Phys. **20**, 3663 (1987).

[15] J. Ekman *et al.* [Comp. Phys. Comm. (unpublished)]

[16] P. Jönsson, G. Gaigalas, J. Bieroń, C. Froese Fischer, and I. Grant, New version: Grasp2k relativistic atomic structure package, Comput. Phys. Commun. **184**, 2197 (2013).

[17] I. P. Grant, *Springer Series on Atomic, Optical and Plasma Physics*, Vol. 40 (Springer, Berlin, 2007).

[18] B. J. McKenzie, I. P. Grant, and P. H. Norrington, A program to calculate transverse breit and qed corrections to energy levels in a multiconfiguration dirac-fock environment, Comput. Phys. Commun. **21**, 233 (1980).

[19] C. Nazé, E. Gaidamauskas, G. Gaigalas, M. Godefroid, and P. Jönsson, ris3: A program for relativistic isotope shift calculations, Comput. Phys. Commun. **184**, 2187 (2013).

[20] S. A. Blundell, W. R. Johnson, and J. Sapirstein, Improved many-body perturbation theory calculations of the $n=2$ states of lithiumlike uranium, Phys. Rev. A **41**, 1698 (1990).

[21] W. R. Johnson, J. Sapirstein, and K. T. Cheng, Theory of $2s_{1/2}$-$2p_{3/2}$ transitions in highly ionized uranium, Phys. Rev. A **51**, 297 (1995).

[22] J. D. Zumbro, E. B. Shera, Y. Tanaka, C. E. Bemis, R. A. Naumann, M. V. Hoehn, W. Reuter, and R. M. Steffen, $e2$ and $e4$ deformations in ^{233,234,235,238}U, Phys. Rev. Lett. **53**, 1888 (1984).

[23] J. D. Zumbro, R. A. Naumann, M. V. Hoehn, W. Reuter, E. B. Shera, C. E. Bemis, and Y. Tanaka, E2 and e4 deformations in ^{232}Th and ^{239,240,242}Pu, Phys. Lett. B **167**, 383 (1986).

[24] P. Ring and P. Schuck, *The Nuclear Many-Body Problem*, 1st ed. (Springer, New York, 1980).

[25] E. Chabanat, P. Bonche, P. Haensel, J. Meyer, and R. Schaeffer, A Skyrme parametrization from subnuclear to neutron star densities Part ii. Nuclei far from stabilities, Nucl. Phys. A **635**, 231 (1998).

[26] B. A. Brown, New Skyrme interaction for normal and exotic nuclei, Phys. Rev. C **58**, 220 (1998).

[27] B. G. Carlsson, J. Dobaczewski, J. Toivanen, and P. Veselý, Solution of self-consistent equations for the N^{3}LO nuclear

energy density functional in spherical symmetry. The program hosphe (v1.02), Comput. Phys. Commun. **181**, 1641 (2010).

[28] M. Stoitsov, N. Schunck, M. Kortelainen, N. Michel, H. Nam *et al.*, Axially deformed solution of the Skyrme-Hartree-Fock-Bogoliubov equations using the transformed harmonic oscillator basis (ii) HFBTHO v2.00d: A new version of the program, Comput. Phys. Commun. **184**, 1592 (2013).

[29] A. Bouyssy, J. F. Mathiot, N. Van Giai, and S. Marcos, Relativistic description of nuclear systems in the Hartree-Fock approximation, Phys. Rev. C **36**, 380 (1987).

[30] R. Rosenfelder, Coulomb corrections to elastic electronproton scattering and the proton charge radius, Phys. Lett. B **479**, 381 (2000).

[31] R. Pohl, R. Gilman, G. Miller, and K. Pachucki, Muonic Hydrogen and the Proton Radius Puzzle, Annu. Rev. Nucl. Part. Sci. **63**, 175 (2013).

[32] H. De Vries, C. W. De Jager, and C. De Vries, Nuclear Charge-Density-Distribution Parameters from Electron Scattering, At. Data Nucl. Data Tables **36**, 495 (1987).

[33] G. Fricke, C. Bernhardt, K. Heilig, L. A. Schaller, L. Schellenberg, E. B. Shera, and C. W. Dejager, Nuclear ground state charge radii from electromagnetic interactions, At. Data Nucl. Data Tables **60**, 177 (1995).

[34] W. van Wijngaarden and J. Li, Hyperfine splittings and isotope shifts of (6s)21s0-(6s6p) 1p1 transition in barium, Can. J. Phys. **73**, 484 (1995).

[35] C. Nazé, J. G. Li, and M. Godefroid, Theoretical isotope shifts in neutral barium, Phys. Rev. A **91**, 032511 (2015).

[36] J. Li, C. Nazé, M. Godefroid, S. Fritzsche, G. Gaigalas, P. Indelicato, and P. Jönsson, Mass- and field-shift isotope parameters for the $2s$–$2p$ resonance doublet of lithiumlike ions, Phys. Rev. A **86**, 022518 (2012).

[37] C. Brandau, C. Kozhuharov, Z. Harman, A. Müller, S. Schippers, Y. S. Kozhedub, D. Bernhardt, S. Böhm, J. Jacobi, E. W. Schmidt, P. H. Mokler, F. Bosch, H.-J. Kluge, Th. Stöhlker, K. Beckert, P. Beller, F. Nolden, M. Steck, A. Gumberidze, R. Reuschl, U. Spillmann, F. J. Currell, I. I. Tupitsyn, U. D. Jentschura, V. M. Shabaev, C. H. Keitel, A. Wolf, and Z Stachura, Isotope Shift in the Dielectronic Recombination of Three- Electron $^{A}Nd^{57+}$, Phys. Rev. Lett. **100**, 073201 (2008).

[38] S. R. Elliott, P. Beiersdorfer, and M. H. Chen, Trapped-Ion Technique for Measuring the Nuclear Charge radii of Highly Charged Radioactive Isotopes, Phys. Rev. Lett. **76**, 1031 (1996).

[39] G. Plunien, B. Müller, W. Greiner, and G. Soff, Nuclear polarization contribution to the lamb shift in heavy atoms, Phys. Rev. A **39**, 5428 (1989).

[40] G. Plunien, B. Müller, W. Greiner, and G. Soff, Nuclear polarization in heavy atoms and superheavy quasiatoms, Phys. Rev. A **43**, 5853 (1991).

[41] G. Plunien and G. Soff, Nuclear-polarization contribution to the lamb shift in actinide nuclei, Phys. Rev. A **51**, 1119 (1995).

[42] G. Plunien and G. Soff, Erratum: Nuclear-polarization contribution to the lamb shift in actinide nuclei, Phys. Rev. A **53**, 4614 (1996).

[43] T. Beier, P. J. Mohr, H. Persson, and G. Soff, Influence of nuclear size on QED corrections in hydrogenlike heavy ions, Phys. Rev. A **58**, 954 (1998).

[44] E. W. Weisstein, Gram-Schmidt orthonormalization, from MATHWORLD, a Wolfram web resource.

Printed by Media-Tryck, Lund 2020 NORDIC SWAN ECOLABEL 3041 0903

Computational Atomic Structure: Applications to Astrophysics and Nuclear Structure

This is a thesis about atoms and ions; their structures and the interactions of their electrons with internal and external electromagnetic fields and with the nucleus. I grew up in Athens, Greece, and had my graduate education in Lund. This work was performed at the Department of Materials Science and Applied Mathematics at Malmö University and the Department of Physics at Lund University and defended on the 13th of March 2020. The picture was taken before swimming with seals in Cape Town.

LUND UNIVERSITY

Lund University
Faculty of Science
Department of Physics
Division of Mathematical Physics

ISBN 978-91-7895-436-0